

UNIVERSITY OF CALIFORNIA

Los Angeles

Integrated Cryogenic Buffer Gas Beam, Linear Quadrupole Trap, and Time of Flight Mass
Spectrometer for Low Temperature Ion-Molecule Chemistry

A dissertation submitted in partial satisfaction

of the requirements for the degree

Doctor of Philosophy in Physics

by

Gary Chen

2019

© Copyright by

Gary Chen

2019

ABSTRACT OF THE DISSERTATION

Integrated Cryogenic Buffer Gas Beam, Linear Quadrupole Trap, and Time of Flight Mass Spectrometer for Low Temperature Ion-Molecule Chemistry

by

Gary Chen

Doctor of Philosophy in Physics

University of California, Los Angeles, 2019

Professor Wes Campbell, Chair

The dissertation of Gary Chen is approved.

Eric Hudson

Paul Hamilton

James Larkin

Wes Campbell, Committee Chair

University of California, Los Angeles

2019

?

CONTENTS

List of Figures	viii
Preface	xiii
Curriculum Vitae	xiv
1 Introduction	1
1.1 Thesis Outline	1
2 Chemical Rate Constants	2
2.1 Average Dipole Orientation Theory (ADO)	3
2.1.1 Radially Symmetric Adiabatic Capture Theory	3
2.1.2 Ion-Dipole Interaction	5
3 The Cryogenic Buffer Gas Beam (CBGB)	11
3.1 Design	13
3.1.1 Heat Load and Thermal Conductivity	16
3.1.2 Gas Fill Lines	19
3.2 Beam Density and Extraction	23
3.2.1 Direct Beam Measurement and Parameterization	27
3.2.2 Beam Density at Ion Trap	32
3.3 Beam Velocity	33
3.4 Beam Shuttering	37
4 Trapping and Cooling Ions	40

4.1	Ion Trapping	40
4.2	Vacuum Requirements	43
4.3	${}^9\text{Be}^+$ Laser Cooling	44
4.4	Imaging System	47
4.5	Determining Excited state	49
4.6	Time of Flight Mass Spectrometer (TOF-MS)	52
4.7	Dual Species Loading	52
5	$\text{Be}^+({}^2\text{S}_{1/2}/{}^2\text{P}_{3/2}) + \text{H}_2\text{O}$	56
5.1	Optical Control of Reactions between Water and Laser-Cooled Be^+ Ions . . .	56
5.1.1	Abstract	56
6	$\text{Be}^+ + \text{H}_2\text{O/HOD/D}_2\text{O}$	63
6.1	Isotope-selective chemistry in the $\text{Be}^+({}^2\text{S}_{1/2}) + \text{HOD} \rightarrow \text{BeOD}^+/\text{BeOH}^+ + \text{H/D}$ reaction	63
6.2	Abstract	63
6.3	Introduction	63
6.4	Experimental	65
6.5	Results and Discussion	69
6.6	Conclusion	71
7	O_2 Titration	73
7.1	$\text{Be}^+ + \text{O}_2$	73
7.2	$\text{C}^+ + \text{O}_2$	76
8	$\text{Low Temperature C}^+ + \text{H}_2\text{O}$	78
8.1	Formyl Isomer Production	78

8.2 $^{15}\text{N}_2$ Titration	80
8.2.1 Branching Ratio Determination	82
9 Conclusion and Future Outlook	85
A Chemical Rate Equations	86
A.1 $\text{Be}^+ + \text{H}_2\text{O} + \text{H}_2$	86
A.2 $\text{Be}^+ + \text{H}_2\text{O}/\text{HOD}/\text{D}_2\text{O}$	87
A.3 $\text{C}^+ + \text{H}_2\text{O}$	87
B CBGB Drawings	89
References	91

LIST OF FIGURES

2.1 Numerical solutions for eq. (2.15) as a function of maximum angle K . In the limit of large K , we find an intuitive solution where θ_1 averages towards 0.	8
2.2 Numerical solution to eq. (2.16) as a function of the ratio of rotational energy and the monopole-dipole term. The low ratio behavior is not immediately obvious, but the greater the ratio between the rotational energy and monopole-dipole term, the more θ_2 tends towards $\pi/2$	9
2.3 Dipole locking constant C parameterized by the dipole moment μ_D and polarizability α .[47]	10
 3.1 Schematic of target species entrainment within a buffer gas beam cell. With high densities of buffer gas particles, an introduced target species undergoes collisions with the buffer gas such that it cools. At high enough densities, flow dynamics cause the target species to become entrained in the buffer gas flow and are carried out of the cell with greater efficiency.	12
3.2 Cross sectional view of CBGB in solidworks. Components include copper sheath for PTR, aluminum radiation shield with chevron baffles, copper shield and experimental cell, and skimmer mounted in stem chamber. The baffles allow for gas to flow into the cold region of the beam apparatus, while preventing 300 K black body radiation from hitting the inner shield and cell.	15
3.3 Cross sectional view of CBGB with side walls removed from the outer vacuum chamber, 40 K aluminum radiation shield, and inner 4 K cryopumping shield exposing the inner experimental cell. A skimmer is mounted in the stem region.	16
3.4 The water fill line, sealed by an ultratorr fitting and heated by nichrome wire. A shut off valve and vernier valve are used to regulate the flow of water into the buffer gas cell.	21

3.5 A kapton film serves as the back wall of the buffer gas cell with a hole punctured for the insertion of the water fill line. The kapton surface seals the back of the cell for a stronger forward beam, while limiting the heat load from a room temperature fill line, and resisting ice formation allowing for continuous and consistent operation with water for over 10 hours.	22
3.6 Theoretically derived buffer gas beam properties of interest given the physical dimensions of our cell in particular: $d_{aperture} = 9$ mm. A) γ extraction ratio, dotted red line indicates $\gamma = 1$ where hydrodynamic entrainment begins. B) Number density of buffer gas species within the experimental cell, given an enclosed back wall. The density of target species introduced should stay under 1% of the buffer gas density for other properties to hold. C) Number of collisions a target species particle would expect before extraction out of the cell, the dotted red line indicates 100 collisions before extraction, when rotational degrees of freedom are characteristically thermalized.	27
3.7 Fitted linear behavior of H ₂ O entrained in a Ne buffer gas beam 30 cm from cell aperture. The onset of hydrodynamic entrainment seems to occur around 20 SCCM up through 60/65 SCCM where the H ₂ O extracted into the beam has a clear linear form of $(9.2 \times 10^8 \text{ cm}^{-3}/\text{SCCM})f - 2 \times 10^{10} \text{ cm}^{-3}$	28
3.8 Projected beam densities with a Ne flow rate of 30 SCCM with various distances of interest within the chamber. Beam densities shown are without throttling of the H ₂ O flow valve.	30
3.9 Projected beam densities at the trap center over various nominal Ne flow rates and smallest skimmer aperture size. Beam densities shown are without throttling of the H ₂ O flow valve.	31
3.10 text	32
3.11 Be ⁺ decay and BeOH ⁺ appearance due to the introduction of H ₂ O from the CBGB. A shared fit of rates 5.1 and 5.2 yields a water beam density $\rho_{beam} = (2.18 \pm 0.37) \times 10^6 \text{ cm}^{-3}$	33

3.12 Angled longitudinal scan of Yb fluorescence collected by PMT at \approx 24 cm from cell aperture. A fit of all isotopic peaks yields mggm	36
3.13 Ratios of water and neon from the beam when the Uniblitz shutter is opened and closed. Detection is done via RGA placed 30 cm from the cell aperture.	38
3.14 Fluorescence decays of loaded Be^+ ions exposed to a cold water beam with an inline shutter either opened, in green ($\tau = 7.23 \times 10^{-3}$ s) or closed, in blue ($\tau = 6.37 \times 10^{-2}$ s)	38
3.15 Fluorescence decays of loaded Be^+ ions exposed to a cold water beam with an inline shutter opened, in green ($\tau = 5.37 \times 10^{-2}$ s) or closed, in red ($\tau = 7.59 \times 10^{-3}$ s)	39
4.1 The ion trap inside of the experimental vacuum chamber. An Einzel lens and imaging objective are seen on the vertical axis.	42
4.2 Stability diagram of the experimental ion trap with parameters defined in table 4.1. The trap is set up to be stable for ions of interest, including high mass reaction products, from Be^+ , and C^+ at $m/z = 9$, 12 to CO_2H^+ at $m/z = 45$. . .	43
4.3 Differential pumping region in between the stem and ion trap chambers with gate valves on either end. Blank copper CF gaskets with apertures of 4 mm and 10 mm are placed towards the stem and ion chamber respectively to limit conductance of background gasses while allowing the cryogenic beam through. An Agilent Twistorr 84 FS turbo pump keeps the region at pressures around 10^{-10} Torr and a leak valve allows for controlled introduction of secondary gasses.	44
4.4 Electronic structure of ${}^9\text{Be}^+$, laser cooling is done with 313 nm light.	45
4.5 AOM's running at 400 MHz are used to tune the initially blue detuned primary beam on resonance with the ${}^2\text{S}_{1/2}$ to ${}^2\text{P}_{3/2}$ transition. A double passed AOM tunes the primary beam to the ${}^2\text{S}_{3/2}$ to ${}^2\text{P}_{3/2}$ transition to re-pump any ${}^2\text{P}_{3/2} \longrightarrow {}^2\text{S}_{3/2}$ decays. A third AOM creates a first order beam 200 MHz red to aid the capture of hot ablated Be^+ ions.	45

4.6	The iXon3 camera is mounted onto a 3 axis translation stage as well as the enclosed imaging pathway. The imaging tubes include the Sill objective lens at the end, inserted into the reentrant flange, an angled mirror, and a 313 nm bandpass filter placed at the camera input.	48
4.7	A set of ion images taken at various 313 nm powers run thorough a maximum filter algorithm that identifies local maxima, representing individual ions (circled in red).	50
4.8	Individual ions identified from images in figure 4.7. Integrated pixel values with subtracted background counts shown for each image, a set's averaged value is shown in brackets.	51
4.9	P-state fraction curve fitted to incident laser power at a fixed detuning of $\delta = \Gamma/2$. Total fluorescence value is normalized by fitted efficiency parameter a to yield ρ_{pp}	52
4.10	Image of the single laser, dual ablation set up. The 1064 nm YAG pulse is split into two paths, and recombined such that they proceed through the same focusing element into the chamber to hit two different targets.	54
4.11	TOF trace of simultaneous Be^+ and C^+ ablation loading averaged over 10 shots. A soft A-ramp is applied after loading, ejecting any unintentionally loaded Cn^+ clusters. The C^+ peak is narrowed from sympathetic cooling with the laser cooled Be^+ ions.	55
5.1	61
5.2	62
6.1	66
6.2	67
6.3	67
6.4	68
6.5	68

7.1	A linear dependence on the rate constant for reaction 7.3 as a function of P state excitation. $k = (6 \pm 1) \times 10^{-11}P + (-0.03 \pm 0.16) \times 10^{-11}$	74
7.2	Shared fitting of trapped products with 14% p-state excitation.	74
7.3	Shared fitting of trapped products where Be^+ was exposed to O_2 without the 313 nm light.	75
7.4	TOF traces for data taken with 14% p-state excitation at 0s and 200s showing no products at 0s, distinct peaks for reaction products BeH^+ , BeOH^+ , and O_2^+ , but an absence of BeO^+ .	75
7.5	TOF traces for data taken with without laser excitation at 0 s and 50 s showing residual BeOH^+ at 0 s, but only an inclusion of BeO^+ at 50 s. More endothermic product channels of BeH^+ and O_2^+ are absent.	76
8.1	TOF trace of reaction products of Be^+ and C^+ after exposure to both water from the CBGB beam, and CO (10 s) before titration with $^{15}\text{N}_2$ (10 s). There is a distinct lack of N_2H^+ , indicating full conversion of $\text{HOC}^+ \longrightarrow \text{HCO}^+$.	81
8.2	text	82
8.3	$^{15}\text{N}_2$ introduced into the ion chamber after trapped Be^+ and C^+ are exposed to water from the CBGB for set times.	83

PREFACE

CURRICULUM VITAE

- 2009 – 2013 B.S. in Physics, University of Maryland (UMD), College Park, Maryland
- 2013 – Present Ph.D. student in Physics, University of California, Los Angeles (UCLA).

CHAPTER 1

Introduction

This thesis chronicles the experimental work done to realize an apparatus for cold ion-molecule chemistry of species of astrochemical interest, and attempts to understand chemistry in general along the way.

1.1 Thesis Outline

CHAPTER 2

Chemical Rate Constants

When describing the rates of chemical reactions, it is usually described by the order of reaction. Usually the order of reaction is dependent on the sum of the order the constituents contribute to the reaction. For example, if we have a reaction of:



The appearance of products $[C]$ and $[D]$ is directly equivalent to the disappearance of $[A]$ and $[B]$. The rate constant is then defined as:

$$k = \frac{\Gamma}{[A]^m[B]^n}$$

Where k is the rate constant, and Γ is the reaction rate in time. The order of the reaction is defined as the sum of the constituent power dependencies $m + n$. For gas phase reactions, the dependencies are usually of order unity, as it is unlikely to have multiple collisions during a single reaction lifetime. For bi-molecular reactions that we are exploring, we would expect the rate to be a second order rate, which gives a solution of:

$$\frac{[A]}{[B]} = \frac{[A]_0}{[B]_0} e^{([A]_0 - [B]_0)kt}$$

Where the rate constant $k = (([A]_0 - [B]_0)\tau)^{-1}$. In reality, we are only trapping a few ions in the trap while flooding the chamber with neutral reactants from either the beam or a leak valve. In either case, the concentration of one reactant is held effectively fixed, while the

other is depleted. From here, we yield the pseudo-first-order reaction rate constant, which takes a second order reaction and simplifies it to a first order rate equation.

$$\frac{d[A]}{dt} = -k[B][A]$$

$$[A] = [A]_0 e^{-k[B]t} \quad (2.1)$$

Where $[A]$ and $[B]$ are the concentrations of the scarce and flooded reactants respectively. We can readily identify the rate constant $k = ([B]\tau)^{-1}$, with dimensions cm^3/s . The reactions discussed in this thesis are exclusively of the pseudo-first-order.

2.1 Average Dipole Orientation Theory (ADO)

Under the understanding that the reactions of interest follow a pseudo-first order model, we are only considering single collisions between the two reactants. To figure out the characteristic rate of the rate constant k , we want to model the interaction between the reactants, whether it be neutral-neutral, to ion-dipole. To do this, we consider adiabatic capture theory, a study of the long range potentials between particles to yield a reaction rate constant. A caveat is that the adiabatic capture theory is long ranged, only finding the rate at which a collision will occur, not necessarily when a reaction will happen. The probability of a reaction occurring requires modeling of short range interactions within the reaction complex.

2.1.1 Radially Symmetric Adiabatic Capture Theory

A general method of calculating the rate constant of two particles with a given potential, finding the collisional cross section, which is then averaged over a velocity distribution to find the rate constant.^[59] Starting with the attractive potential, we find that it is a summation

of interactions with coefficients C_n and r dependence n .

$$V(r) = \sum_n -\frac{C_n}{r^n} \quad (2.2)$$

In the center of mass frame, we see that

$$V_{eff} = \frac{l^2}{2\mu r^2} - \sum_n \frac{C_n}{r^n} \quad (2.3)$$

if $n > 2$, we can derive the capture cross-section and rate constant as follows. First, we find the position r_0 corresponding to the maximum of the effective potential, which is the maximum of the centrifugal barrier.

$$\begin{aligned} \frac{\partial V_{eff}(r_0)}{\partial r} &= 0 \\ \therefore r_0 &= \left(\frac{n\mu, C_n}{l^2} \right)^{1/n-2} \end{aligned}$$

Substituting r_0 back into equation 2.3, we find the maximal value of the effective potential:

$$V_{eff}(r_0) = \left(\frac{l^2}{\mu} \right)^{\frac{n}{n-2}} \frac{n-2}{2n} (nC_n)^{-\frac{2}{n-2}} \quad (2.4)$$

This then defines the energy necessary for a collision, for if E_{col} exceeds $V_{eff}(r_0)$, the reactants will be able to surmount the centrifugal barrier and collide. Thus, we may define the maximum value for the angular momentum l and the impact parameter b .

$$\begin{aligned} l_{max} &= (\mu n)^{1/2} (C_n)^{1/n} \left(\frac{2E_{col}}{n-2} \right)^{\frac{n-2}{2n}} \\ b_{max} &= \frac{l_{max}}{\mu v} \end{aligned}$$

We can then define a collision cross section dependent on the collision energy:

$$\begin{aligned}\sigma(E_{col}) &= \pi b_{max}^2 \\ &= \frac{\pi}{2} n \left(\frac{2}{n-2} \right)^{\frac{n-2}{2}} \left(\frac{C_n}{E_{col}} \right)^{\frac{2}{n}}\end{aligned}$$

Integrating the collision cross section with a Maxwell Boltzmann distribution yields a generalized rate constant as a function of temperature and n .

$$k(T) = \int_0^\infty v f(v) \sigma(v) dv \quad (2.5)$$

$$= \sqrt{\frac{2\pi}{\mu}} n \left(\frac{2}{n-2} \right)^{\frac{n-2}{2}} C_n^{2/n} (k_B T)^{\frac{n-4}{2n}} \Gamma \left(2 - \frac{2}{n} \right) \quad (2.6)$$

For instance, we are interested in ion-neutral interactions of order $n = 4$.

$$\begin{aligned}C_4 &= \frac{\alpha q^2}{2} \\ k(T) &= 2\pi q \sqrt{\frac{\alpha}{\mu}}\end{aligned} \quad (2.7)$$

Where α is the polarizability of the neutral reactant, and q is the ion charge. The corresponding k value in eq. (2.7) is known as the Langevin rate constant, which is famously temperature independent.

2.1.2 Ion-Dipole Interaction

Unlike the Langevin interaction, the ion-dipole term has an angular term defined with respect to the inter-molecular axis. A few approximations are taken to give an average dipole orientation theory pioneered and expanded on by Su and Bowers.[47, 48] This can also be extrapolated to include quadrupole interactions.[49]

The Langevin term of the ion and ion-induced dipole interaction is as follows:

$$V_L(r) = -\frac{\alpha q^2}{2r^4} \quad (2.8)$$

In the case of the ion-dipole interaction:

$$V_D(r, \theta) = -\frac{q\mu_D}{r^2} \cos(\theta) \quad (2.9)$$

The method outlined in section 2.1.1 finds the rate constant by dealing with a two body problem only needing to consider the r degree of freedom. The inclusion of the θ term complicates this, but to first order, we can parameterize θ as a function of r . What we want to achieve is to write down the potential as such:

$$\begin{aligned} V(r) &= -\frac{\alpha q^2}{2r^4} - \frac{q\mu_D}{r^2} \cos(\bar{\theta}(r)) \\ \bar{\theta} &= \frac{\int \theta P(\theta) d\theta}{\int P(\theta) d\theta} \end{aligned} \quad (2.10)$$

Where $P(\theta)$ is the probability of finding the dipole oriented with angle θ . To determine the average orientation of the dipole, we consider the following cases:

1. $P(\theta)$ is inversely proportional to the angular velocity:

$$P(\theta) \propto 1/\dot{\theta}$$

2. An orientation has a probability weighted by the circumference of an angle:

$$C = 2\pi l \sin(\theta)$$

$$P(\theta) \propto \sin(\theta)$$

The angular probability is proportional to both effects:

$$P(\theta) \propto \frac{\sin(\theta)}{\dot{\theta}} \quad (2.11)$$

We can relate the angular velocity to the angular kinetic energy and the total energy in the system:

$$KE_{rot} = \frac{1}{2}I\dot{\theta}^2$$

$$E_{tot} = KE_{rot} + V_D \quad (2.12)$$

Redefining equation 2.11 with equation 2.12, we find:

$$P(\theta) \propto \frac{\sin(\theta)}{\sqrt{E_{rot} - V_D}} \quad (2.13)$$

Combining equations eqs. (2.13) and (2.10) yields a total averaged dipole orientation.

$$\bar{\theta} = \frac{\int \frac{\theta \sin(\theta) d\theta}{\sqrt{E_{rot} + q\mu_D/r^2 \cos(\theta)}}}{\int \frac{\sin(\theta) d\theta}{\sqrt{E_{rot} + q\mu_D/r^2 \cos(\theta)}}} \quad (2.14)$$

From here, two situations arise:

1. $E_{rot} = E_1 < \frac{q\mu_D}{r^2}$: There is not enough rotational energy to overcome the dipole locking. The solution is oscillatory, but θ has an r dependent bound. We let the maximal capture angle that rotational energy E_1 allows be defined as K .

$$E_1 = -\frac{q\mu_D}{r^2} \cos(K)$$

When substituted into equation 2.14, we find:

$$\bar{\theta}_1 = \frac{\int_0^K \frac{\theta \sin(\theta) d\theta}{\sqrt{\cos(\theta) - \cos(K)}}}{\int_0^K \frac{\sin(\theta) d\theta}{\sqrt{\cos(\theta) - \cos(K)}}} \quad (2.15)$$

After some math (something something integration by infinite series) and get a result of:

$$\bar{\theta}_1 = \frac{2\sqrt{2}A}{\sqrt{1 - \cos(K)}}$$

where $A \equiv \int_0^{\pi/2} \frac{a^2 \cos(\phi)^2 d\phi}{\sqrt{q - a^2 \sin(\phi)^2}}$

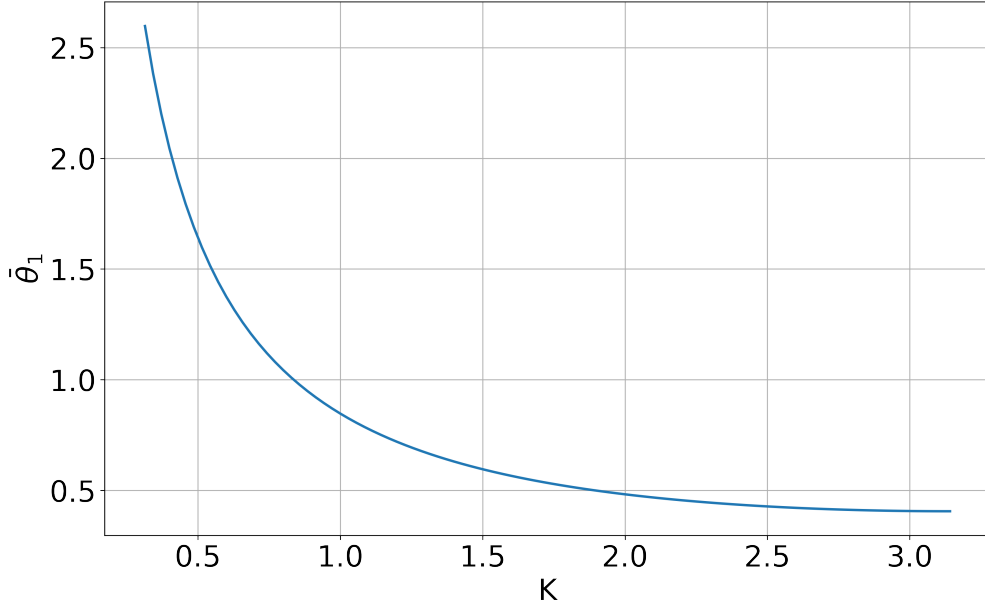


Figure 2.1: Numerical solutions for eq. (2.15) as a function of maximum angle K . In the limit of large K , we find an intuitive solution where θ_1 averages towards 0.

2. $E_{rot} = E_1 > \frac{q\mu_D}{r^2}$: The rotational energy is enough to overcome the dipole locking and θ can swing around in a complete circle

$$\bar{\theta}_2 = \frac{\int_0^\pi \frac{\theta \sin(\theta) d\theta}{\sqrt{E_2 + q\mu_D/r^2 \cos(\theta)}}}{\int_0^\pi \frac{\sin(\theta) d\theta}{\sqrt{E_2 + q\mu_D/r^2 \cos(\theta)}}} \quad (2.16)$$

We no longer have bounds on the angles the dipole is allowed over, but the behavior is still dependent on the strength of the internal energy and dipole force.

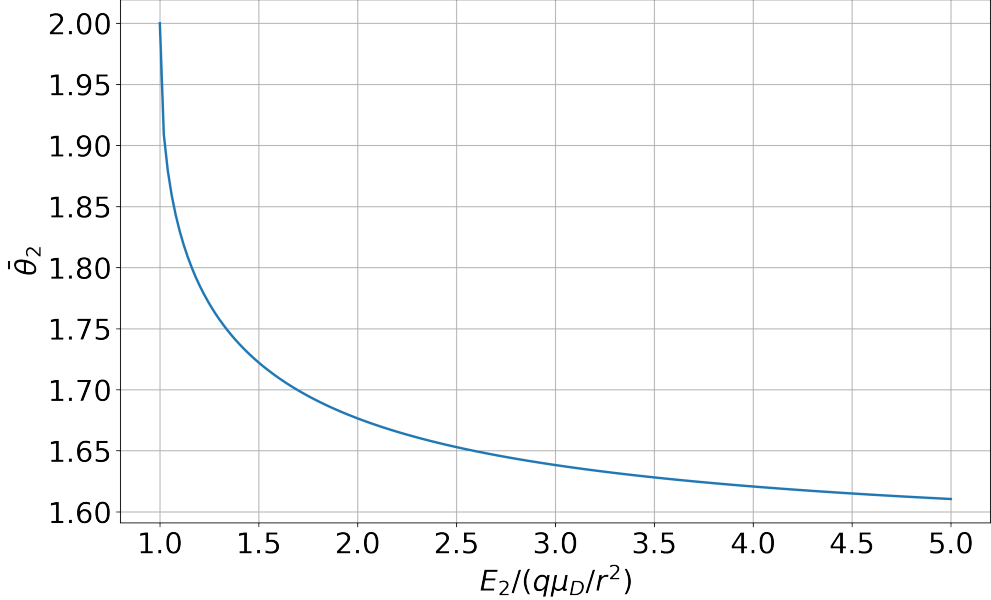


Figure 2.2: Numerical solution to eq. (2.16) as a function of the ratio of rotational energy and the monopole-dipole term. The low ratio behavior is not immediately obvious, but the greater the ratio between the rotational energy and monopole-dipole term, the more θ_2 tends towards $\pi/2$.

Let's say we have the forms for $\bar{\theta}_1$ and $\bar{\theta}_2$, we want to write down the full form of θ . We can combine the two weighted by the probability of each as a function of internal energy.

$$\bar{\theta}(r) = \bar{\theta}_1(r)F_1 + \bar{\theta}_2(r)F_2 \quad (2.17)$$

Where the weightings F_i are found via:

$$P(\epsilon)d\epsilon = \frac{1}{k_B T}e^{-\frac{\epsilon}{k_B T}}d\epsilon$$

For diatomics, the energies of rotational states is defined as:

$$\epsilon = B_e J(J+1)$$

Where the rotational constant is $B_e = \frac{\hbar^2}{2\mu R^2}$, μ is the reduced mass of the molecule, and R is the inter-nuclear separation. We can then use equation 2.5 and get a cross section and

rate constant. The form is similar to that of just a Langevin term, but now with a dipole interaction term added onto it.

$$k_{ADO} = \frac{2\pi e}{\sqrt{\mu}} \left(\sqrt{\alpha} + C\mu_D \sqrt{\frac{2}{\pi k_B T}} \right) \quad (2.18)$$

Where C is the dipole locking constant. All of the terms aside from C come from the integration over a Boltzmann distribution in v . C itself can be numerically solved by iteratively integrating over combinations of μ_D and α .[47][51]

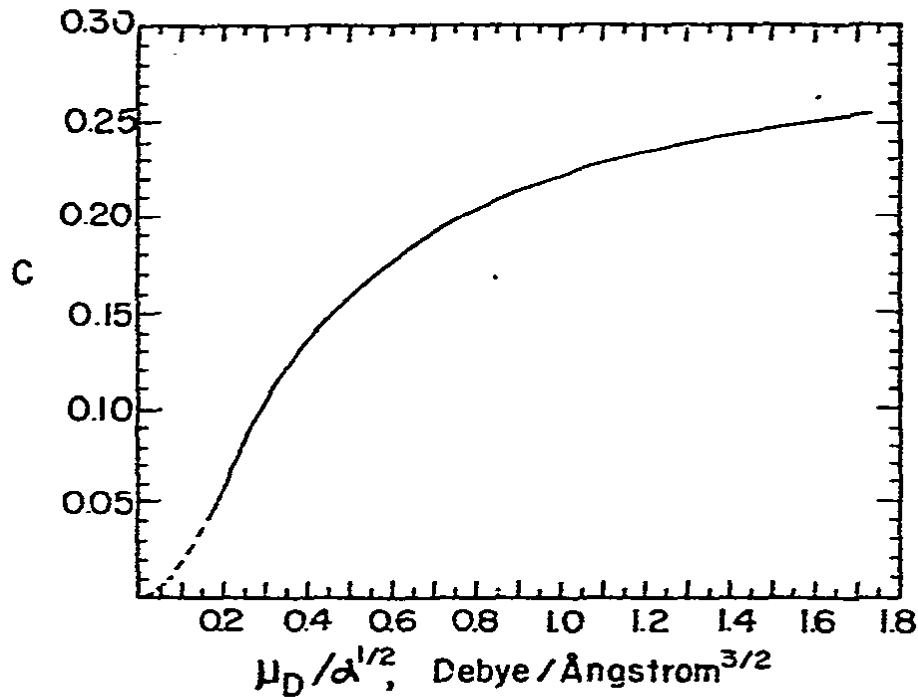


Figure 2.3: Dipole locking constant C parameterized by the dipole moment μ_D and polarizability α .[47]

CHAPTER 3

The Cryogenic Buffer Gas Beam (CBGB)

To reach reaction temperatures around 10K from a beam of molecules with trapped ions, a cryogenic buffer gas beam (CBGB) of neon with entrained water is employed. Numerous other methods of creating cold beams of molecules exist, from Zeeman decelerators [31], to Stark decelerators. CBGB's in particular have the benefit of being species agnostic, where the resultant beam properties are not dependent on the target species at hand, rather, the buffer gas species.

By holding a cell filled with a noble gas above its vapor pressure, a volume of gas can be held at cryogenic temperatures. Other species of molecules or atoms may be introduced into the buffer gas cell via ablation, fill line, etc. The target species particles are then sympathetically cooled via collisions with the cold buffer gas. An aperture at one end of the cell allows for the extraction of the buffer gas and entrained target species into a ballistic beam. Holding the buffer gas cell temperature to above 17 K for neon, and 4 K for helium, in high vacuum allows us to accumulate an appreciable stagnation number density within the cell to produce a beam of entrained target particles.

The properties of interest are a function of the flow regime of the beam, which is determined by the choice of gas, its flow rate, and the dimensions of the cell it is held in. It's convenient to use the Reynolds number at the aperture to characterize the flow regime, which can be written as:

Add
ci-
ta-
tions
for
de-
cel-
er-
a-
tors

Missing
figure

Schematic of CBGB

Figure 3.1: Schematic of target species entrainment within a buffer gas beam cell. With high densities of buffer gas particles, an introduced target species undergoes collisions with the buffer gas such that it cools. At high enough densities, flow dynamics cause the target species to become entrained in the buffer gas flow and are carried out of the cell with greater efficiency.

$$\begin{aligned} Re &\approx \frac{2d_{aperture}}{\lambda} \\ &\approx \frac{8\sqrt{2}\dot{N}\sigma}{d_{aperture}\bar{v}} \end{aligned} \quad (3.1)$$

Where $d_{aperture}$ is the diameter of the aperture and λ is the mean free path of the buffer gas particles.[22] When the Reynolds number is low, $Re < 1$, we find that there are on average > 1 collisions at the aperture, meaning the particles escape with little to no interactions with other particles and is called the effusive regime. At high Reynolds numbers, $Re > 100$, in the supersonic regime, there are many collisions and forward velocity boosting as well as internal velocity distribution narrowing occurs. In between, we find the intermediate regime, where we observe the onset of hydrodynamic entrainment of target species with mild forward velocity boosting. In all cases, the gasses inside the cell at thermal equilibrium follow the Maxwell-Boltzmann distribution.

$$f(v) = \left(\frac{m}{2\pi kT}\right)^{3/2} 4\pi v^2 e^{-\frac{mv^2}{2kT}} \quad (3.2)$$

Where the mean velocity is:

$$\bar{v} = \sqrt{\frac{8k_B T}{\pi m}} \quad (3.3)$$

The goal for our beam is three fold, to produce a **slow, dense, localized** beam of our target species that can make it down into the ion trap region. The velocity and density of the target species are both related to the flow regime of the buffer gas, and to reach our goal, it's ideal for us to aim for a beam that operates within the intermediate regime, between effusive and supersonic. Producing a localized beam ensures that we are introducing the minimal unwanted gas load into the ion trap chamber, and that we may quickly and reliably shutter the beam to start and stop the chemical reactions. In the following sections, we will discuss the design of the apparatus and characterization of the beam density, extraction, forward velocity, and shuttering.

3.1 Design

The CBGB apparatus design has various stages, a room temperature 300 K outer aluminum vacuum chamber, onto which a Pulse Tube Refrigerator (PTR) is mounted, an aluminum radiation shield mounted to the 40 K PTR cooling stage, and an inner copper cryopumping shield and experimental cell connected to the 4 K PTR cooling stage. Connected to the vertical vacuum chamber, a "stem" region protrudes out from the beam side as seen in figures figs. 3.2 and 3.3 where a large Agilent Varian-V 551 turbo pump evacuates the entire volume. The beam comes out of the experimental cell and shield, through a set of apertures, into the stem region where skimmers and shutters are mounted to manipulate the beam.

A Cryomech PT415 PTR with a remote head option was attached to the top plate of the vacuum chamber with a large bellows mount to isolate the chamber from the mechanical vibrations caused by the PTR motor head. The chamber was pumped down to normal operating pressures, where then 4 retaining screws were tightened to just above the bellows' compressed height. This maintains mechanical decoupling between the outer vacuum

chamber and the PTR while running.

We want to minimize the mechanically coupling onto the PTR due to the fragility of the pulse tube walls; small amounts of force applied onto a mechanically connected component would risk torquing the walls to break. Thus, all components inside the CBGB are mechanically connected to the top plate of the vacuum chamber via 8-32 stainless steel (SS316) threaded rods. Thermal connections are made with copper braids welded onto L-shaped brackets that mount between platforms secured to the PTR cooling stages, and the shields.

Not only are all the inner shields connected to the top plate, but so are the feedthroughs including gas fill lines. This ensures that any and all connections made into the CBGB are not disturbed when opening the outer vacuum chamber to expose the inner components.

The design of the shields themselves is informed by the choice of buffer gas species. Commonly used buffer gas species are helium and neon, while helium provides a slower beam, it is more technically challenging to implement. The main technical difference comes from the cryopumping requirements; where neon only needs surfaces to be held at 17 K to continually cryopump, helium requires (coconut) activated charcoal held at 4 K or lower. Aside from the difficulty of getting surfaces to 4 K these volumes of charcoal can become saturated and require purging, limiting one's operating time (few hours). On the other hand, neon ice formed on the 17 K surface will act as a cryopump for more neon gas, allowing for many hours of continuous operation with no appreciable build up of background gas. Our experiment uses neon as a buffer gas for its technical simplicity, the lower achievable temperature with the helium does not yield dramatic gains in the final reaction temperature.

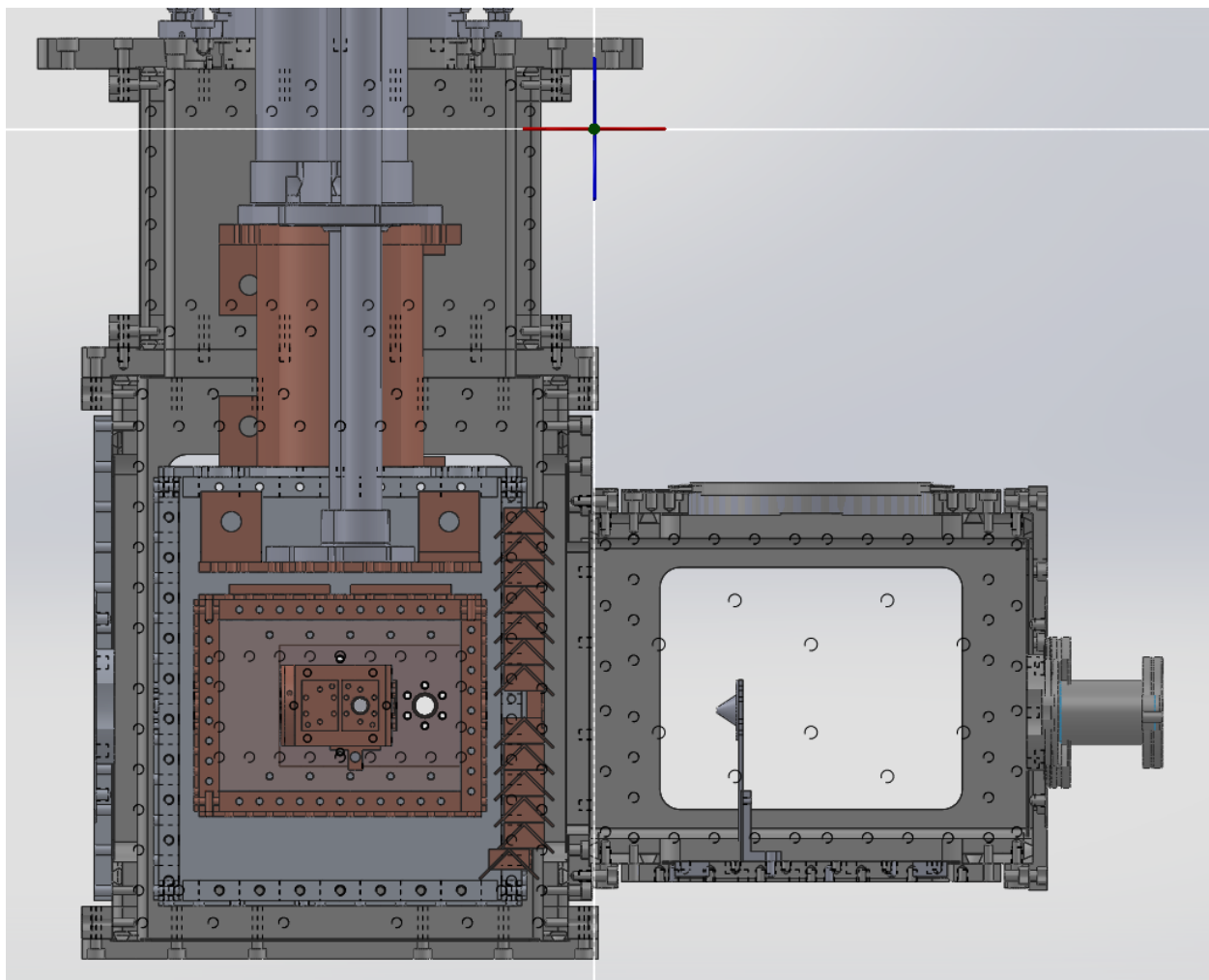


Figure 3.2: Cross sectional view of CBGB in solidworks. Components include copper sheath for PTR, aluminum radiation shield with chevron baffles, copper shield and experimental cell, and skimmer mounted in stem chamber. The baffles allow for gas to flow into the cold region of the beam apparatus, while preventing 300 K black body radiation from hitting the inner shield and cell.

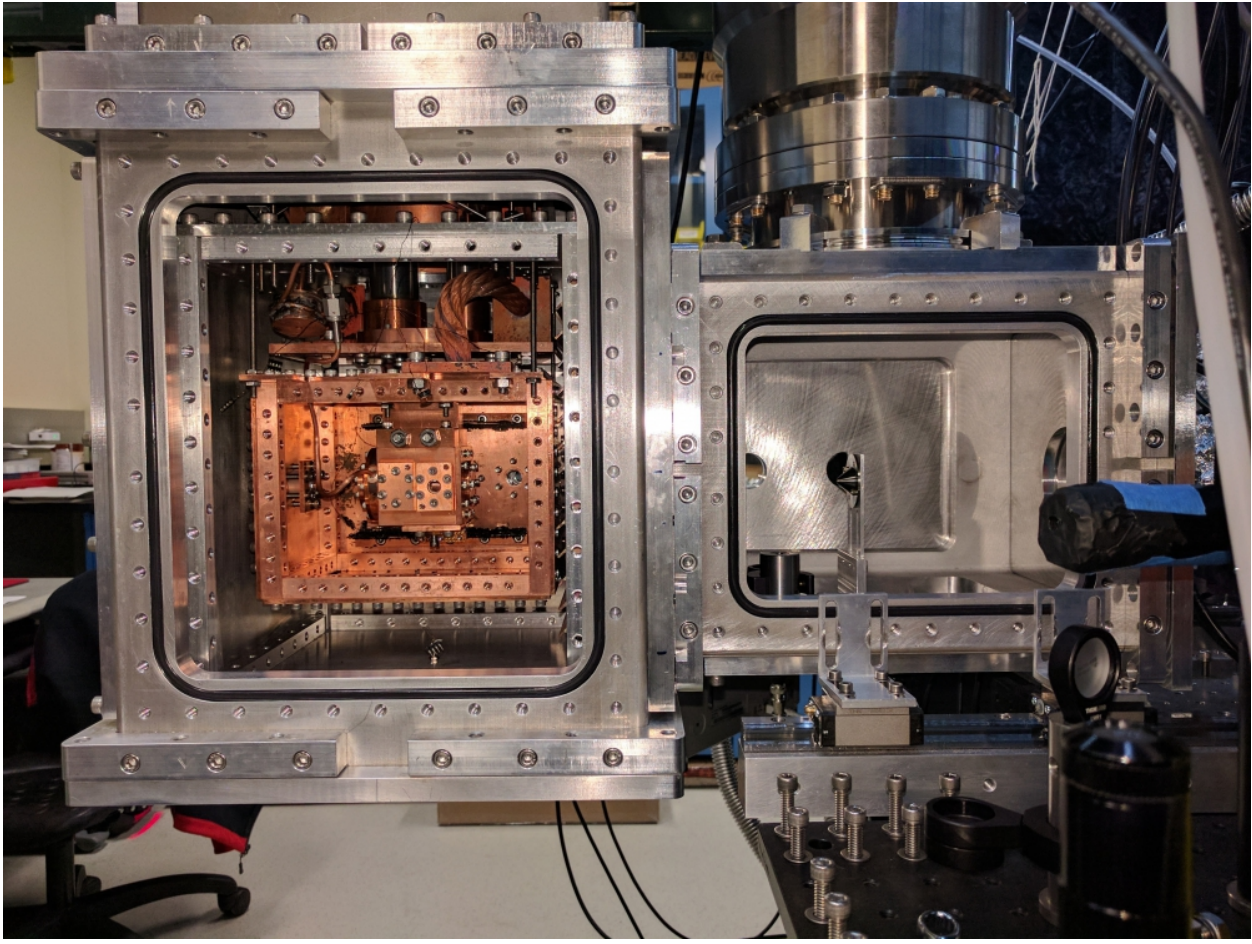


Figure 3.3: Cross sectional view of CBGB with side walls removed from the outer vacuum chamber, 40 K aluminum radiation shield, and inner 4 K cryopumping shield exposing the inner experimental cell. A skimmer is mounted in the stem region.

3.1.1 Heat Load and Thermal Conductivity

To produce a beam of cold particles, various components need to be held within specific temperature ranges to ensure proper operation. Considering neon as the buffer gas species of choice, we maintain the experimental cell at 20 K to prevent the neon from freezing to the walls and maintain a high stagnation density that allows for tuning of the flow regime. Conversely, we need the cryopumping shield surrounding the experimental cell to maintain

a temperature < 17 K so that the neon that escapes the cell is readily captured, as the turbo connected to the stem chamber cannot keep up with the gas load. A lack of proper cryopumping results in high densities in the chamber, which scatters the beam.

The PTR 40 K cooling stage has 40 W of cooling power, while the lowest 4 K stage has only 4 W. The low cooling power of the lowest stage means that extra care is needed to minimize the heat transfer to the stage from the higher temperature regions including black body radiation and conducted heat from high temperature surfaces.

Material choices used in the CBGB are dictated by their thermal conductivity down to the temperature ranges of interest. At room temperature, thermal conductivity (k) of a material is dominated by transfer of energy via phonons through the material. In this regime, different alloys and purities of a material do not greatly affect the conductivity. But once we enter cryogenic temperatures, the conductivity is dominated by electron motion through the material, meaning that purer samples have fewer imperfections to scatter off of, yielding higher conductivities.

Al 6061 was chosen for the radiation shield for its thermal conductivity ($k_{Al6061}(T = 40$ K) = 70 W/(m K)[?]), ease of machining, as well as lightweight properties. The thermal mass of the aluminum shield coupled with its relatively lower thermal conductivity (compared to Cu 10100) means the cool down of this region limits the cool down process to 6 hr until at workable temperatures. The face of the aluminum shield on the outgoing beam side was fitted with a set of stacked chevron baffles as seen in figure 3.2. The baffle design blocks stray light from entering the radiation shield, while enabling gas to pass from the enclosed shields into the stem region, preventing high density regions from forming and scattering the beam. Conversely, the baffles allow for gas within the stem region to reenter the cryogenic shields and facilitate cryopumping of stray particles.

The copper region contains the experimental cell, enclosed by a copper shield that acts as a cryopumping surface at the appropriate temperatures. At cryogenic temperatures, it's convenient to characterize the conductivity of a copper with the residual resistance ratio ($RRR = \frac{R(T=295 \text{ K})}{R(T=4 \text{ K})}$), where $R(T)$ is the measured resistance at temperature T , which can be

related to the thermal conductivity with the Wiedemann-Franz Law.^[?] Cu 10100, or oxygen free copper, was chosen for these components for its high thermal conductivity through to 4 K, $RRR = 2000$, $k_{Cu10100}(4 \text{ K}) = 10^4 \text{ W}/(\text{m K})$ compared to ^[?].

Because it is heat sunk into the same cooling stage as the experimental cell, the copper shield does not act as a radiation shield for it does not redirect the heat load away from the experimental cell's cooling surfaces. For the experimental cell to hold an appreciable vapor pressure, while the thermally linked shield acts as a cryopumping surfaces, the two components will need to held at different temperatures. The experimental cell is held at a higher temperature than that of the cryopumping shield with a resistive heater, which is monitored and controlled with a temperature sensor diode (DT-670) and a Lakeshore controller (Model 325). A SS316 ($k_{SS316}(T = 40 \text{ K}) \approx 7 \text{ W}/(\text{m K})$) stand off is used to create a poor thermal bridge between the two regions, allowing for a constant thermal gradient.

The main heat loads onto the system are those from the black body radiation, as well as the stainless steel rods supporting the shields from the top mounting plate. The temperature over the system may be determined by solving the heat/diffusion equation given proper boundary conditions. We use Fourier's Law to approximate the conductive heat loads through individual pieces

$$\dot{Q} = \frac{A}{l} k \Delta T \quad (3.4)$$

Where \dot{Q} is the rate of heat transfer, A is the cross sectional area of the component in question, l is the length of the component, and k is the thermal conductivity of the material. In general, we should be using the integral form where we have a temperature dependent thermal conductivity, $k(T)$, but approximate it to be constant. The main conductive heat loads come from the SS316 rods that mechanically anchor the shield components to the top chamber plate. On the 4 K cryopumping shield, there are 4 such rods, in total, contributing $\approx 60 \text{ mW}$ of power to the 4 K cooling stage.

Aside from the conductive heat load, black body radiation is the main source of heat load onto the cold regions. We describe the power radiated from a source with the Stefan-

Boltzmann law:

$$\dot{Q} = A\epsilon\sigma T^4 \quad (3.5)$$

Where A is the area of the emitting object, ϵ is the emissivity of the surface, and σ is the Stefan-Boltzmann constant. To find the power incident between two surfaces (1, 2) though, we find the form to be:

cite
book

$$\dot{Q} = \sigma A(T_1^4 - T_2^4) \frac{\epsilon_1 \epsilon_2}{\epsilon_1 + \epsilon_2 - \epsilon_1 \epsilon_2} \quad (3.6)$$

In order to characterize the beam inside the CBGB, fused silica windows were mounted onto every shield to allow for optical access. These may pose a problem, as this line of sight allows for radiation coming from room temperature sources to heat up the inner components. The peak wavelength of a black body source at a temperature T is described by Wien's displacement law:

$$\lambda_{max} \approx \frac{2900}{T} \mu\text{m} \quad (3.7)$$

One can see the peak wavelength from a room temperature source is around $93 \mu\text{m}$, which is readily blocked by our fused silica windows. In total, the maximal approximate incident black body power onto the 4 K region, including a 20% fudge factor, is on the order of 200 mK.

talk
about
num-
bers

3.1.2 Gas Fill Lines

To have a functioning beam, we need to introduce both the buffer gas as well as the target species gas from room temperature without over burdening the cooling stage, or plugging the fill lines. The buffer gas fill line is made of thin walled SS316, minimizing the thermal connection between the room temperature mounting and the cold experimental cell. It is

thermally anchored to the 40K cooling stage and then brazed onto a plate that mounts to the experimental cell. To avoid local freezing of the buffer gas, the tubing must avoid cryopumping shield as contact.

More care must be taken for the design of the water fill line, as it cannot make contact with any mildly cooled metal surface for fear of local freezing. The mating of the fill line to the experimental cell must also prevent excessive heat loads onto the cell while still enclosing the back side to preserve beam flux. With the design help of David Patterson, we utilize a thick walled 1/8" copper tube, with the tip bent at 90°, that enters from the bottom of the CBGB (figure 3.4), through the shields, into the back of the experimental cell. The fill line can be manipulated from the bottom of the chamber and the insertion depth into the cell can be adjusted before pump down. By slathering the o-ring at the bottom of the chamber with silicon vacuum grease, one may also adjust the tubing in situ, but the CBGB should be gated off from the rest of the experiment.

Leaving the back of the cell open eliminated conductive heat transfer between the fill line and the cell, but did not allow for a reliable beam. Ice readily formed on the nearby copper surfaces and slowly closed the back opening, decreasing the effective $A_{aperture}$ of the cell, thus changing the flow properties. The back was replaced with a 0.001" film of kapton with a cross cut into the middle for the fill line as seen in figure 3.5. The poor thermal conductivity of kapton (0.5 W/(m K)) ensures minimal conductive heat load to the cell, prevents ice from forming, while also closing the back of the cell. The beam may be run continuously with water entrained in the neon buffer gas for over 10 hours without any change in beam properties. Collisions with buffer gas particles within the cell transferring heat between the fill line and cell walls added < 0.05W of heat load. Solving the integral form of Fourier's Law in cylindrical coordinates (3.8), we find that the heat load through the kapton is only 0.019 W.

$$\dot{Q} = \frac{2\pi k l (T_1 - T_2)}{\ln(r_2 - r_1)} \quad (3.8)$$



Figure 3.4: The water fill line, sealed by an ultratorr fitting and heated by nichrome wire. A shut off valve and vernier valve are used to regulate the flow of water into the buffer gas cell.

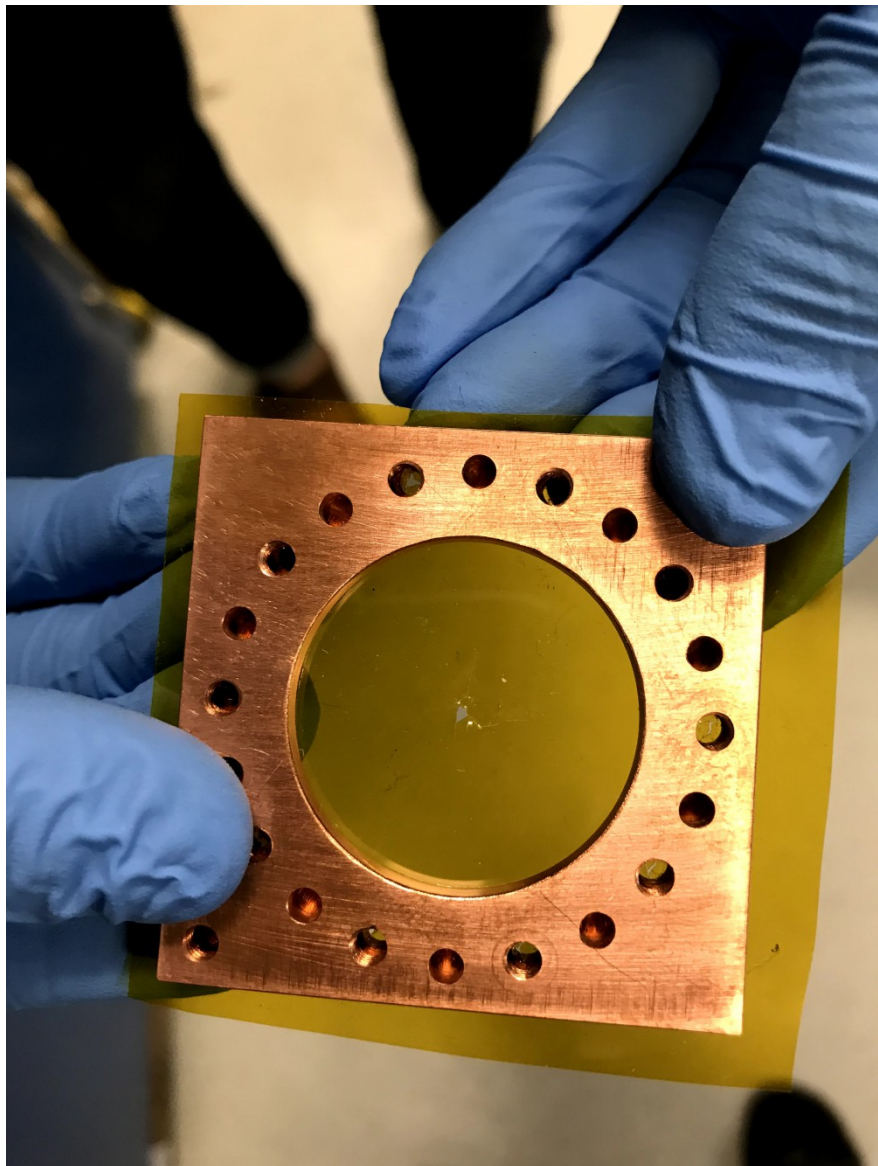


Figure 3.5: A kapton film serves as the back wall of the buffer gas cell with a hole punctured for the insertion of the water fill line. The kapton surface seals the back of the cell for a stronger forward beam, while limiting the heat load from a room temperature fill line, and resisting ice formation allowing for continuous and consistent operation with water for over 10 hours.

3.2 Beam Density and Extraction

We need to have a fairly dense beam of our target species to reach the ion trap center in order to get a reasonable signal to noise of the cold molecule reaction as opposed to the warm background reactions. A dense beam coupled with good cryopumping ensures that the signals seen are primarily, if not solely due to the introduction of the cold beam.

The downstream properties of a beam all start with the buffer gas stagnation density within the experimental cell. The stagnation density is the steady state buffer gas density that is determined by the physical dimensions of the cell, including the aperture, and the gas throughput, or number flow rate going in. Experimentally, it's preferable to use volumetric flow rates when operating the apparatus, so for calculations, that needs to translate to number flow rate using the ideal gas law:

$$\dot{N} = \frac{Pf}{k_B T}$$

where P is pressure and f is the volumetric flow rate, this translates to about 4×10^{17} particles/s⁻¹ for 1 SCCM of gas flow. By solving for the number density in the flow out of an aperture with molecular flow, we find that the stagnation density within the cell can be shown as:

$$C_{ap} = A \frac{\bar{v}}{4}$$

$$n_b = \frac{4\dot{N}}{A_{aperture} \bar{v}} \quad (3.9)$$

In general, buffer gas beams operate with stagnation densities around $10^{15} - 10^{17}$ cm⁻³. Outside of the cell, we can describe the density of the beam as a function of distance. [33]

$$n(z) = \frac{n_0}{2} \left(1 - \frac{z}{\sqrt{z^2 + a^2}} \right) \quad (3.10)$$

Where z is the distance from the aperture into the vacuum side, n_0 is the initial number density, a is the radius of the aperture. In the far-field, this goes to:

$$n(z) = \frac{n_0 a^2}{4z^2}$$

But there is something that we must consider, that is that we aren't seeing the full aperture while we are at all locations, we are actually seeing an appended area due to the inclusion of apertures and skimmers in the way. While only n_0 is only dependent on the aperture size of the cell, $n(z)$ will have a set value defined by the smallest aperture in the beam path. For us, although our cell aperture is ≈ 9 mm in diameter, we have multiple apertures and skimmers in the way, the smallest of which is a skimmer from Beam Dynamics with a diameter of 2 mm.

Sympathetic cooling occurs through collisions between the hot target species being introduced and the cryogenic buffer gas particles. We may consider each hard sphere collision to transfer heat from the hot target species (T_s) to the cold buffer gas at constant temperature (T_b).

$$\Delta T_s = -\frac{T_s - T_b}{k}$$

Where $k \equiv \frac{(m_b + m_s)^2}{2m_b m_s}$. For the N^{th} collision, we can write the change in temperature:

$$T_s(N) - T_s(N-1) = -\frac{T_s(N-1) - T_b}{k}$$

For large values of N , where the change in temperature becomes small, we can turn the discrete equations into a differential form.

$$\frac{dT_s(N)}{dN} = -\frac{T_s(N) - T_b}{k}$$

Which we can solve with the condition that $T_s(0) = T_0$

$$\begin{aligned} \frac{T_s(N)}{T_b} &= \left(\frac{T_0}{T_b} - 1 \right) e^{-\frac{N}{k}} + 1 \\ &\approx \frac{T_0}{T_b} e^{-\frac{N}{k}} + 1 \end{aligned}$$

Assuming an ablation loading process in which $T_0 = 1 \times 10^4$ K, we find that it still only takes ≈ 12 collisions to thermalize the target species within a factor of 2 of the buffer gas temperature. In general ≈ 100 collisions are needed to relax rotational states to the same range. Vibrational degrees of freedom may take upwards of 10^4 collisions to fully thermalize if the elastic collision energy is much lower than the internal vibrational level.

By finding the mean free path, we can consider the characteristic length the particles travel to be thermalized with the buffer gas, this is then compared to the characteristic length of the cell to determine the effectiveness of the cooling.

$$\lambda = \frac{A_{aperture} \bar{v}}{4f\sigma\sqrt{m_s/m_b}}$$

If a species is introduced into the buffer gas cell that has a lower vapor pressure than that is allowed at the current temperature, it will be lost when it comes in contact with the cell walls. The rate of this loss can be described as the characteristic time of diffusion of a particle in the buffer gas to the physical dimensions of the cell set the diffusion time constant:

$$\tau_{diff} = \frac{16}{9\pi} \frac{A_{cell} n_{0,b} \sigma}{\bar{v}} \quad (3.11)$$

where σ represents the collisional cross section for the buffer gas with the target species. On the other hand, we have the characteristic pump out time given by the conductance of a cell aperture:

$$\tau_{pump} = \frac{4V_{cell}}{\bar{v} A_{aperture}} \quad (3.12)$$

By combining equations eqs. (3.11) and (3.12), we can get a dimensionless ratio, γ that characterizes the extraction fraction out of the cell.

$$\gamma = \frac{\tau_{diff}}{\tau_{pump}} = \frac{\sigma f}{L_{cell} \bar{v}} \quad (3.13)$$

Notice that the γ factor does not depend on aperture size, this is generally true, but increasing the aperture size will lower your number density within the cell, which then influences the characteristic length scale of thermalization. Larger apertures thus run the risk of not allowing your particles to fully thermalize in rotational/vibrational states. But decreasing the aperture size can make alignment as well as controlling the number density more difficult, as finer control over the flow rate is necessary for equivalent flow regimes.

Using equations eqs. (3.13) and (3.9), knowing the physical dimensions of the experimental cell, we find that we may derive theoretical characteristics of the buffer gas beam. During normal operation, our main control over the buffer gas beam is the manipulation of the Ne flow rate, so as a function of buffer gas flow rate (f), we may see how key properties are affected.

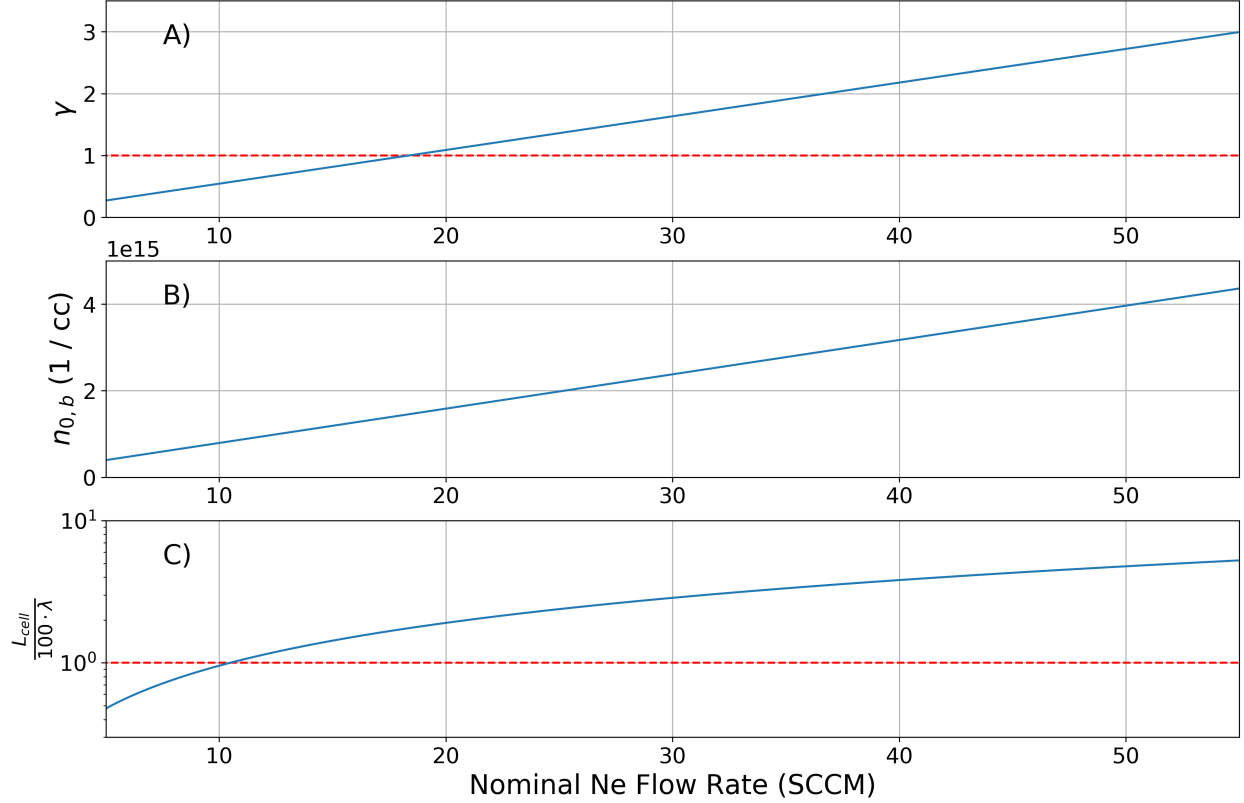


Figure 3.6: Theoretically derived buffer gas beam properties of interest given the physical dimensions of our cell in particular: $d_{aperture} = 9$ mm. A) γ extraction ratio, dotted red line indicates $\gamma = 1$ where hydrodynamic entrainment begins. B) Number density of buffer gas species within the experimental cell, given an enclosed back wall. The density of target species introduced should stay under 1% of the buffer gas density for other properties to hold. C) Number of collisions a target species particle would expect before extraction out of the cell, the dotted red line indicates 100 collisions before extraction, when rotational degrees of freedom are characteristically thermalized.

3.2.1 Direct Beam Measurement and Parameterization

Although we can make statements about the properties of the buffer gas itself in the beam, we are most interested in the properties of the target species introduced into the cell. In

particular, understanding the extraction ratio γ , as well as the velocity, gives us a good handle on the target species characteristics.

To observe the extraction of the target species from the cell, a residual gas analyzer (RGA) is used to determine the density of the beam in the ballistic regime upstream from the ion trap. To ensure the highest possible signal, the Swagelok vernier flow valve used to regulate water vapor flow into the cell is fully opened. During normal operation of the beam in conjunction with the ion trap, the valve is set to a much smaller opening to ensure the properties of the beam are dominated by the buffer gas species, as well as to control the reaction rates.

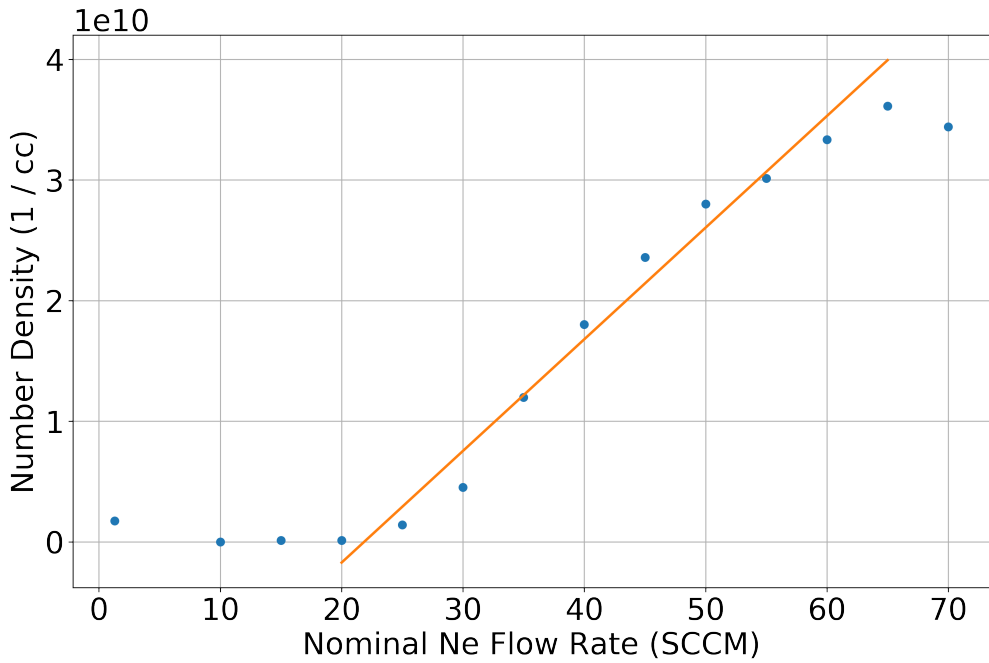


Figure 3.7: Fitted linear behavior of H_2O entrained in a Ne buffer gas beam 30 cm from cell aperture. The onset of hydrodynamic entrainment seems to occur around 20 SCCM up through 60/65 SCCM where the H_2O extracted into the beam has a clear linear form of $(9.2 \times 10^8 \text{ cm}^{-3}/\text{SCCM})f - 2 \times 10^{10} \text{ cm}^{-3}$.

We find that theoretical calculations and experimental results agree that the onset of hydrodynamic entrainment occurs at a buffer gas flow rate of ≈ 20 SCCM. We can combine

the results here with equations eqs. (3.3), (3.9) and (3.10) to map out beam densities subject to all other possible parameters we may want to adjust, over our entire experimental apparatus. We start by scaling a combination of equations eqs. (3.9) and (3.10) by α , a buffer gas to target species density scaling factor.

$$n(z) = \alpha \frac{f}{A_{\text{aperture}} \bar{v}} \left(1 - \frac{z}{\sqrt{z^2 + a^2}} \right)$$

But this only holds true for the region in which the number density is linearly dependent to the buffer gas flow rate, not over all possible ranges; we've seen that the target species only behaves linearly in the hydrodynamic regime. This means that we should be equating the function of $n(z)$ with the linear fit performed on the data for the parameters the data was taken at.

$$mf + b = \alpha \frac{f}{A_{\text{aperture},0} \bar{v}_0} \left(1 - \frac{z_0}{\sqrt{z_0^2 + a_0^2}} \right)$$

Where $z_0 = 30$ cm, being the distance of the RGA from the cell aperture, and $z = 0 = 2$ mm, for the smallest aperture seen during the experimental run. We also define the experimental scaling factors:

$$\begin{aligned} \alpha &= \frac{m}{\beta} + \frac{b}{\beta f} \\ \beta &= \frac{1}{A_{\text{aperture},0} \bar{v}_0} \left(1 - \frac{z_0}{\sqrt{z_0^2 + a_0^2}} \right) \end{aligned}$$

Thus, we obtain a form that includes experimentally derived scaling factors that allows us to project the target species density over the length of the system.

$$n(z) = \frac{mf + b}{A_{\text{aperture}} \bar{v} \beta} \left(1 - \frac{z}{\sqrt{z^2 + a^2}} \right) \quad (3.14)$$

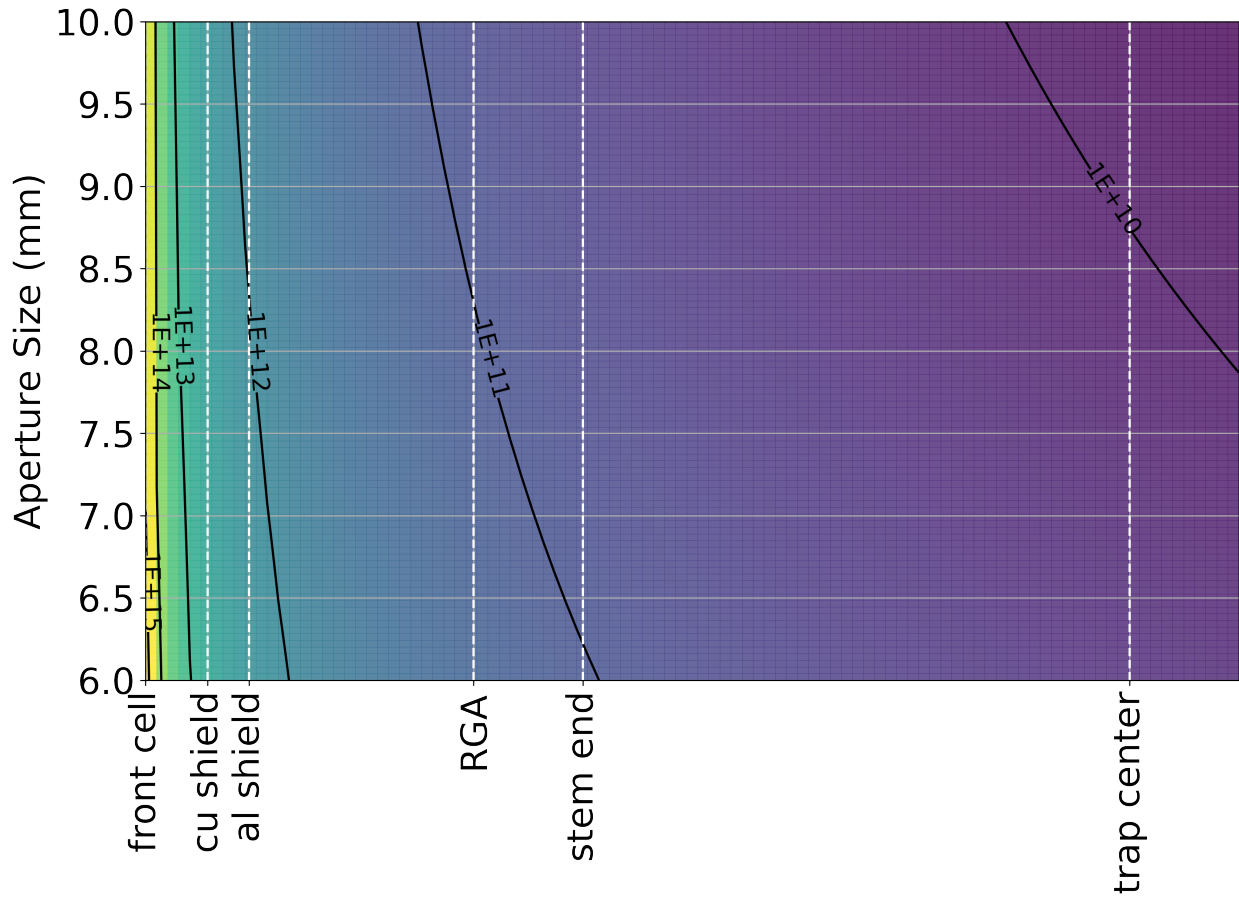


Figure 3.8: Projected beam densities with a Ne flow rate of 30 SCCM with various distances of interest within the chamber. Beam densities shown are without throttling of the H₂O flow valve.

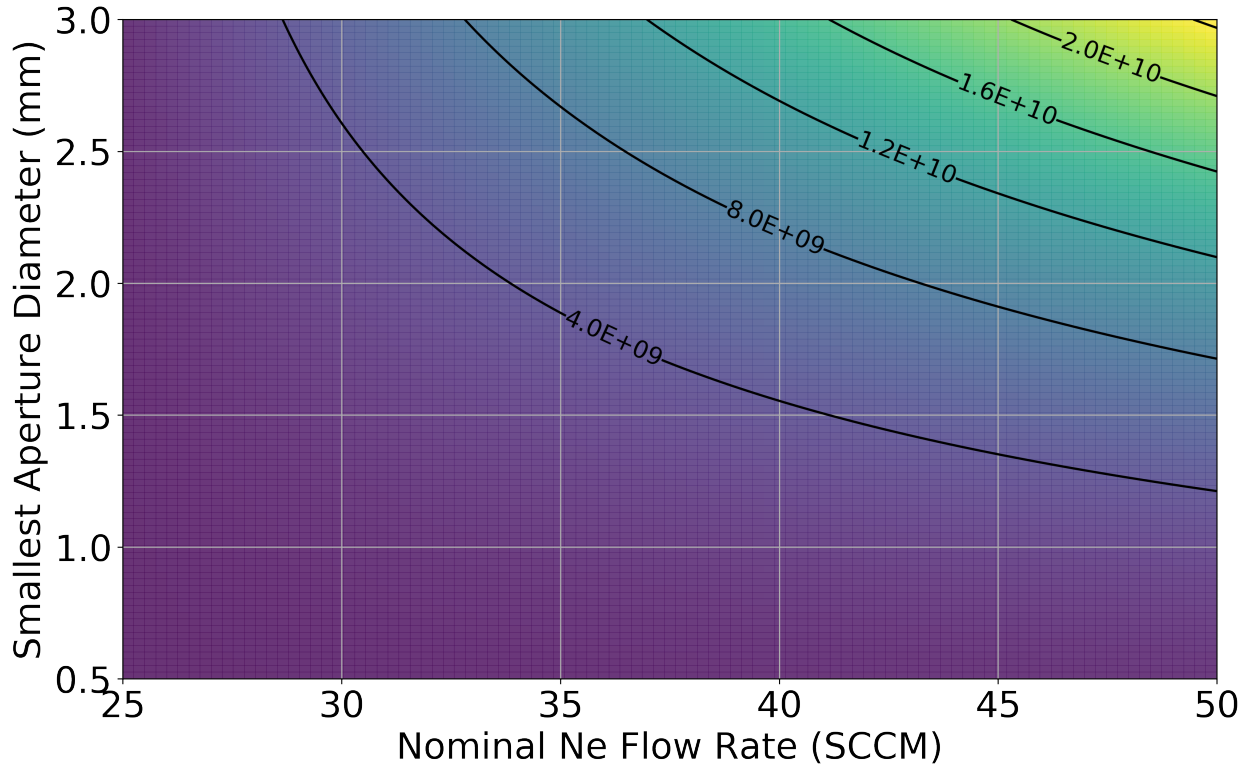


Figure 3.9: Projected beam densities at the trap center over various nominal Ne flow rates and smallest skimmer aperture size. Beam densities shown are without throttling of the H₂O flow valve.

One should not forget the mass dependence in the thermal velocity equation, which leads us to conclude that the choice of the species is a statement of the dominant species in the beam. If we choose to calculate the thermal velocity of the target species found in the beam due to the theoretical thermal velocity of the buffer gas species, that indicates that the beam properties are still dominated by the buffer gas species. At target species/buffer gas ratios greater than 1/100, we may start to see the effects of the target species on not only the beam density, but also forward velocity.

3.2.2 Beam Density at Ion Trap

Determining the water density in the beam at the ion trap is more difficult than in the CBGB and stem region. During normal operation of the CBGB, the RGA in the trap chamber, which is off the beam axis and in a nipple, is unable to detect a change in the background water pressure. We turn to the trapped ions to find an answer.

By introducing water via the CBGB into the chamber with laser cooled Be^+ ions, we observe reactions 5.1 and 5.2 from delayed TOF traces. Knowing the rate constant for this reaction (equation 5.11), we may find the density of the beam. The reaction products are ejected from the trap into the time of flight mass spectrometer (TOF-MS) at various delay times and the integrated ion signal is recorded. Assuming a forward velocity for H_2O upwards of 200 m/s, we have a reaction temperature of ≈ 20 K. The interaction produces reactions 5.1 and 5.2, which were experimentally determined to react at temperature (T) and ${}^2\text{P}_{3/2}$ state excitation fraction (P) at a rate defined by equation 5.11.

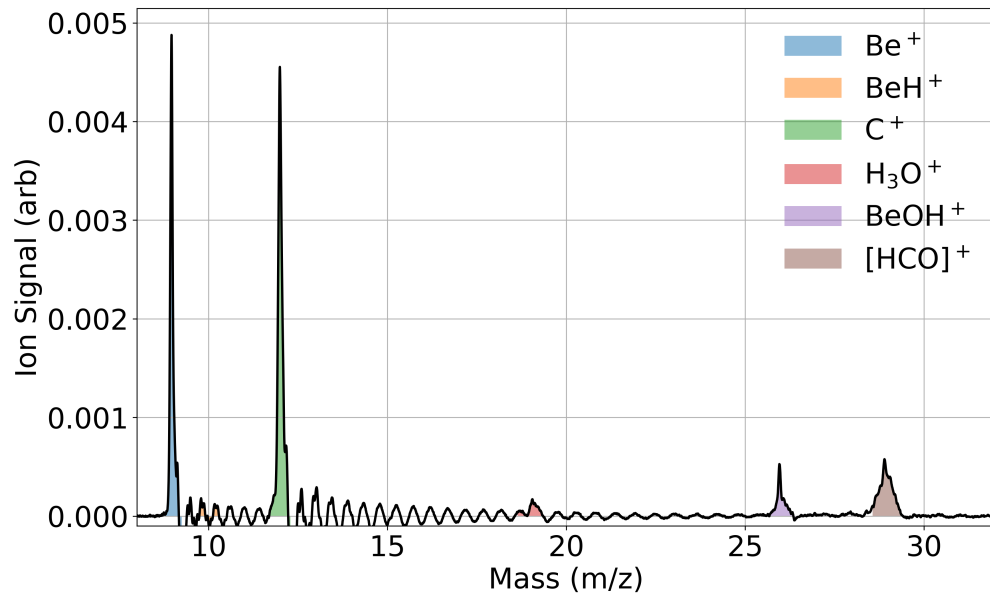


Figure 3.10: text

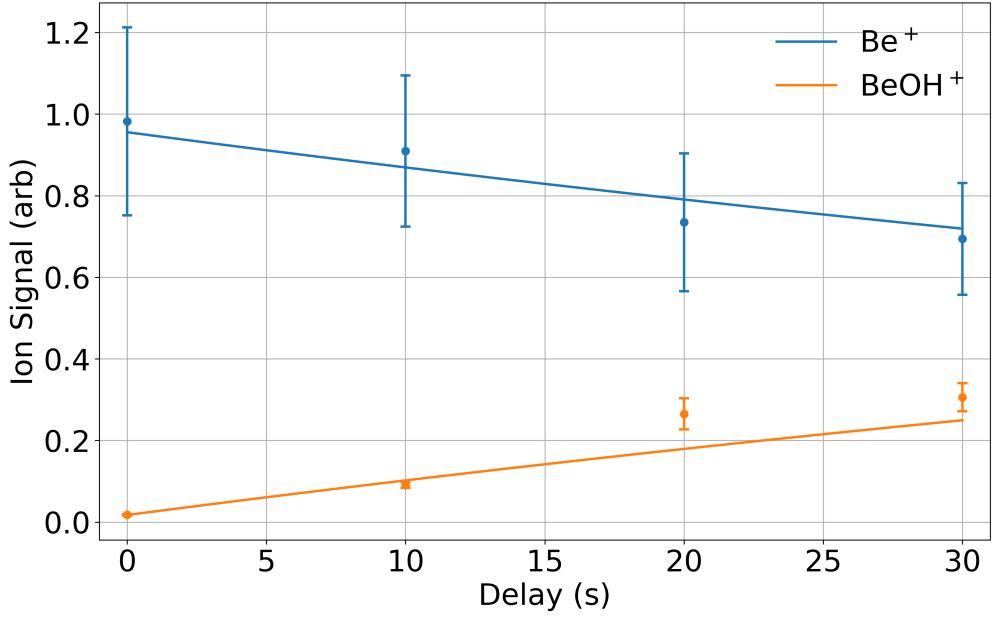


Figure 3.11: Be^+ decay and BeOH^+ appearance due to the introduction of H_2O from the CBGB. A shared fit of rates 5.1 and 5.2 yields a water beam density $\rho_{beam} = (2.18 \pm 0.37) \times 10^6 \text{ cm}^{-3}$.

Using the ADO approximation

3.3 Beam Velocity

Over the various flow regimes; effusive, intermediate, and supersonic, the forward velocity and distributions change drastically from 150 m/s up to 800 m/s. We first consider the edge cases of the effusive and supersonic regimes. In the effusive regime, we make the assumption that the particles in the cell are non-interacting. We may rewrite the equation 3.2 as a function of the mean velocity \bar{v} into a simpler form .

$$f(v) = \frac{32}{\pi^2} \frac{v^2}{\bar{v}^3} e^{-4v^2/\pi\bar{v}^2} \quad (3.15)$$

To get the velocity distribution in the beam, we can calculate the distribution of particles

incident on an aperture in the cell.

$$\begin{aligned} f_{beam}(v) &= \frac{v}{\bar{v}} f(v) \\ &= \frac{32}{\pi^2} \frac{v^3}{\bar{v}^4} e^{-4v^2/\pi\bar{v}^2} \end{aligned}$$

For low Reynold's numbers ($Re < 1$) the flow at the aperture is purely molecular, which means that there are few to no collisions. This allows us to continue to use the Maxwell-Boltzmann distribution to describe the forward velocity [23].

$$\bar{v}_{\parallel} = \int_0^{\infty} v f(v) dv \approx 1.2\bar{v} \quad (3.16)$$

The spread of the forward velocity of an effusive beam is the full width half max (FWHM) of the Maxwell-Boltzmann distribution: $\Delta\bar{v} \approx 1.5\bar{v}$. As the Reynolds number increases, one can reach the supersonic regime ($Re > 100$) where the forward velocity reaches $1.4\bar{v}$ and the distribution drastically narrows.[23, 33]

But as the flow regime nears the supersonic regime, forward collisions around the aperture cause boosting of the average velocity as well as a decrease in the velocity spread.

Supersonic beam velocities can be shown to be:[33]

$$v_{\infty} = \sqrt{\frac{2k_b T_0}{m} \frac{\gamma}{\gamma - 1}}$$

Where γ is the heat capacity ratio C_p/C_v , and T_0 is the original temperature of the source.

The intermediate regime in between the effusive and supersonic regimes is particularly difficult to model, for there are some collisions at the aperture unlike the effusive regime, causing some boosting and narrowing, but not enough to treat the behavior as fully fluid-like. The section 3.2 results show that we can produce a beam in this intermediate regime by demonstrating clear hydrodynamic entrainment.

To better understand the reaction temperatures we will be able to reach, we need a characterization of the beam's velocity, more specifically, the velocity of the target species entrained within the buffer gas. The ideal target species is one with a reliable loading method and can be directly detected in small amounts. Ytterbium metal is known to have good ablation properties and the produced neutrals have well known spectra. By ablating ytterbium foil inside of the experimental cell while the neon gas is being introduced, the ytterbium is cooled by the buffer gas and carried out of the cell. As long as the target species number density is a trace amount in comparison to the bulk buffer gas number density (0.1%), the flow characteristics are dominated by the buffer gas species [22]. Based upon the results of our direct RGA measurements of the beam density, we know that the cell parameters used in the previous measurement land us in the intermediate flow regime due to the clear evidence of hydrodynamic entrainment.

To determine the velocity of the beam, we ablate an ytterbium target mounted inside the experimental cell where both neon and water are being introduced. The resulting beam is then hit with a 399 nm laser to excite the Yb isotope transitions. The laser is scanned over 3.5 GHz, encompassing all possible Yb isotope peaks. Two scans were taken, one with the 399 nm light perpendicular to the beam path, and the other where the laser is coming in with an angle of 57.3°. The resulting spectra are then fitted with summed Gaussian functions with predetermined isotopic shifts, giving us the center (^{174}Yb) frequency, as well as the widths of the lines. Between the transverse and angled scans, we find an offset in the spectrum caused by the doppler shift, seen in figure 3.12:

$$\Delta f = \frac{\Delta v}{v} f \cos(\theta) \quad (3.17)$$

Where f is the fundamental center frequency, Δf is the offset observed, v is the forward velocity of the excited ^{174}Yb , and θ is the angle of the beam with respect to the beam. Using equation 3.17, we find the forward velocity of the beam is around 150 m/s, within the expected range for a hydrodynamically entrained beam. The fitted shared widths give us a beam temperature of 20 K, which is exactly what the experimental cell was held to.

Missing
figure

Diagram of Yb beams

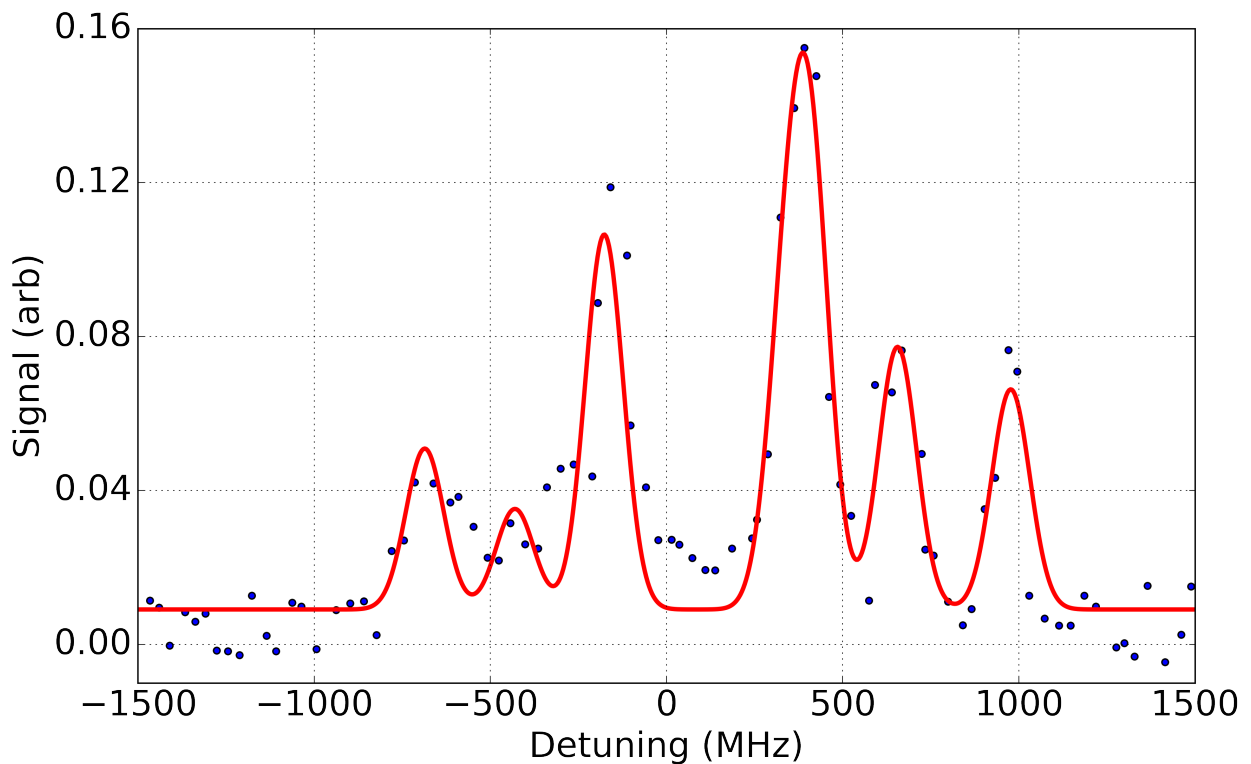


Figure 3.12: Angled longitudinal scan of Yb fluorescence collected by PMT at ≈ 24 cm from cell aperture. A fit of all isotopic peaks yields mggm

We find that the Yb is entrained within the neon and sympathetically cooled to the cell's temperature. The water that is also introduced in the beam will also be at a similar temperature and forward velocity as long as the neon density is much larger than that of the water when the beam dynamics is dominated by the properties of the buffer gas species.

3.4 Beam Shuttering

With the RGA in the beam path, we were able to open and close a shutter in the beam path and see an extinction of the water signal, but a more accurate representation would be from the ions in the trap themselves. We know that the trapped Be^+ ions will react with H_2O to predominately produce BeOH^+ , which we see as a drop in the fluorescence. Figure 3.15 shows fits of the fluorescence decay as a beam from the CBGB is suddenly blocked by our shutter in the beam line. Comparing the fitted reaction rates, we find that they agree with the background rates found as shown in figure 3.14. This indicates to us that we indeed have a beam of cryogenic water coming from the CBGB, as seen by the sudden extinction of the $\text{Be}^+ + \text{H}_2\text{O}$ reaction.

To accurately control the reactions occurring in the ion trap, it is ideal to be able to quickly turn the beam on and off. Controlling the fill lines outside of the chamber is not ideal, as thin tubing was used, yielding very low conductances. The characteristic time of flow through a tube can be shown to be $\tau_{tube} = CV$, where C is the conductance and V is the volume of the tube in question. Turning on and off the flow outside of the chamber would give time constants in the range of seconds. To more deterministically control the beam flux, we insert a vacuum compatible Uniblitz VS35 35mm Optical Shutter in the beam line. The shutter does not create a seal within the chamber, background gasses may flow around and influence the beam.

Running the beam with the shutter in between the RGA and experimental cell, we find that there is a distinct difference in the H_2O signal when the shutter is open and closed. Using laser cooled Be^+ , we find the difference in the reaction rate both independently, as well as in situ, figs. 3.14 and 3.15.

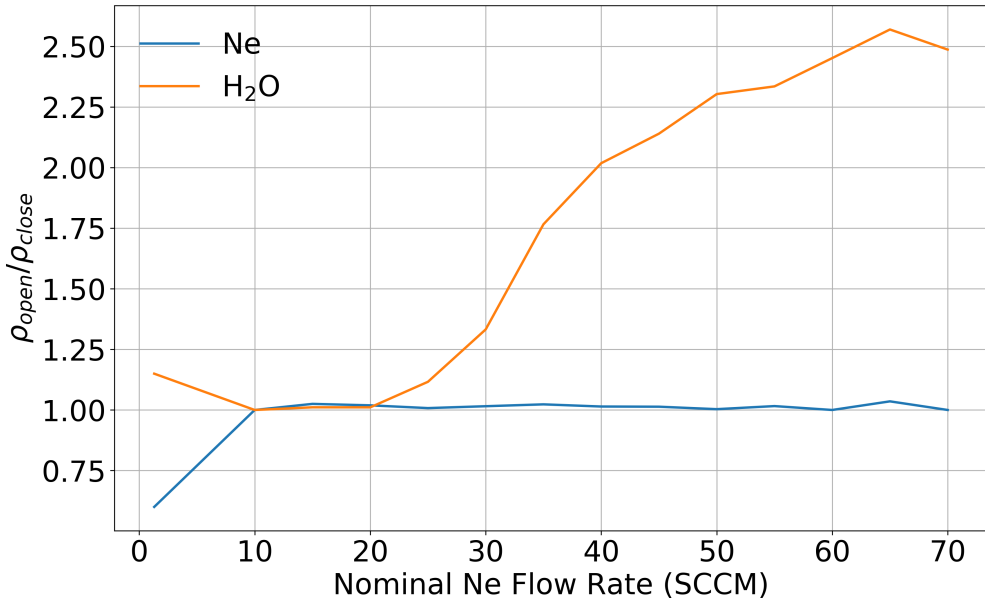


Figure 3.13: Ratios of water and neon from the beam when the Uniblitz shutter is opened and closed. Detection is done via RGA placed 30 cm from the cell aperture.

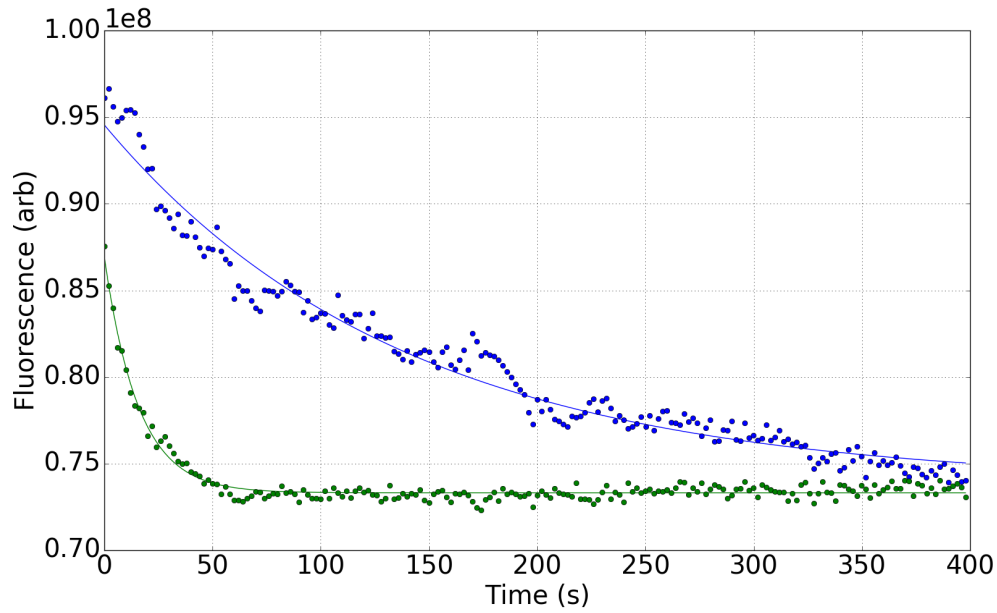


Figure 3.14: Fluorescence decays of loaded Be⁺ ions exposed to a cold water beam with an inline shutter either opened, in green ($\tau = 7.23 \times 10^{-3}$ s) or closed, in blue ($\tau = 6.37 \times 10^{-2}$ s)

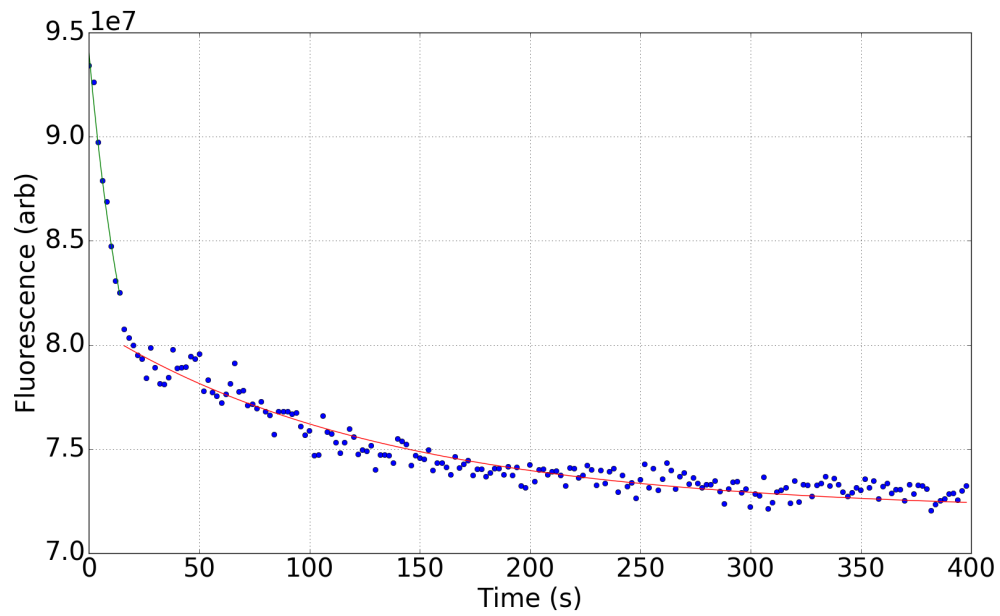


Figure 3.15: Fluorescence decays of loaded Be^+ ions exposed to a cold water beam with an inline shutter opened, in green ($\tau = 5.37 \times 10^{-2}\text{s}$) or closed, in red ($\tau = 7.59 \times 10^{-3}\text{s}$)

CHAPTER 4

Trapping and Cooling Ions

4.1 Ion Trapping

Use RF fields at 1MHz in a linear quadrupole ion trap (LQT) to trap charged particles spatially.

Consider a 3 dimensional potential that could trap a particle, we may assume the form:

$$\Phi = \frac{\Phi}{r_0^2} \sum_{i=1}^3 \alpha_i r_i^2$$

Where r_0 is the distance to the potential surfaces and $r_{1,2,3}$ correspond to x , y , and z respectively. But by Laplace's equation, $\Delta\Phi = 0$, we don't get a confining potential as one of the terms α_i must be negative, leading to a saddle-like potential. To get around this, we may vary the potential in time to create a pseudo-potential that can confine a subset of ions:

$$\Phi_0(t) = V_{DC} + V_{rf} \cos(\Omega_{rf}t)$$

Solving for the equations of motion, we find:

$$\ddot{r}_i + \frac{2\alpha_i e}{mr_0^2} (V_{DC} + V_{AC} \cos(\Omega_{rf}t)) r_0 = 0 \quad (4.1)$$

To solve this, we make changes of variable:

cite
the
OG
Paul

$$a = \frac{8eV_{DC}}{mr_0^2\Omega_{rf}^2} \quad (4.2)$$

$$q = \frac{4eV_{DC}}{mr_0^2\Omega_{rf}^2} \quad (4.3)$$

$$\tau = \frac{1}{2}\Omega_{rf}t$$

To then find the characteristic Mathieu equation:

$$\frac{\partial^2 u}{\partial \tau^2} + (a - 2q \cos(2\tau))u = 0 \quad (4.4)$$

A diagram showing stable solutions to equation 4.4 with the experimental trap values is shown in figure 4.2. To provide full 3 dimensional trapping, DC end cap voltages of around 200 V are applied to contain the ions axially.

Considering our linear quadrupole trap, where we have radial symmetry, the conditions for the x and y orientations are the same, where $a_x = a_y = -\frac{1}{2}a_z$ as well as $q_x = q_y = -\frac{1}{2}q_z$. As long as we are in a regime where $a \ll q^2 \ll 1$, we can approximate the pseudo-potential as a harmonic oscillator where multiples of the secular frequency are the allowed modes.

$$\omega_i = \gamma_i \frac{\Omega_{rf}}{2} \quad (4.5)$$

Where $\gamma_i = \sqrt{a_i + \frac{q_i^2}{2}}$. Inside this harmonic potential, the ions may move around up until the point at which they would hit the trap rods. Keeping with the harmonic potential approximation, we can characterize the maximum energy an ion may have in the trap to be when the energy of the ion at the condition where it would be displaced far enough to hit a rod.

$$E_0 = \frac{m}{2e}\omega_{sec}^2 r_0^2 \quad (4.6)$$

Compiling the relevant trap parameters and using equations eqs. (4.5) and (4.6):

Parameter	Value
r_0	6.85 mm
Ω_{rf}	$(2\pi)3$ MHz
V_{DC}	2 V
V_{rf}	250 V
ω_{sec}	83 kHz
$E_0(m/z = 9)$	3 eV

Table 4.1: Experimental trap parameters predominantly used in this thesis.

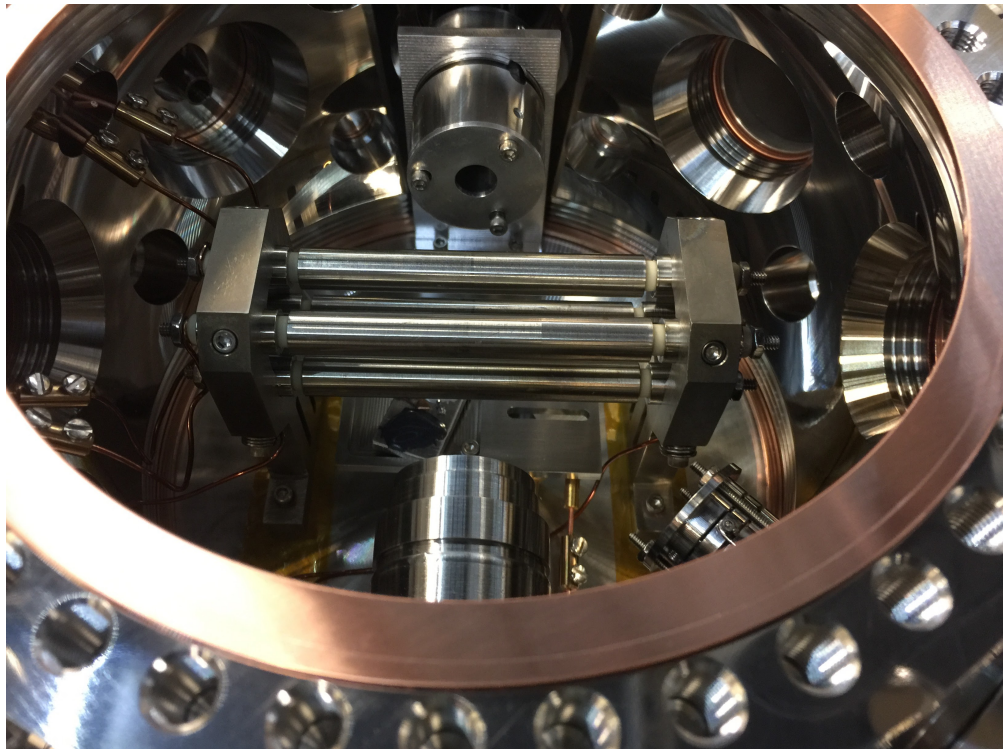


Figure 4.1: The ion trap inside of the experimental vacuum chamber. An Einzel lens and imaging objective are seen on the vertical axis.

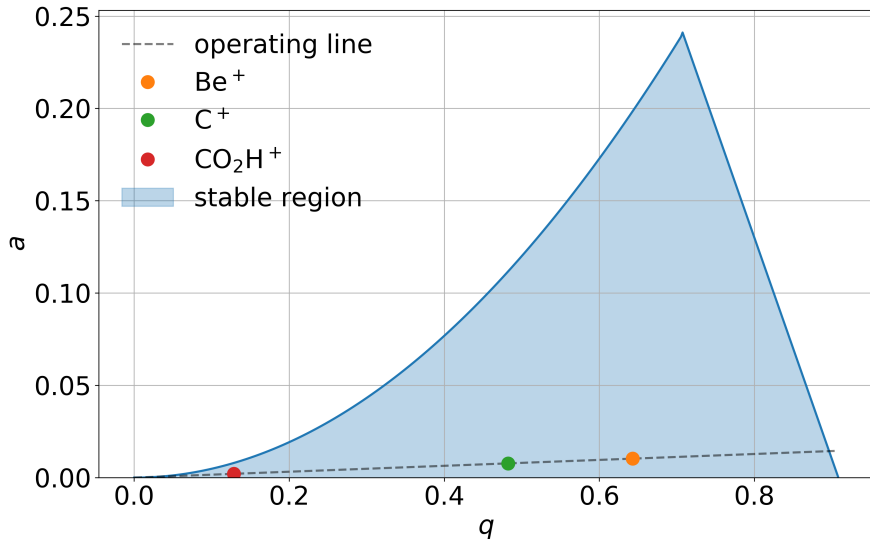
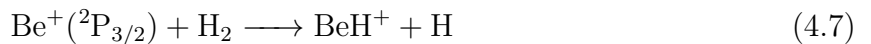


Figure 4.2: Stability diagram of the experimental ion trap with parameters defined in table 4.1. The trap is set up to be stable for ions of interest, including high mass reaction products, from Be^+ , and C^+ at $m/z = 9$, 12 to CO_2H^+ at $m/z = 45$.

4.2 Vacuum Requirements

To reliably laser cool and trap ions into crystals, it is ideal to have ultra-high vacuum (UHV) which is generally defined as having a pressure $< 10^{-9}$ Torr. The characteristic collision rate between a monopole and polarizable neutral is defined by the C_4/r^4 attractive term and is called the Langevin collision rate. In a vacuum chamber, we tend to find the predominant gas left after baking is H_2 , which will have collisions with the trapped ions at the Langevin rate.

By knowing the rate of



to be [36]. With an ion gauge, we find our vacuum to be $\approx 1 \times 10^{-10}$ Torr, and verified [rate]

via Be^+ fluorescence decay due to reactions with background H_2 .

We want to make sure that there is as little H_2O in the chamber as possible to ensure that the data we take with the water from the CBGB is exclusively from the CBGB and not due to background water collisions.

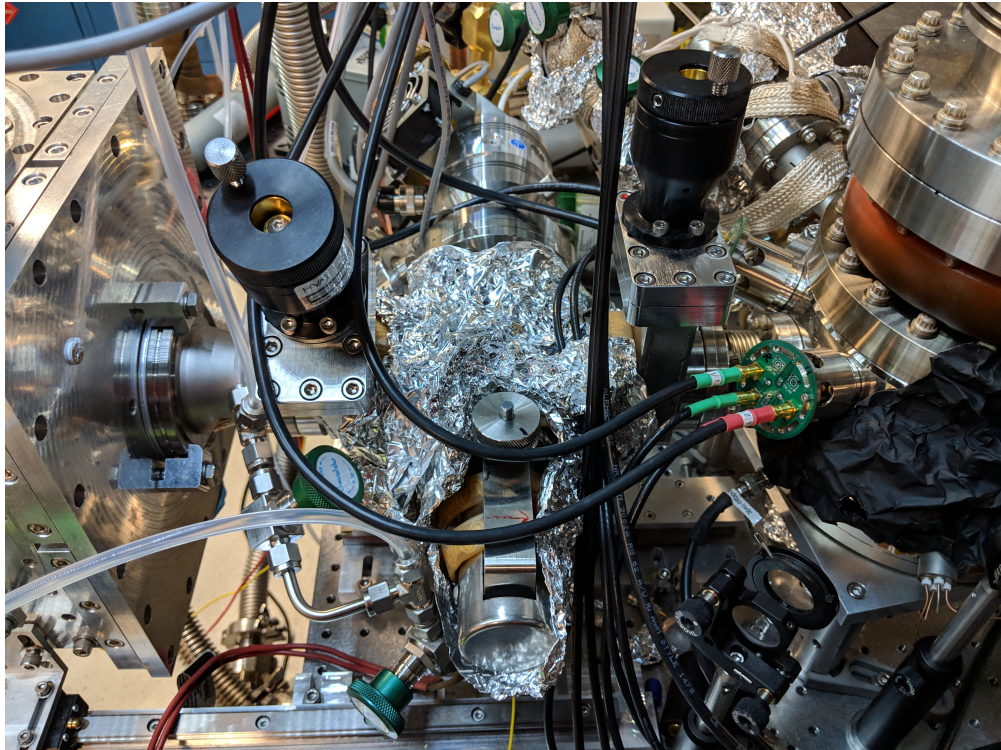


Figure 4.3: Differential pumping region in between the stem and ion trap chambers with gate valves on either end. Blank copper CF gaskets with apertures of 4 mm and 10 mm are placed towards the stem and ion chamber respectively to limit conductance of background gasses while allowing the cryogenic beam through. An Agilent Twistorr 84 FS turbo pump keeps the region at pressures around 10^{-10} Torr and a leak valve allows for controlled introduction of secondary gasses.

4.3 ${}^9\text{Be}^+$ Laser Cooling

Laser cooling for the ${}^9\text{Be}^+$ ion is done with a Toptica TA-FHG Pro tuned to 313 nm with a peak power of 400 mW. The fundamental laser light is blue-detuned by 400 MHz from the

$^2S_{1/2}$ to $^2P_{3/2}$ transition. The fundamental is then passed through a 400 MHz AOM to be on resonance with the transition. The unperturbed light is then double passed through another 400 MHz AOM to repump the population that has fallen into the $2S_{1/2}$ state.

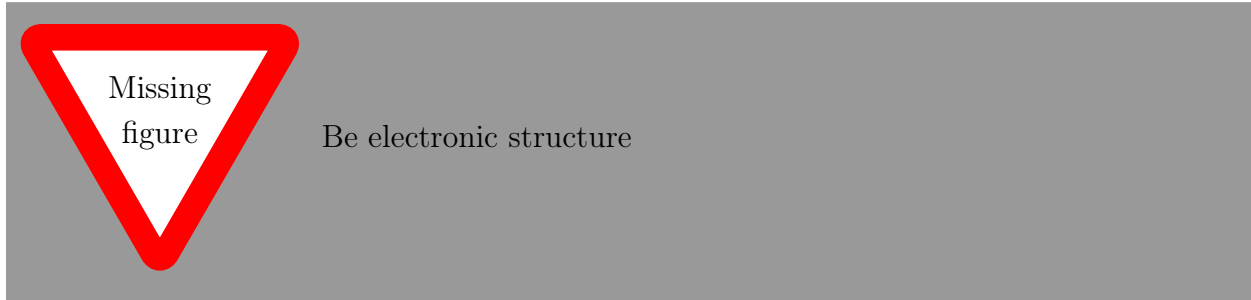


Figure 4.4: Electronic structure of ${}^9\text{Be}^+$, laser cooling is done with 313 nm light.



Figure 4.5: AOM's running at 400 MHz are used to tune the initially blue detuned primary beam on resonance with the $^2S_{1/2}$ to $^2P_{3/2}$ transition. A double passed AOM tunes the primary beam to the $^2S_{3/2}$ to $^2P_{3/2}$ transition to re-pump any $^2P_{3/2} \rightarrow ^2S_{3/2}$ decays. A third AOM creates a first order beam 200 MHz red to aid the capture of hot ablated Be^+ ions.

As we excite the cooling transition, force is being imparted onto the ion via absorption of the photons and spontaneous emission. We can define the force to be the product of the scattering rate of a two level system and the momentum of each photon.

$$\begin{aligned}
F &= p\Gamma\rho_{pp} \\
&= \hbar k \Gamma \frac{1}{2} \frac{s}{1 + s + 4 \left(\frac{\delta - \vec{k} \cdot \vec{v}}{\Gamma} \right)^2}
\end{aligned} \tag{4.8}$$

Where k is the photon's wavenumber, Γ is the linewidth of the excited transition, and ρ_{pp} is the probability of finding the ion in the excited ${}^2\text{P}_{3/2}$ state characterized by the saturation parameter $s = I/I_s = I/(\frac{\pi hc}{3\lambda^3\tau})$ and laser detuning $\delta = \omega_0 - \omega_l$. We can see that the force the ion feels is dependent on the laser detuning from resonance, which in turn is dependent on the doppler shift of the ion with respect to the laser $\vec{k} \cdot \vec{v}$. In general, the laser frequency (ω_l) is red detuned from the cooling transition ($\omega_l < \omega_0$). In this instance, if the ion is moving towards the laser such that the velocity (v) and k vector are anti-aligned, we see a positive doppler shift in the frequency ($+kv$), decreasing the effective detuning, increasing the scattering rate. When the ion is moving away from the laser while $\omega_l < \omega_0$ is true, we see that the detuning increases, lowering the scattering rate. Each time the ion absorbs a photon, it gains a momentum kick in the photon's direction, meaning the ion preferentially absorbs light that causes it to lose momentum. After absorption, the ion emits a photon after $\tau = \Gamma^{-1}$ time, isotropically, which averages to zero. We can Taylor expand equation 4.8 for small values of v to find this velocity dependence.

$$F(v) = F(v = 0) + \beta v$$

Where we define the damping coefficient:

$$\beta = 4\hbar k^2 \frac{s \frac{\delta}{\Gamma}}{1 + s + 4 \left(\frac{\delta}{\Gamma} \right)^2}$$

Since the ion trap is not a perfect harmonic potential, which would require hyperbolic trap electrodes, the ion's trajectory is mixed along each axis, allowing for the 3 dimensional laser cooling with just one beam angled from both radial and axial axes of the trap.

4.4 Imaging System

Using the 313 nm laser, we fluoresce the Be^+ ions and cool them down to a cloud or crystal in the ion trap. The scattered light is observed via our imaging system shown in figure 4.6. The components include the Andor iXon3 camera with EM gain, a 313 nm band pass filter, angled mirror, enclosing lens tubes, and Sill objective lens with 0.2 NA, and 40 mm working distance. The alignment of our objective lens to camera imaging plane yields a magnification of about $\times 5.5$.

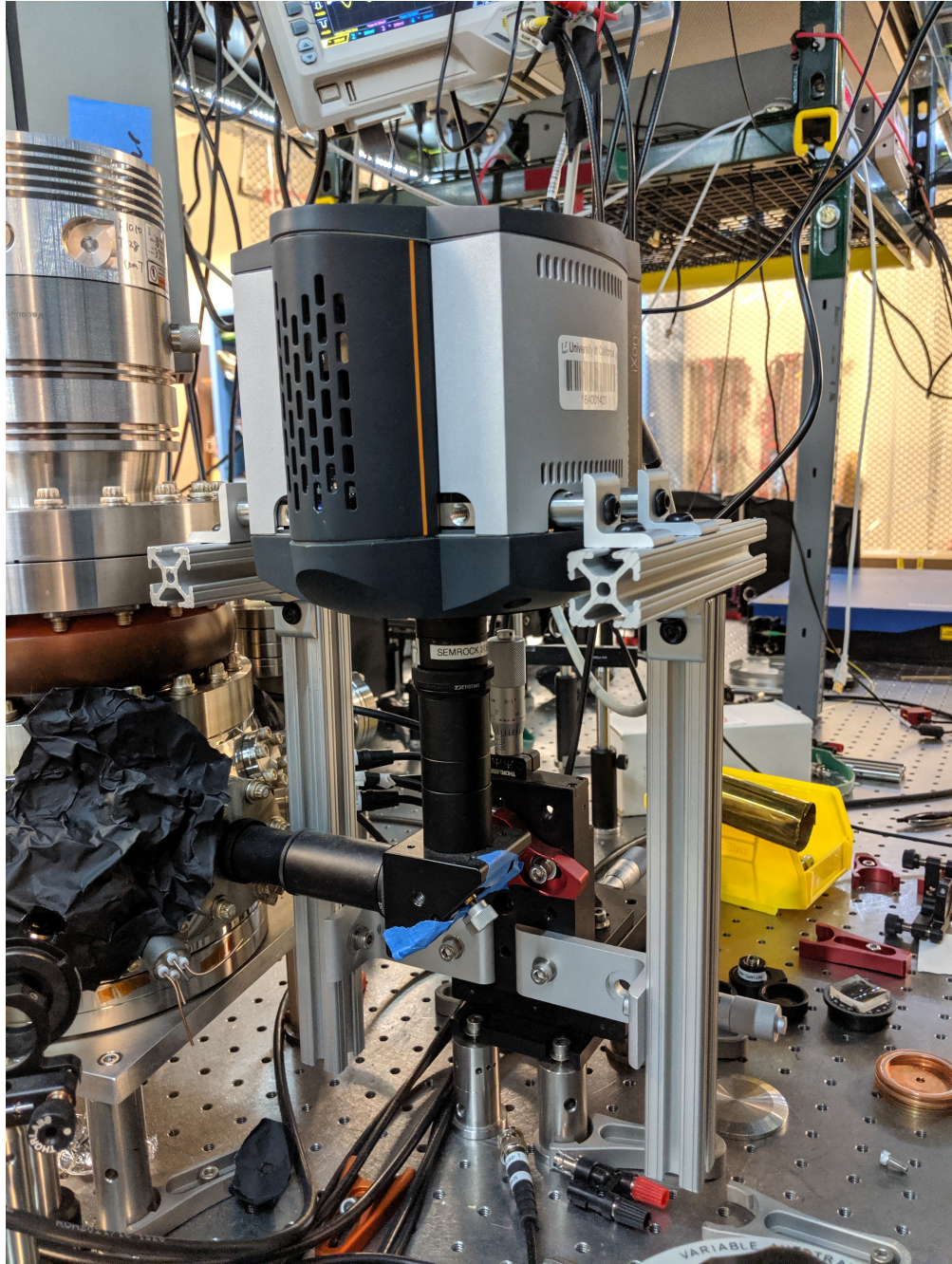
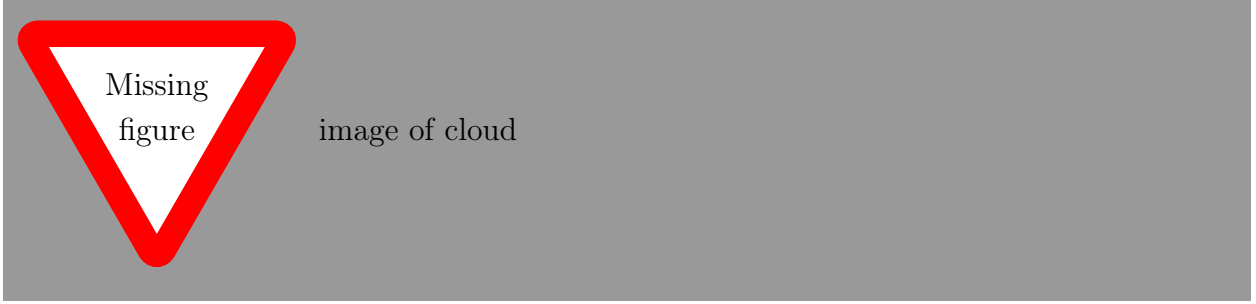


Figure 4.6: The iXon3 camera is mounted onto a 3 axis translation stage as well as the enclosed imaging pathway. The imaging tubes include the Sill objective lens at the end, inserted into the reentrant flange, an angled mirror, and a 313 nm bandpass filter placed at the camera input.

All of the imaging components are rigidly mounted onto the 3 axis translation stage

allowing us to move the focal point without changing the magnification.



Considering all the components, the total efficiency of our imaging system is:

$$\epsilon = \Omega\alpha\beta\gamma \quad (4.9)$$

Where Ω is the solid angle the reentrant objective appends, α is the camera's quantum efficiency at 313 nm, β is the camera's exposure time, and γ is the camera's gain. For a fluorescing ion scattering at $\Gamma \times (\rho_{pp} \approx 0.20)$, we expect on the order of 10^5 counts per ion including the imaging inefficiencies.

4.5 Determining Excited state

Ideally, having a single ion in the trap while sweeping the frequency or power would allow us to determine the saturation parameter, and thus the fraction of Be^+ in the excited ${}^2\text{P}_{3/2}$ state. Due to the size and depth of our ion trap, we cannot reliably load only one ion. On top of that, the most common residual gasses in a vacuum chamber, H_2O and H_2 both readily react with Be^+ in the excited state. Instead, we take images of the ions at various powers and find the fluorescence per ion to fit to a generalized form of the scatter rate (Γ_d):

$$\begin{aligned} \Gamma_d &= a\rho_{pp} \\ &= \frac{a}{2} \frac{s}{1 + s + 4(\delta/\Gamma)^2} \end{aligned} \quad (4.10)$$

Where the parameter a consists of all the efficiency parameters in equation 4.9. To get the P-state fraction, Be^+ ions are loaded into the trap and A-ramps are applied until a chain is formed and the laser detuning adjusted until we see maximum fluorescence on the camera, which coincides with a detuning of $\Gamma/2$. Then images of the ions are taken at various laser powers and run through a maximum filter algorithm to identify the locations of individual ions as seen in figure 4.7. The portion of the image not an ion is then averaged to obtain the background pixel value, which is then subtracted from each localized ion image. The pixel values over each localized ion is then summed to yield a total fluorescence value, which is then averaged for each image as shown in figure 4.8. By fitting the collected fluorescence per ion as a function of incident power, we find the generalized efficiency a , revealing the P-state fraction at each power in ρ_{pp} , shown in figure 4.9.

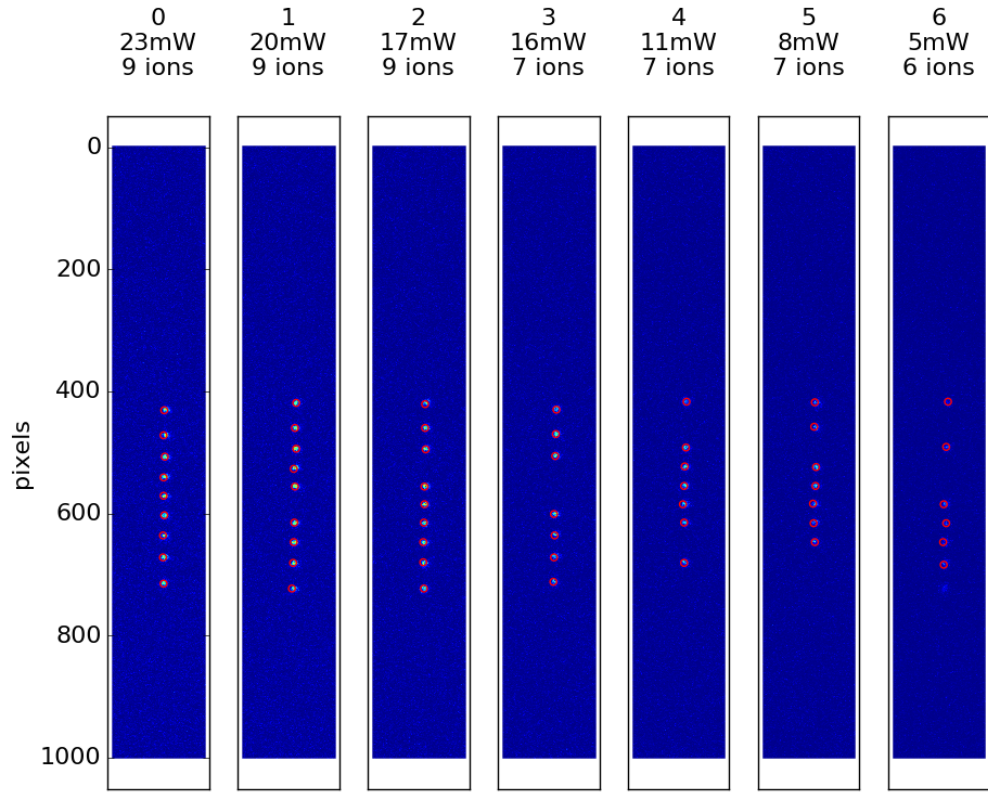


Figure 4.7: A set of ion images taken at various 313 nm powers run thorough a maximum filter algorithm that identifies local maxima, representing individual ions (circled in red).

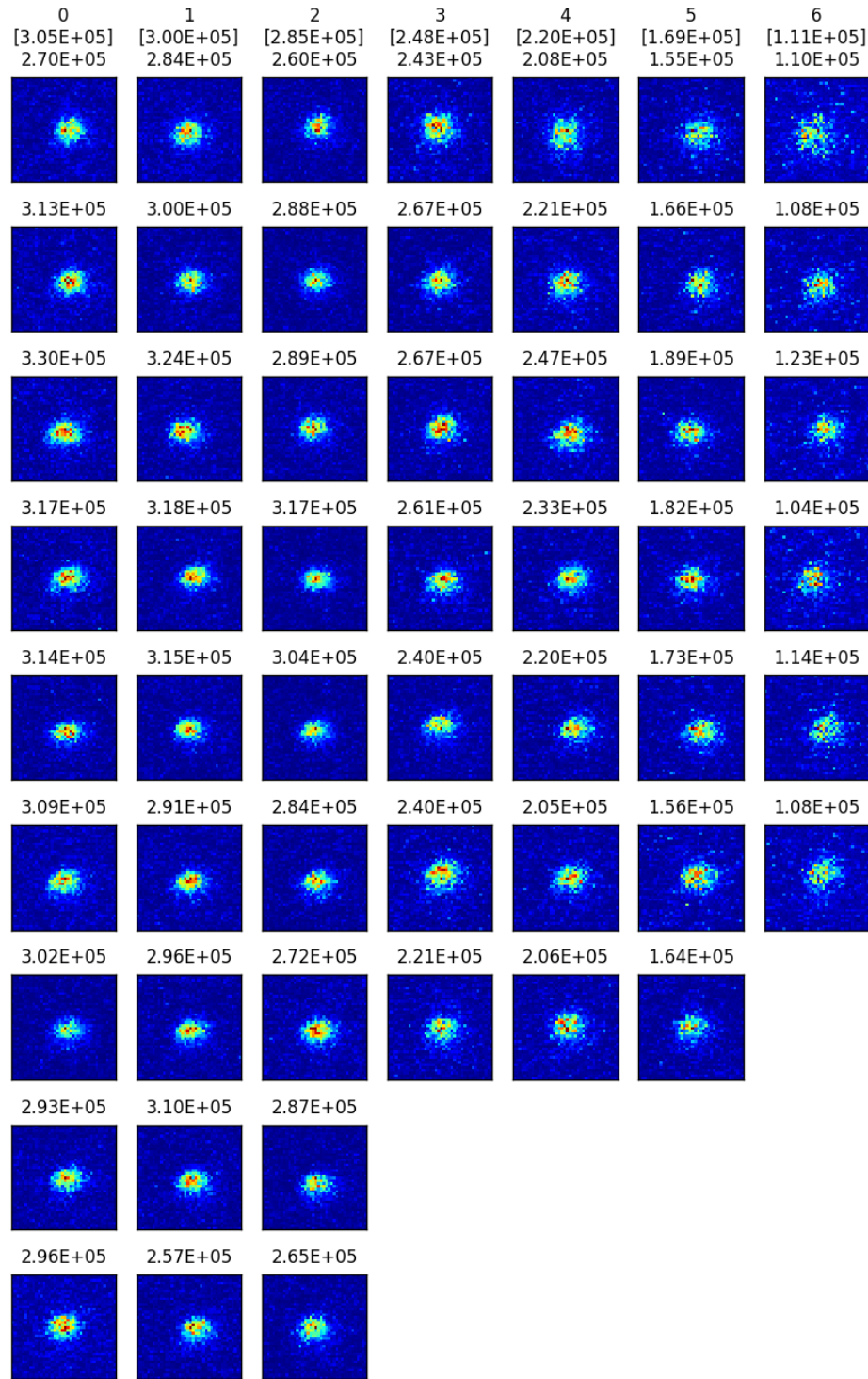


Figure 4.8: Individual ions identified from images in figure 4.7. Integrated pixel values with subtracted background counts shown for each image, a set's averaged value is shown in brackets.

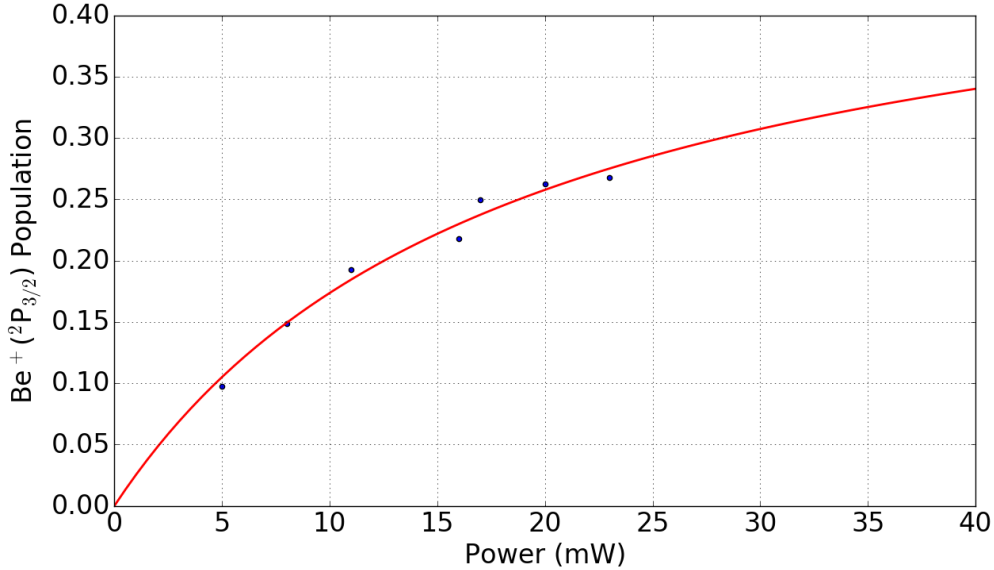


Figure 4.9: P-state fraction curve fitted to incident laser power at a fixed detuning of $\delta = \Gamma/2$. Total fluorescence value is normalized by fitted efficiency parameter a to yield ρ_{pp} .

4.6 Time of Flight Mass Spectrometer (TOF-MS)

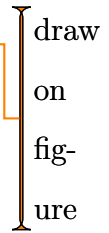
pew pew shoot the ions into a tube and measure their mass

4.7 Dual Species Loading

Although loading and cooling Be⁺ ions is fairly straight forward, it is not as clear as how to load C⁺ ions into the trap with Be⁺ reliably. Early attempts involved using the home-made electron gun to electron dissociate and CO gas introduced via leak valve, all possible ionized products of CO were detected (C⁺, O⁺, and CO⁺). Even when loading into an empty trap, it was not possible to reliably isolate the C⁺ via A-ramping of the trap RF voltage. Prolonged use of the electron gun directly towards the ion trap also caused charging that would slowly dissipate and change the trap parameters. On top of these complications, it would have to work in conjunction with ablation loading Be⁺.

Instead of using two different methods to load the different ion species, ablating both

simultaneously was found to be the best method. A sample of Be metal was placed on top of a piece of graphite on the target holder so that both samples were in view of the ablation laser. The set up shown in figure 4.10 allowed us to separate the ablation laser into two beam with independent alignment and focal planes. The polarization of the laser light is rotated with a half-waveplate, which then enters a polarizing beam splitter (PBS), allowing for tuning of power into either path. The vertically polarized reflected light is reflected again with another PBS and is steered up to the objective lens and then focused into the chamber. The horizontally polarized light transmitted through the first PBS is aligned through an adjustable telescope system. This light is then realigned with the vertically polarized light on the second PBS, co-propagating into the chamber. The "delay stage" for the horizontal light allows for independent focusing and alignment onto the sample.



draw
on
fig-
ure

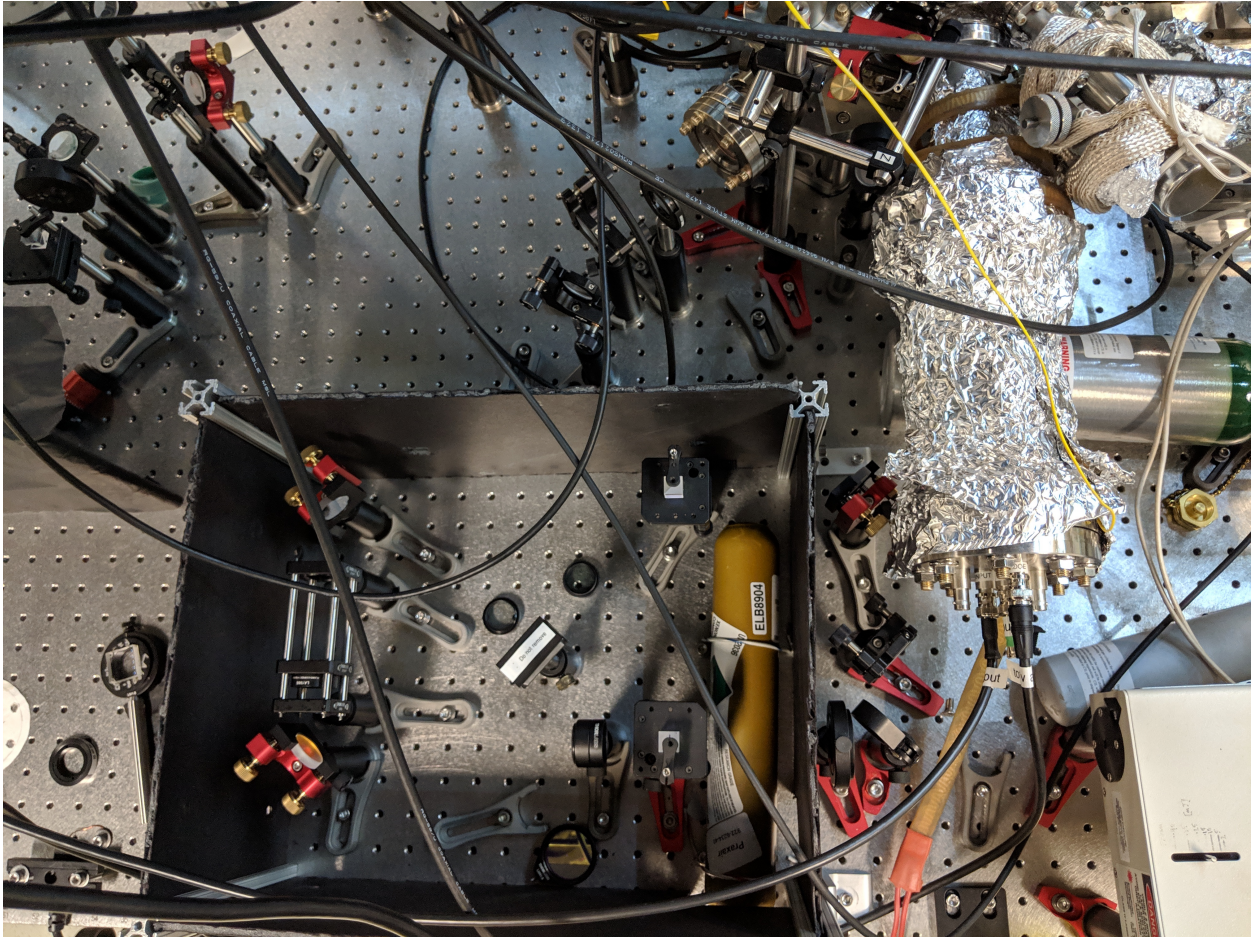


Figure 4.10: Image of the single laser, dual ablation set up. The 1064 nm YAG pulse is split into two paths, and recombined such that they proceed through the same focusing element into the chamber to hit two different targets.

Blocking one beam allowed for adjustments for the ablation of each species independently. When loading C^+ , we found a strong dependence of the trapped species and the fluence. Lower fluence created not only C^+ , but clusters of, C_2^+ , and C_3^+ as well. Tight focusing of the beam improves the efficiency of creating only C^+ , but some Cn^+ is still usually produced. By changing the trap's a parameter (A-ramp) via changing the V_{DC} (4.2), we can change the stability diagram for the trap, causing higher m/z ions to become more unstable. The higher mass Cn^+ ions are preferentially kicked out of the trap, while the lighter Be^+ and C^+

are less affected, allowing us to load clean samples of the desired species.

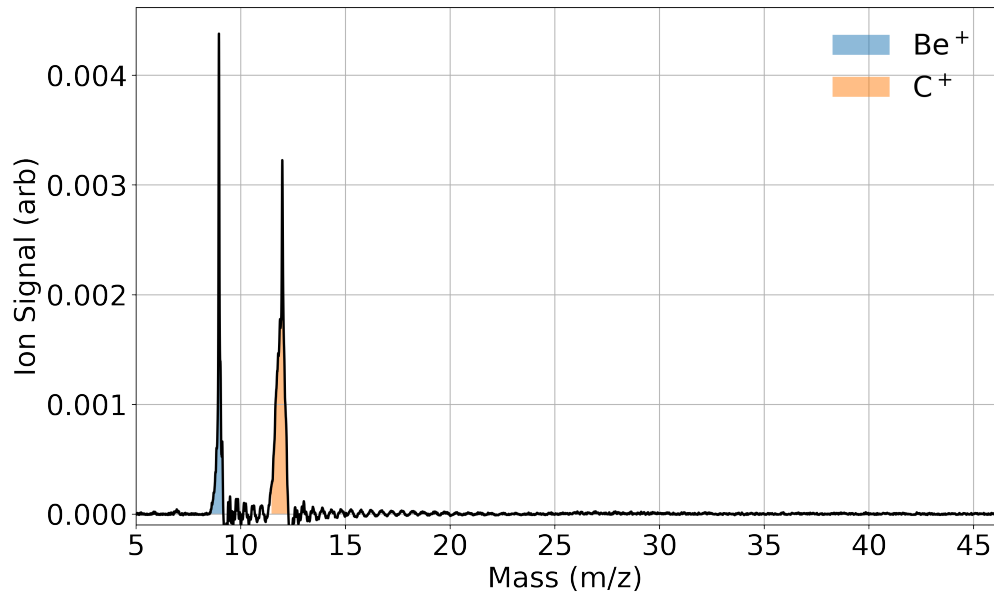


Figure 4.11: TOF trace of simultaneous Be^+ and C^+ ablation loading averaged over 10 shots. A soft A-ramp is applied after loading, ejecting any unintentionally loaded C_n^+ clusters. The C^+ peak is narrowed from sympathetic cooling with the laser cooled Be^+ ions.

CHAPTER 5



5.1 Optical Control of Reactions between Water and Laser-Cooled Be^+ Ions

5.1.1 Abstract

We investigate reactions between laser-cooled Be^+ ions and room-temperature water molecules using an integrated ion trap and high-resolution time-of-flight mass spectrometer. This system allows simultaneous measurement of individual reaction rates that are resolved by reaction product. The rate coefficient of the $\text{Be}^+({}^2\text{S}_{1/2}) + \text{H}_2\text{O} \longrightarrow \text{BeOH}^+ + \text{H}$ reaction is measured for the first time and is found to be approximately two times smaller than predicted by an ion-dipole capture model. Zero-point-corrected quasi-classical trajectory calculations on a highly accurate potential energy surface for the ground electronic state reveal that the reaction is capture-dominated, but a submerged barrier in the product channel lowers the reactivity. Furthermore, laser excitation of the ions from the ${}^2\text{S}_{1/2}$ ground state to the ${}^2\text{P}_{3/2}$ state opens new reaction channels, and we report the rate and branching ratio of the $\text{Be}^+({}^2\text{P}_{3/2}) + \text{H}_2\text{O} \longrightarrow \text{BeOH} + \text{H}$ and $\text{H}_2\text{O} + \text{Be}$ reactions. The excited-state reactions are nonadiabatic in nature.

5.1.1.1 Introduction

Low-temperature reactions of simple ions with small molecules play a central role in astrochemical environments from interstellar clouds to cometary comae to planetary atmospheres, including that of Earth[2, 24]. The chemical evolution of interstellar molecular

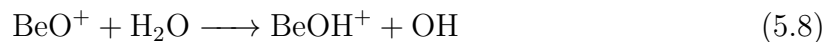
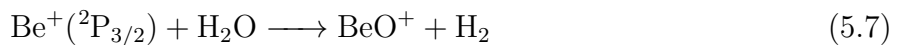
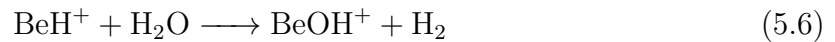
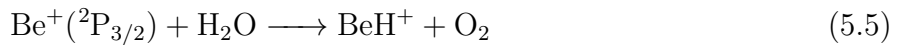
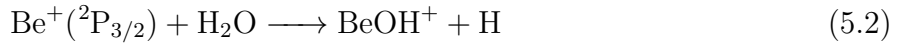
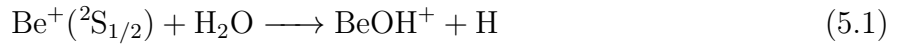
clouds ultimately yields the seedbed from which new stars and planets are born and the raw materials from which life likely developed. A firm understanding of the reaction rates for a host of elementary ion-molecule reactions is essential to accurately model these environments these environments. Techniques such as selected ion flow tubes (SIFTs)[1], guided ion beams[3], and supersonic flows (CRESU)[40] have improved our empirical understanding of these processes; however, each has its own limitations.[43, 44] Theoretically, it has long been recognized that these ion-molecule reactions are often barrierless, and their rates are frequently described by capture models.[16] However, recent studies have revealed that dynamical features can sometimes prevail,[29, 26, 6] in which case statistical treatments may not be accurate.[18, 9] Therefore, new experimental and theoretical efforts are needed to accurately address ion-molecule chemistry.

We have developed an approach, adapted from the ultracold ion community,[20, 50, 53] to study reactions of atomic ions with small molecules. Here we report the use of this approach to study the reaction of Be^+ with gas-phase water for the first time. There have been very few experimental studies of gas-phase reactions between metal ions and water, especially at low temperature, despite their importance for metal ion chemistry in a range of environments.[19, 32, 52]

Singly ionized beryllium is a particularly attractive metallic reactant to use for such studies because it is both theoretically tractable and experimentally highly controllable. The relatively simple electronic structure of this three-electron ion allows both highly accurate characterization of its electronic structure and laser cooling,[4] and the low mass of Be^+ lends itself to high motional frequencies as well as efficient sympathetic cooling of other chemically interesting atomic ions when employed in ion traps.[7, 36, 25, 39] For the molecular reaction partner, H_2O is arguably the most important molecule in chemistry, and theoretical studies of its reactions with a single atom have been reported on full-dimensional potential energy surfaces (PESs).[27, 45, 35, 28, 56] Thus this system of reagents provides an opportunity to perform a high-resolution comparison between experiments and theory for a molecule-ion system.

The apparatus employed here is shown in the Supporting Information (SI) (Figure S1). Laser ablation of metallic Be is used to produce Be^+ ions, which are trapped in a linear radio frequency Paul trap.[55] Laser cooling [54] is used to cool the translational motion of the ions, resulting in a Coulomb crystal of Be^+ ions. Gaseous, room-temperature H_2O molecules are then introduced via a leak valve into the trapping region, where they react with the trapped ions. Charged products of the chemical reaction remain in the trap and are subsequently detected via an integrated time-of-flight mass spectrometer (TOFMS) recently developed by our group[38, 37] and used to discover new species.[34] The total reaction rate is measured by monitoring the decay of Be^+ ion fluorescence, and the product branching ratios are extracted from the mass spectrum.

A key feature of this experiment is that by varying the detuning of the 313 nm laser used to cool the ions, the population in the excited $1\text{s}^2 2\text{p}^1 {}^2\text{P}_{3/2}$ and ground $1\text{s}^2 2\text{s}^1 {}^2\text{S}_{1/2}$ states can be controlled. Because the energy difference between the ground and excited states is 3.96 eV, several more product channels are open for the $\text{Be}^+({}^2\text{P}_{3/2}) + \text{H}_2\text{O}$ entrance channel. Using this system, we are able to measure the reaction rate and product branching ratio for these two entrance channels. We find that the ground-state channel, $\text{Be}^+({}^2\text{P}_{3/2}) + \text{H}_2\text{O}$, exclusively produces $\text{BeOH}^+ + \text{H}$, whereas the excited-state channel, $\text{Be}^+({}^2\text{P}_{3/2}) + \text{H}_2\text{O}$, also produces $\text{H}_2\text{O}^+ + \text{Be}$ with a yield of 10%. Specifically, the reactions considered here are



Because the translational energy of the laser-cooled Be^+ ions is < 0.5 K, the energy of the room-temperature water sets the reaction kinetic energy of $\text{Be}^+ + \text{H}_2\text{O}$ in the center of mass frame to 100K. The internal state distribution of the H_2O is assumed to be given by the 300 K. Typical TOF traces (10 sample average) at reaction times $t = 0$ and 70 s with 7 and 26% relative $\text{Be}^+(\text{P}_{3/2})$ state excitation are shown in Figure 1A,B, respectively. The fluorescence signal, which is used to determine the reaction time zero and normalize the initial ion number for the TOF, is monitored by the camera (ANDOR iXON3 EMCCD) in real time. At $t = 0$ s, a large peak of $m/z = 9(\text{Be}^+)$ and a smaller one of $m/z = 9(\text{BeOH}^+)$ are evidenced in the TOF trace (blue line), which indicates that Be^+ ions are the main species in the trap at $t = 0$. The finite amount of BeOH^+ at $t = 0$ reflects the fact that reactions eqs. (5.1) to (5.8) happen even during the loading process and that the mass filtering procedure is imperfect. At $t = 70$ s, a $m/z = 19$ peak emerges when more Be^+ ions are excited to $\text{P}_{3/2}$ state, which we identify as H_3O^+ resulting from reactions eqs. (5.3) and (5.4). The $\text{BeOH}^+ / \text{H}_3\text{O}^+$ ratio, $\eta(P_{\text{P}})$, is measured by integrating both peaks for the experimentally controlled excited-state population P_{P} . The BeOH^+ signal includes the amount unfiltered during loading, products from both reactions eqs. (5.1) and (5.2), as well as, in principle, the two-step reactions eqs. (5.5) to (5.8). The H_3O^+ signal is produced via the two-step reactions eqs. (5.3) and (5.4). Whereas we do not observe products from reactions eqs. (5.5) to (5.8) (see also in SI), they are thermochemically allowed and therefore included in our analysis, which sets upper limits on their reaction rate coefficients.

The total reaction rate is given by $\Gamma_t = \rho_{\text{H}_2\text{O}} k_t$, where $\rho_{\text{H}_2\text{O}}$ is the H_2O density measured from a Stanford Research Systems residual gas analyzer (RGA) calibrated to an ion gauge (see the SI for more information) and k_t is approximated as $k_t = P_{\text{S}}k_1 + P_{\text{P}}k_2 + P_{\text{P}}k_3$, where P_{S} and P_{P} are the Be^+ population in the $\text{S}_{1/2}$ and $\text{P}_{3/2}$ states, respectively, and k_i is the reaction rate coefficient of reaction i . Reaction eq. (5.4) has been studied by other groups, reporting a rate coefficient of $(2.05 \pm 0.010) \times 10^{-9} \text{ cm}^3/\text{s}$.^[21] The measured $\text{H}_3\text{O}^+ / \text{BeOH}^+$

ratio is given from the reaction rates by

$$\eta(P_{\text{P}}) = \frac{P_{\text{P}}k_3}{P_{\text{S}}k_1 + P_{\text{P}}k_2} \quad (5.9)$$

To use equation 5.9 to extract the individual rate coefficients (k_i), the total reaction rate Γ_t is first measured by monitoring the Be^+ fluorescence decay with a camera, as shown in Figure (see also the SI). Fluorescence decay is monitored directly after a DC voltage applied to trap electrodes is used to filter out the heavier products from the trap to allow better crystallization of the Be^+ ions by reducing ion-ion heating.[8] The inset of Figure shows typical fluorescence images of the Be^+ coulomb crystal at various times. Fluorescence is used to measure the total reaction rate because the total measurement time is 30 times shorter than using the TOFMS (Figure). To determine the separate rate coefficients for the Be^+ ground and excited states, we measure the total reaction rate coefficients for different excited-state fractions, shown in Figure . A linear fit (blue line) is found using the least-squares method. The vertical intercept of this fit gives the Be^+ ground-state reaction rate coefficient $k_1 = (2.2 \pm 0.3_{\text{stat}}) \times 10^{-9} \text{ cm}^3/\text{s}$, whereas the sum of the slope and intercept gives the total excited-state Be^+ reaction rate coefficients $k_2 + k_3 = (4.7 \pm 1.7_{\text{stat}}) \times 10^{-9} \text{ cm}^{-3}/\text{s}$. Using equation 5.9, the reaction rate coefficients of reactions eqs. (5.2) and (5.3) are then calculated to be $k_2 = (4.2 \pm 1.6_{\text{stat}}) \times 10^{-9} \text{ cm}^{-3}/\text{s}$ and $k_3 = (0.47 \pm 0.11_{\text{stat}}) \times 10^{-9} \text{ cm}^{-3}/\text{s}$, respectively. The ratio of reaction rate coefficients for reactions eq. (5.3) to eq. (5.2) is therefore $k_3/k_2 = 0.11 \pm 0.03$ independent of systematic errors in the density measurement. Charged products from reactions eqs. (5.5) and (5.7) to be $< 5 \times 10^{-10} \text{ cm}^3/\text{s}$. Reactions at these upper bounds for the rate coefficients do not significantly change the analysis above, justifying their exclusion from k_i .

It is instructive to compare these measured rate coefficients to those predicted by capture theory. For an ion reacting with a polar molecule, the leading order interaction potential as a function of the molecule-ion separation r is described by monopole-dipole interaction ($U \propto r^{-2}$) and the polarization of the molecule by the ion ($U \propto r^{-4}$). For this case, the rate coefficient is typically found using the average dipole orientation (ADO) collision model,[47]

where the ion-dipole interaction is averaged over rotational states. The expression for the rate coefficient from ADO theory is

$$k_{\text{ADO}} = 2\pi e \sqrt{\frac{\alpha}{\mu}} + 2\pi e \mu_D C \sqrt{\frac{2}{\mu \pi k_B T}} \quad (5.10)$$

where α is the average neutral molecule polarizability, μ is the reduced mass, μ_D is the molecular dipole moment, e is the elementary charge, and C is the dipole locking constant. As a capture theory, ADO theory assumes that the reaction is dominated by long-range intermolecular forces, and when the ion moves inside the maximum of the centrifugal barrier, the reaction always proceeds with unit efficiency. The ADO model predicts that both the ground and excited Be⁺ states react with a rate coefficient of $4.1 \times 10^{-9} \text{ cm}^3/\text{s}$ at 100 K reaction temperature, roughly two times larger than measured for the ground state, but in agreement with the measured reaction rate of the excited state. However, because it is long-range, the ADO model cannot provide the branching ratio and state-dependent information and is therefore insufficient for describing the observed reactions.

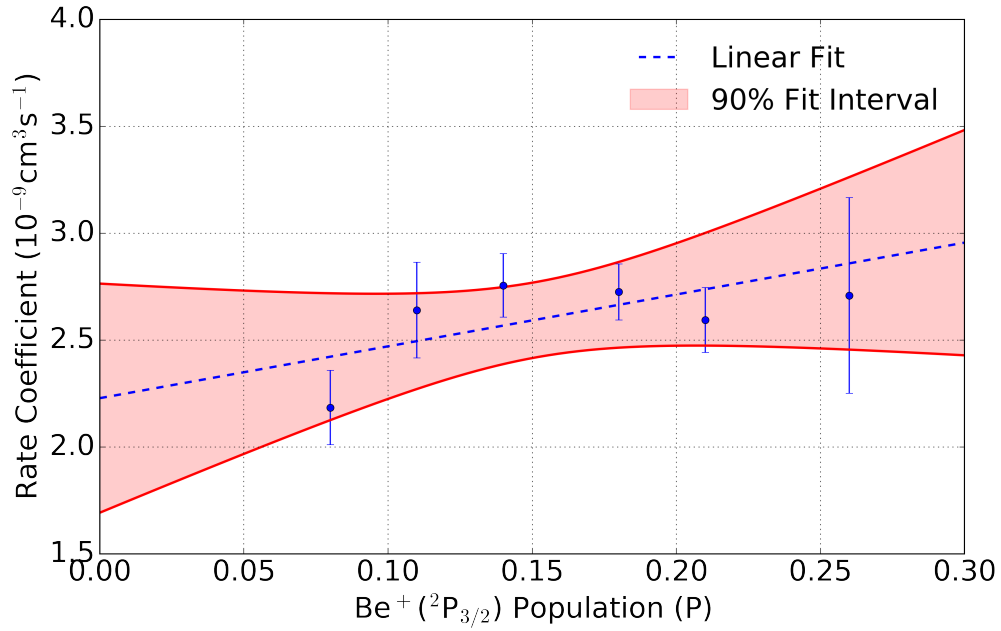


Figure 5.1:

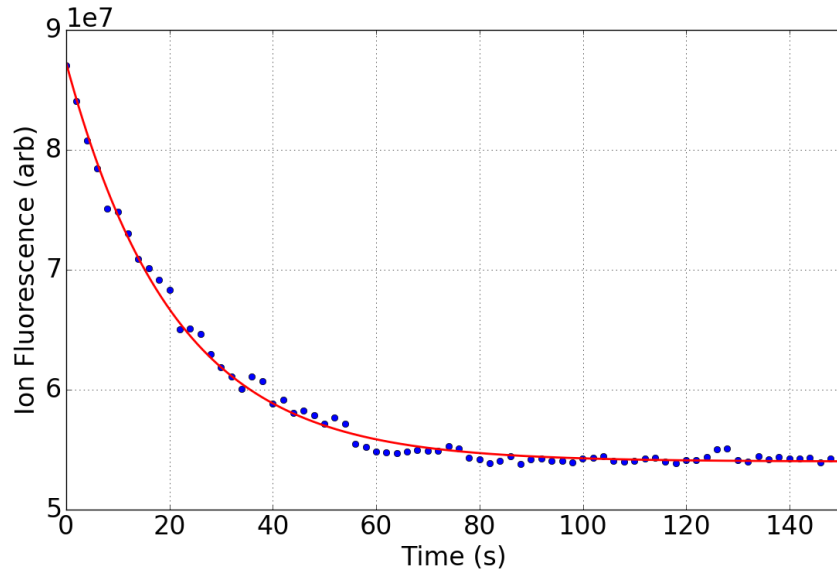


Figure 5.2:

Since the experimental rate constant agrees well with the theoretical rate, we may generalize 5.1 and 5.2.

$$k_{5.2}(T) \approx ((0.54)k_{ADO}(P) + (0.49)k_{ADO}) \times 10^{-9} \text{ cm}^3/\text{s} \quad (5.11)$$

CHAPTER 6



6.1 Isotope-selective chemistry in the $\text{Be}^+(\text{^2S}_{1/2}) + \text{HOD} \rightarrow \text{BeOD}^+/\text{BeOH}^+ + \text{H/D}$ reaction

6.2 Abstract

Low temperature reactions between laser-cooled $\text{Be}^+(\text{^2S}_{1/2})$ ions and partially deuterated water (HOD) molecules have been investigated using an ion trap and interpreted with zero-point corrected quasi-classical trajectory calculations on a highly accurate global potential energy surface for the ground electronic state. Both product channels have been observed for the first time, and the branching to $\text{BeOD}^+ + \text{H}$ is found to be 0.58 ± 0.14 . The experimental observation is reproduced by both quasi-classical trajectory and statistical calculations. Theoretical analyses reveal that the branching to the two product channels is largely due to the availability of open states in each channel.

6.3 Introduction

Together, isotope substitution and the measurement of the resulting product branching ratios provide important details about reaction dynamics and are often used to identify reaction pathways and understand bond-selective chemistry.[?, 10, 57] Important examples include X + HOD (X = H, F, Cl, O) reactions, where the branching ratios are experimentally controlled by selective excitation of the O–H or O–D bond.[41, 5, 30, 58, 45, 46, 15, 60, 42] It is now understood that a highly-accurate potential energy surface (PES) is crucial for performing

theoretical calculations of the product branching ratio, where subtle, difficult to identify, PES features have been found to significantly affect the results.[42]

A sophisticated understanding of radical-molecule reaction dynamics is continuing to develop from extensive experimental and theoretical studies. However, despite their importance in interstellar chemistry, where the isotopic branching ratios strongly influence the products of the interstellar cloud chemical network,far less progress has been made in the study of H_2^{14} ion–molecule reactions at low temperature. This is largely due to the challenges associated with both the experimental and theoretical approaches to these systems.[9, 12, 1, 3, 40, 43, 44] Experimental difficulties include a lack of quantum state preparation and readout techniques, while theoretical difficulties appear when treating dynamics dominated by the long range interaction between ions and molecules. Recently, several groups have employed cold (mK) and fully-controlled laser-cooled trapped ions to address these experimental issues. For instance, isotope selectivity was probed in the reaction of laser-cooled Mg^+ with HD ,and the H_2^{22} formation rate of MgD^+ was found to be 5 times greater than MgH^+ . This observation was ascribed to a dynamic mechanism in the exit channel of the reaction since statistical methods predict only a factor of approximately 2.[11] A similar experimental technique was applied to $\text{Ca}^+ + \text{HD}$ reactions as well,[17] where the CaD^+ channel was found to have 1.5 times higher population than the CaH^+ channel; no detailed theoretical calculations have been performed for this system. With the help of laser-cooled ions, the initial quantum states are experimentally well controlled, but highly accurate PESs are still challenging to calculate with Mg^+ or Ca^+ ions due to the complexity of their electronic structures. The development of a more comprehensive understanding of ion–molecule reactions at low temperature will benefit from studies with less complex species that are amenable to theoretical treatment.

In this publication, we report a combined experimental and theoretical study of the effect of isotope substitution in an ion–polyatomic molecule reaction. A key objective is to understand the role of dynamics in such a reaction. Previous work on $\text{Be}^+ + \text{H}_2\text{O}$ showed that chemical dynamics resulting from a submerged barrier strongly affect the reaction, leading to a reduction of the overall reaction rate from the capture limit. The overestimation

by the capture model was thus taken as a sign that this reaction is not completely statistical, despite the existence of a deep BeH₂O⁺ potential well along the reaction path. In this work, we probe the dynamics by examining the product branching ratio, which is presumably controlled by the exit channel barriers. Such a measurement is much more sensitive to the determination of the overall rates. Interestingly, here we find that the measured deuteration fraction of the ionic products is in good agreement with quasi-classical trajectory (QCT) calculations on the ground state PES. Furthermore, the branching ratio can be explained by a statistical model based on complete energy randomization in the long-lived transition complex.

6.4 Experimental

The apparatus employed here has been described in detail elsewhere. Briefly, laser ablation of metallic Be is used to produce Be⁺ ions, which are trapped in a linear radio frequency Paul trap. Laser cooling[54] is used to cool the translational motion of the ions, resulting in a Coulomb crystal of Be⁺ ions. A time-of-flight mass spectrometer (TOF-MS)[38, 37, 34, ?] is integrated into the Paul trap to analyze reaction products, allowing investigation of the isotope effect by mass spectrometry of the trapped ionic products. The 313 nm laser for cooling Be⁺ ions allows manipulation of the Be⁺ electronic quantum states; by tuning the frequency of this cooling laser, the fraction of ions in the ²S_{1/2} and ²P_{3/2} states can be precisely controlled. Promotion of the Be⁺ to the ²P_{3/2} state opens more product pathways, as well as modifies existing product channels. HOD is made by mixing H₂O and D₂O.[?, ?] The gaseous room-temperature HOD/H₂O/D₂O mixture is then introduced via a leak valve into the trapping region for reaction with the trapped ions, the actual ratio of the mixture is measured from a Stanford Research Systems (SRS) residual gas analyzer (RGA). The RGA's fractionation of water was calibrated by introducing the water vapor into the chamber and integrating all resulting m/z signals. A typical scan reveals water fractionation products at *m/z* = 18, 17, and 16, which coincide with H₂O⁺, OH⁺, and O⁺. The fractionation ratios of water are found by solving the system of equations:

$$P_{\text{H}_2\text{O}} = R_{18} + R_{17} + R_{16} \quad (6.1)$$

$$R_{18} = \alpha P_{\text{H}_2\text{O}} \quad (6.2)$$

$$R_{17} = \beta P_{\text{H}_2\text{O}} \quad (6.3)$$

$$R_{16} = \gamma P_{\text{H}_2\text{O}} \quad (6.4)$$

where R_i is the pressure reading from the RGA and $P_{\text{H}_2\text{O}}$ is the true H_2O pressure. These fragmentation ratios were found to be $\alpha = 0.768 \pm 0.006$, $\beta = 0.184 \pm 0.006$ and $\gamma = 0.068 \pm 0.002$. The direct readings from analog scans with deuterated samples were then adjusted to account for the fractionation for each isotopologue.

$$P_{\text{H}_2\text{O}} = \frac{1}{\alpha} \left(R_{18} - \frac{\beta}{\alpha} R_{20} - \frac{\beta}{2\alpha} R_{19} \right) \quad (6.5)$$

$$P_{\text{HOD}} = \frac{R_{19}}{\alpha} \quad (6.6)$$

$$P_{\text{D}_2\text{O}} = \frac{R_{20}}{\alpha} \quad (6.7)$$

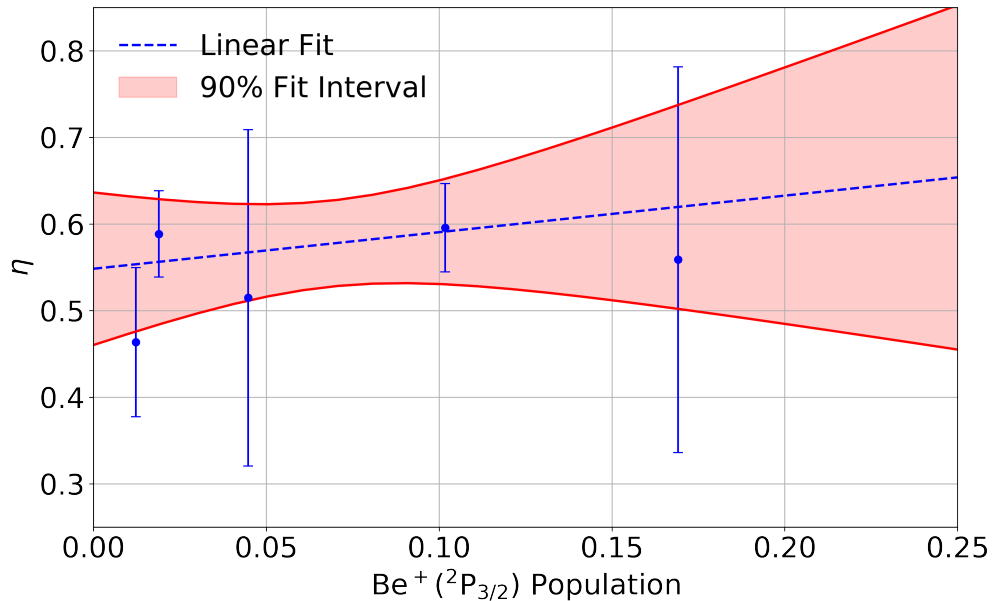


Figure 6.1:

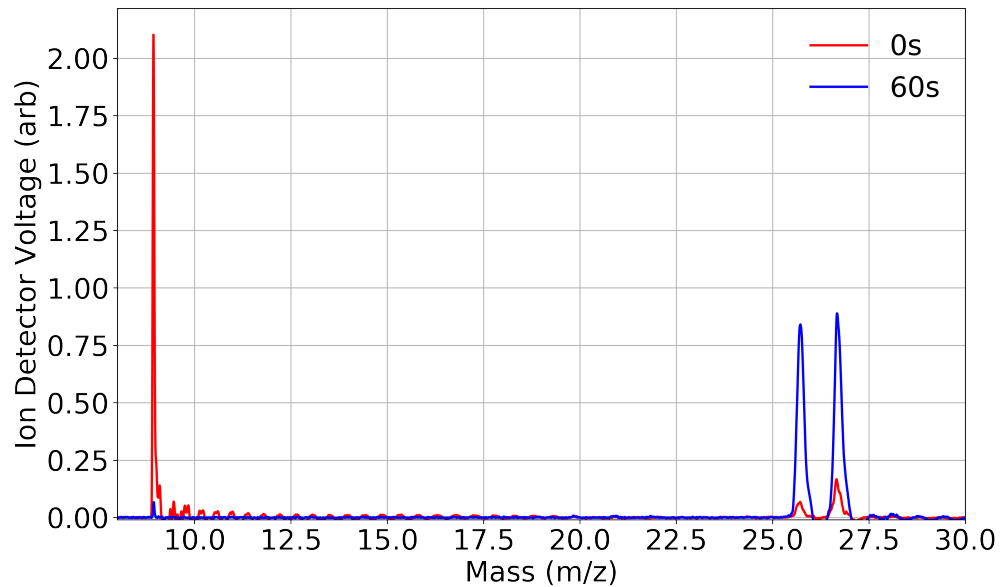


Figure 6.2:

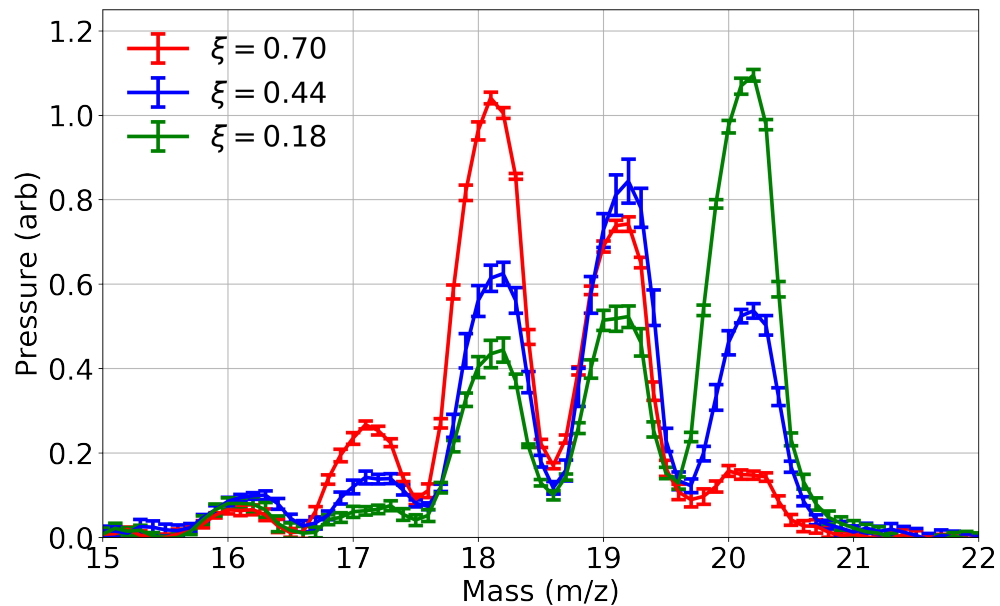


Figure 6.3:

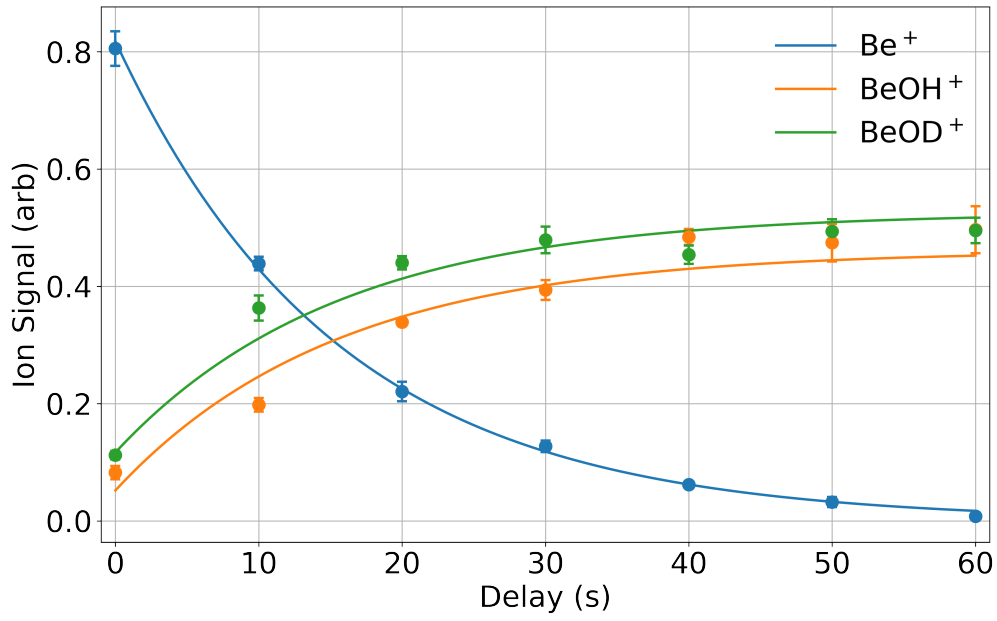


Figure 6.4:

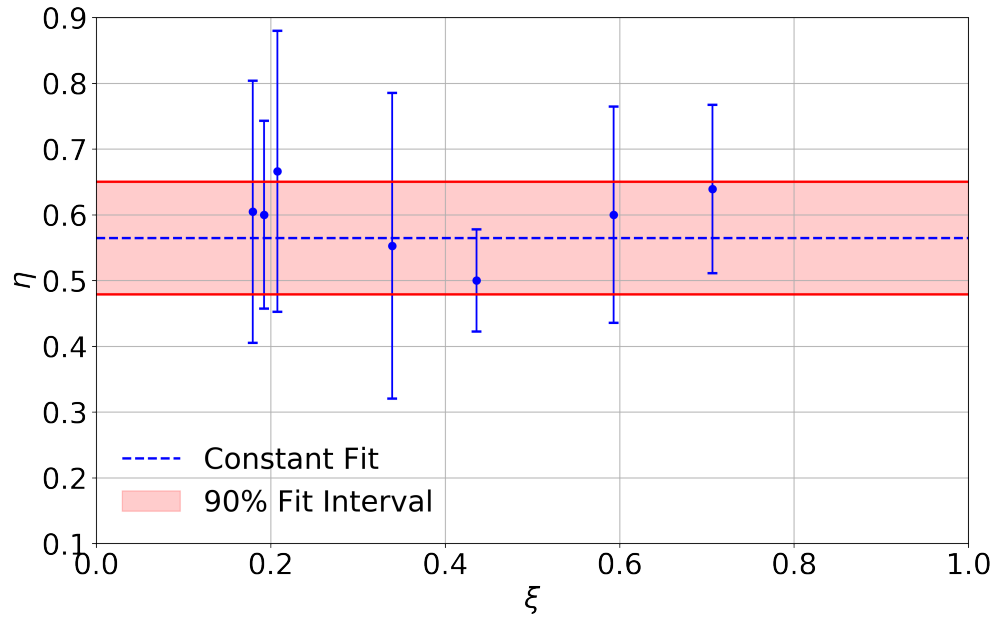
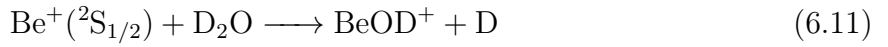
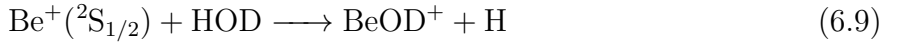
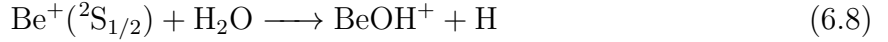


Figure 6.5:

6.5 Results and Discussion

Because the HOD sample also contains both H₂O and D₂O, the product BeOH⁺ ($m/z = 26$) has contributions of the reaction of the cation with H₂O, while BeOD⁺ ($m/z = 27$) has contributions from reactions with D₂O. The reactions of interest are:



Thus, the kinetics of the reagents and products are found from:

$$\dot{\text{Be}}^+(t) = (k_1\rho_1 + k_2\rho_2 + k_3\rho_3)\text{Be}^+(t) \quad (6.12)$$

$$\dot{\text{BeOH}}^+(t) = (k_1\rho_1 + (1 - \eta)k_2\rho_2)\text{Be}^+(t) \quad (6.13)$$

$$\dot{\text{BeOD}}^+(t) = (k_3\rho_3 + \eta k_2\rho_2)\text{Be}^+(t) \quad (6.14)$$

where k_i and ρ_i are the rate coefficient and density for Be^+ reacting H₂O, HOD, and D₂O respectively. The branching ratio $\eta \equiv k_{\text{BeOD}^+}/(k_{\text{BeOD}^+} + k_{\text{BeOH}^+})$ is the fraction of BeOD⁺ produced from reactions (4.2) where k_j is the rate coefficient of species j . Solutions to the rate equations (4.4)–(4.6) are parameterized by the density measurements of the water isotopologues taken from a RGA, and a least-squares fit is taken over data sets of integrated TOF mass spectra with shared fitting parameters k_1 , k_2 , k_3 , and η . In order to extract the pure $\text{Be}^+(^2\text{S}_{1/2})$ and $\text{Be}^+(^2\text{P}_{3/2})$ -state branching ratios, the process shown in Fig. 1(A)–(C) was repeated at different P-state fractions. The results are shown in Fig. 1(D) along with a least-squares linear-fit (blue line). The vertical intercept of this fit gives $\eta_S = 0.56 \pm 0.03$ for the ground $\text{Be}^+(^2\text{S}_{1/2})$ state reaction, while no conclusive dependence on P-state fractions is found within the confidence intervals. To further verify that our measurement is independent

of reagent ratios, we repeated the measurement for different mixtures of HOD, H₂O, and D₂O, as shown in Fig. 3. The branching ratio of BeOD⁺ + H in reaction Be⁺ + HOD (with 2% Be⁺(²P_{3/2}) state population) is consistent over different hydrogen fractions in the gas. The fraction of hydrogen atoms in the chamber (ξ) from all water isotopologues is defined by:

$$\xi = \frac{2\rho_{\text{H}_2\text{O}} + \rho_{\text{HOD}}}{\rho_{\text{H}_2\text{O}} + \rho_{\text{HOD}} + \rho_{\text{D}_2\text{O}}} \quad (6.15)$$

Weighted averaging of the fitted values over different mixtures then gives $\eta = 0.58 \pm 0.14$, $k_2/k_1 = 0.8 \pm 0.9$, $\frac{k_3}{k_1} = 0.8 \pm 0.9$. Despite the large error bars on the relative rate coefficients, due to the significant covariance of the rate coefficients, η is reasonably well determined. To further check our measurement of η , the process was repeated for shared fits with identical rate coefficients ($k_1 = k_2 = k_3$) yielding $\eta = 0.57 \pm 0.07$. The calculated overall rate coefficients of the Be⁺ + D₂O and Be⁺ + HOD reactions are $(2.29 \pm 0.05) \times 10^{-9}$ cm³ molecule⁻¹ s⁻¹ and $(2.29 \pm 0.05) \times 10^{-9}$ cm³ molecule⁻¹ s⁻¹, respectively, which are slightly larger than that $((2.02 \pm 0.04) \times 10^{-9}$ cm³ molecule⁻¹ s⁻¹)25 of the Be⁺ + H₂O reaction. The calculated k_2/k_1 and k_3/k_1 ratios are 1.13 ± 0.04 and 1.13 ± 0.04 , which are consistent with experimental values of 0.8 ± 0.9 and 0.8 ± 0.9 , respectively. The identical k_2/k_1 and k_3/k_1 ratios suggests the negligible isotopic effect in the thermal reaction probabilities of the Be⁺ + D₂O and Be⁺ + HOD reactions. The branching ratio was determined using the QCT method for the Be⁺ + HOD reaction. Specifically, the calculated branching fraction of Be⁺ + HOD (η) is 0.61 ± 0.02 , which is in good agreement with experimental value 0.58 ± 0.14 . The branching ratio of the two products (BeOD⁺ and BeOH⁺) can be understood in terms of the PST model, which assumes complete energy randomization in the deep intermediate (BeHOD⁺) well. In Fig. 4, the branching fraction for the BeOD⁺ + H channel is plotted as a function of the collision energy, which shows very weak temperature dependence. At the specific collisional temperature 100 K, the fraction obtained by integrating the energy dependent branching ratio with a Boltzmann weight is 0.67, which is in reasonable agreement with the QCT results.

To shed more light onto the preference of the $\text{H} + \text{BeOD}^+$ channel in the $\text{Be}^+ + \text{HOD}$ reaction, we provide a further analysis of the two important factors in determining the branching ratio. In PST, the reactivity in a particular product channel is controlled by the availability of open states, which is in turn dictated by the rovibrational states of the corresponding product molecule above the exit barrier formed by the centrifugal potential. Due to the heavier deuterium, it is readily understood that there are more rovibrational states for BeOD^+ than BeOH^+ . However, the availability of open channels is also constrained by the orbital angular momentum (l), which erects a centrifugal barrier in both the reactant and product channels. The l -dependent centrifugal barrier is also isotope dependent, due to the difference in the reduced mass between the two products. The centrifugal barrier rises faster in the $\text{BeOD}^+ + \text{H}$ channel than the $\text{BeOH}^+ + \text{D}$ channel, due to the larger reduced mass of the latter. This is consistent with the fact that the branching fraction (η) of $\text{BeOD}^+ + \text{H}$ channel becomes larger when the centrifugal barrier was not considered (shown in Fig. 4). These two factors have opposing effects on the branching ratio, but the higher density of states in the BeOD^+ molecule dominates, at least at low energies. As a result, the $\text{H} + \text{BeOD}^+$ product channel is strongly favored. The good agreement of the statistical model with both the experimental and QCT results in branching ratio suggests that the reaction is largely statistical. In addition, the DCSs of the $\text{Be}^+ + \text{H}_2\text{O}/\text{HOD}/\text{D}_2\text{O}$ reactions calculated by the QCT method are shown in Fig. 5. It can be seen from the figure that the DCSs of all three reactions are roughly forward–backward symmetric, due to the long-lived intermediates formed in the reactions. The forward–backward symmetry in DCSs suggests the statistical nature of the reaction, which further validates the suitability of the PST model discussed above.

6.6 Conclusion

To summarize, chemical reactions between $\text{Be}^+(^2\text{S}_{1/2})$ and HOD have been investigated using an integrated ion trap and highresolution TOF-MS and ZPE corrected QCT calculations on an accurate global PES. Two product channels have been observed and the branching to

$\text{BeOD}^+ + \text{H}$ is accurately determined to be 0.58 ± 0.14 . The experimental result is in good agreement with ZPE corrected QCT calculation result (0.61 ± 0.02) as well as close to the statistical PST model (0.67), which reveals that the branching to the two product channels is largely due to the availability of different open states in each channel. Since their rate coefficients deviate from the capture limit as reported in our earlier work, it is clear that the $\text{Be}^+(2\text{S}_{1/2}) + \text{H}_2\text{O}/\text{D}_2\text{O}/\text{HOD}$ reactions have a non-negligible non-statistical component. Interestingly, however, the good prediction of the branching ratio by the statistical model discussed above suggests that the formation of the products is largely statistical. This conclusion is further supported by the forward–backward symmetry of the calculated DCSs.

CHAPTER 7

O₂ Titration

7.1 Be⁺ + O₂

Beryllium metal is ablated with an Nd:YAG laser and trapped in a linear Paul trap. Laser cooling is applied with a 313nm laser. Pure O₂ gas is introduced into the chamber via leak valve to react with the ions. Remaining reactants and charged reaction products are ejected into a time-of-flight mass spectrometer (TOF) where the various masses of ions can be determined.

With the introduction of O₂ into the chamber, we consider all the possible reaction products of Be⁺ + O₂



Without excitation into the ²P_{3/2} manifold, reactions 7.1 and 7.2 are endothermic by 2.75 eV and 1.1 eV, respectively. Despite the fact that reaction 7.4 is energetically allowed, it is never seen with laser cooling.

Without 313 nm light, the Be⁺ ions stay in the ²S_{1/2} ground state, but with a ion trap depth > 3 eV, there are portions of the ion cloud with enough energy to still proceed with the production of BeO⁺. Without the laser cooling, we observe the disappearance of BeO⁺

from the trap due to exciting the molecule into a pre-dissociative state.

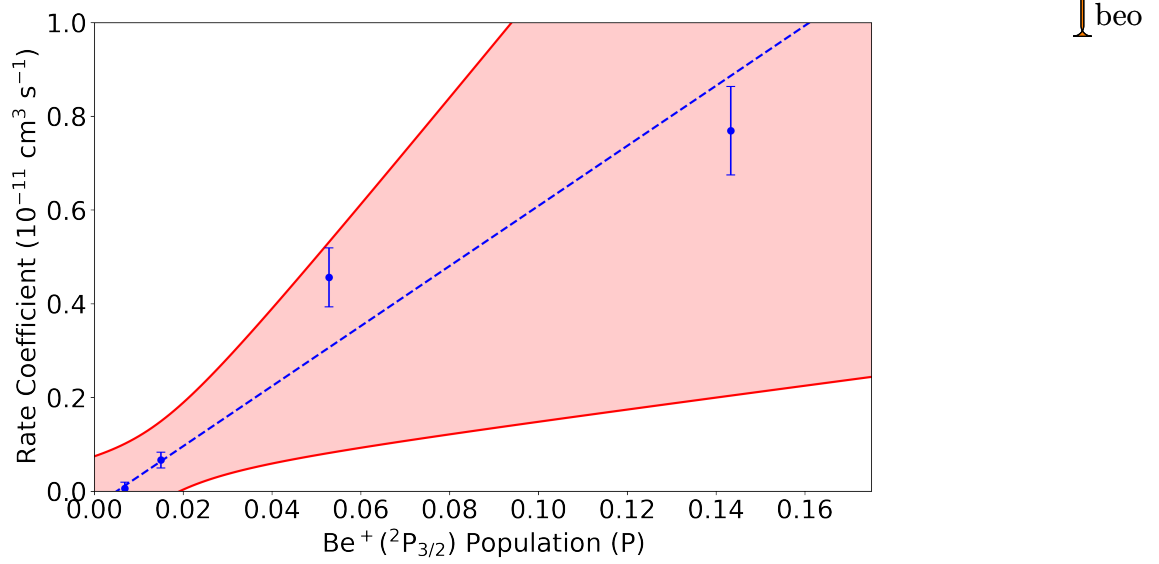


Figure 7.1: A linear dependence on the rate constant for reaction 7.3 as a function of P state excitation. $k = (6 \pm 1) \times 10^{-11}P + (-0.03 \pm 0.16) \times 10^{-11}$

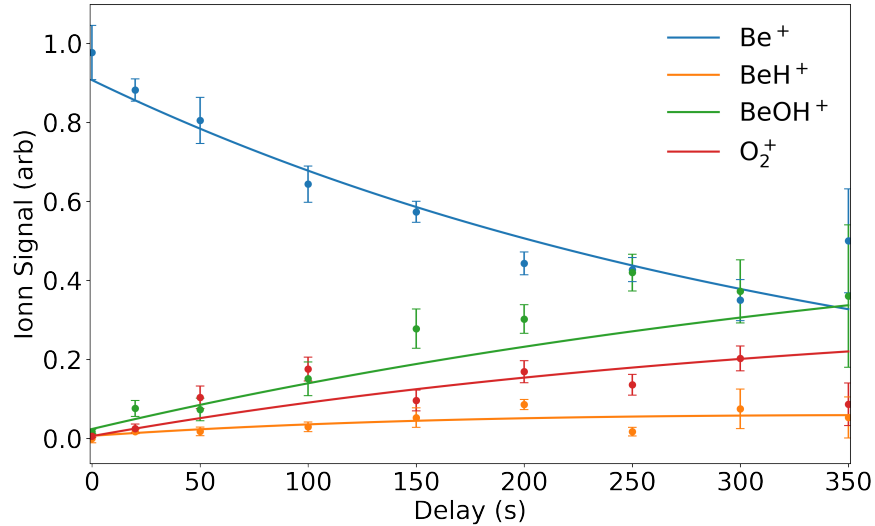


Figure 7.2: Shared fitting of trapped products with 14% p-state excitation.

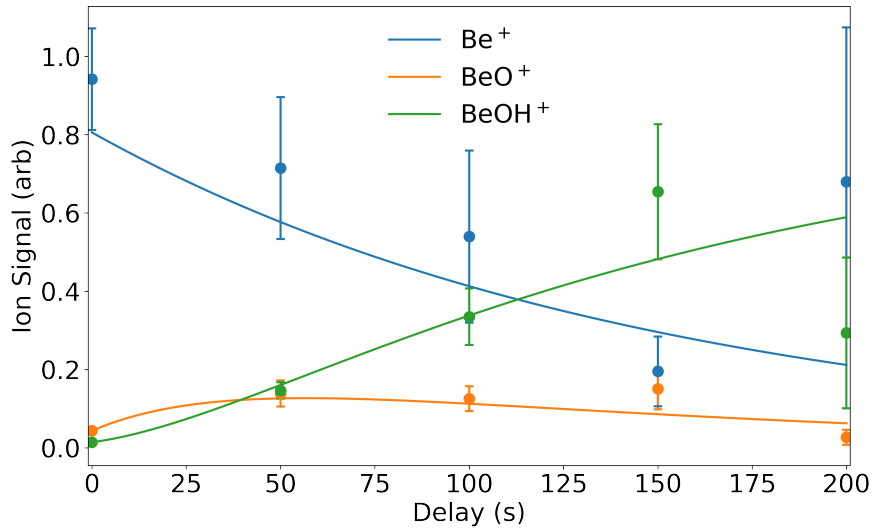


Figure 7.3: Shared fitting of trapped products where Be^+ was exposed to O_2 without the 313 nm light.

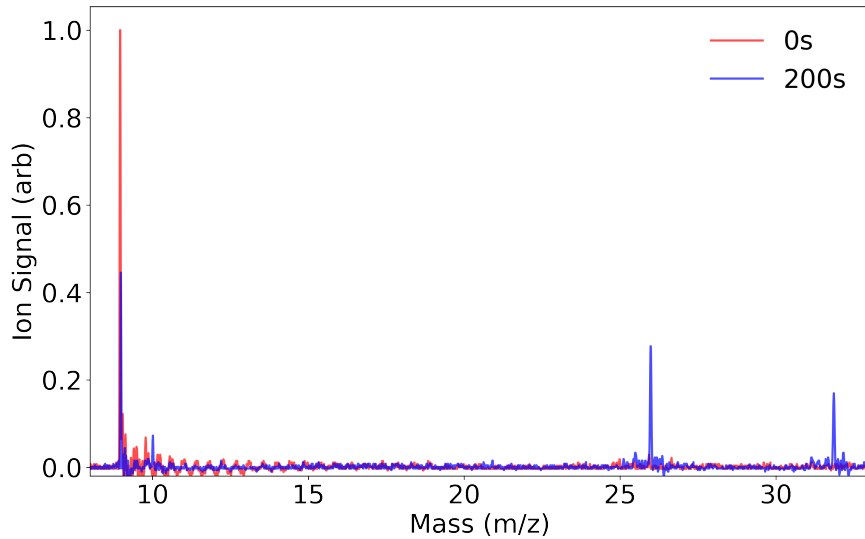


Figure 7.4: TOF traces for data taken with 14% p-state excitation at 0s and 200s showing no products at 0s, distinct peaks for reaction products BeH^+ , BeOH^+ , and O_2^+ , but an absence of BeO^+ .

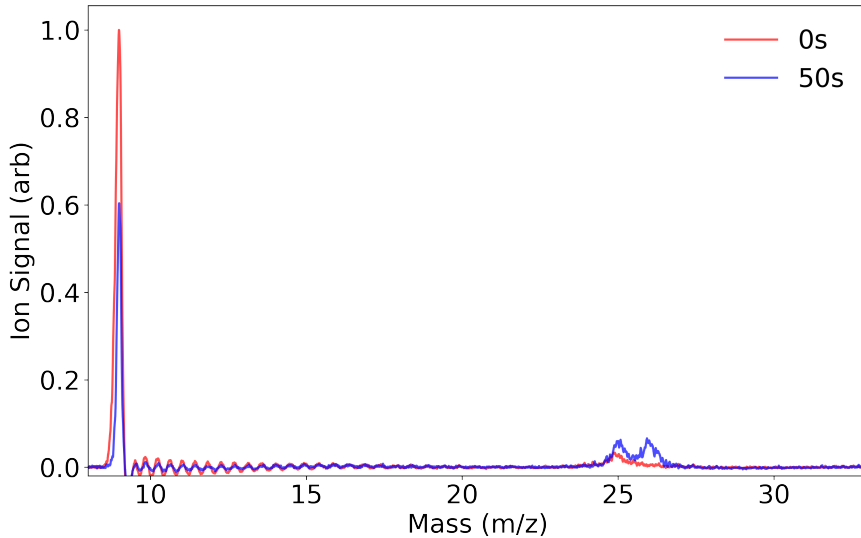


Figure 7.5: TOF traces for data taken with without laser excitation at 0 s and 50 s showing residual BeOH^+ at 0 s, but only an inclusion of BeO^+ at 50 s. More endothermic product channels of BeH^+ and O_2^+ are absent.

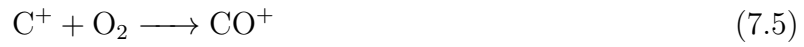
Considering state counting, reactions ?? and ?? have been measured to have branching ratios that vary from 60:40 ($\text{CO}^+:\text{O}^+$) to 30:70 in the other direction. By looking at experimental data as well as the theoretical state counting, we find the ratio to be pretty definitively 60:40.

7.2 $\text{C}^+ + \text{O}_2$

We want to figure out if the $[\text{HCO}]^+$ isomers are still in their internally excited states, as that would change their reactivity with respect to the introduced titration gas X.

By using O_2 , we can see in table 8.1, that we are only eV away from being able to react [] value with the more stable HCO^+ . Given that the main reaction (8.1) is exothermic by 5 eV, if the molecule does not relax within the characteristic time of a collision, we may expect to see some proton exchange occur.

To start, we consider the reactions of C^+ with O_2 :



Where literature tells us that 7.5 7.6 both proceed at approximately $4 \times 10^{-10} \text{ cm}^{-3}/\text{s}$.

We introduce O_2 into the chamber with Be^+ and C^+

CHAPTER 8

Low Temperature C⁺ + H₂O

8.1 Formyl Isomer Production

In the interstellar medium, many reaction occur, in photon dominated regions (PDR's), as these are the regions where both atomic ions and molecules would coexist. At low temperatures, the rate constant of ion-dipole reactions increase, while other rates decrease or do not change, meaning ion-molecule reaction dominate in these cold (10 K - 100 K) PDR's. In particular, we are interested in the cold production of the formyl isomers (HCO⁺ / HOC⁺) via C⁺ and H₂O.



Of which, we verify that the rates of reactions 8.3 and 8.4 are indistinguishable in figure 8.2 such that we may instead write:



Where [HCO]⁺ is used to represent both isomers.

By definition, these formyl isomers of reactions eqs. (8.1) and (8.2) have identical mass and thus, cannot be readily read off by the TOF system. To be able to separate the isomer

products, we need to be able to separate their masses. By introducing a gas into the system with a proton affinity in between the isomer products, we may selectively react only one the less stable HOC^+ isomer. This also yields a distinct m/z peaks originating from separate isomers as seen in reactions 8.6 and 8.8. But by using an external gas, we are doing an indirect measurement, and as such, it may add unintended complications. Certain gasses are more reactive and may react with the excited Be^+ , C^+ , or any other ionized species in the trap. Another possibility is that the COH^+ may isomerize due to interactions with the gas as shown in reaction 8.7.[13]



	Affinity (kcal/mol)
CO*	427
Kr	425
HF	490
N_2	495
Xe	496
NO	531
CO_2	548
CH_4	552
HCl	564
HBr	569
N_2O	571
*CO	594

Table 8.1: Proton affinities of gasses between formyl isomers where (*) indicates H bonding location.

8.2 $^{15}\text{N}_2$ Titration

Previous literature utilized gasses such as NO, CH_4 , N_2O , and Kr to separate the isomers.~~Kr~~ citations and Xe are inert and would not react with any other trapped ion but are too heavy to reliably trap after a reaction. NO is caustic and will ruin the vacuum chamber if introduced, and thus was avoided. Attempts were made with N_2O and well as CH_4 , but both had their own unique complications. N_2O rapidly reacts with Be^+ and made reliable TOF traces unattainable due to the loss of the coolant ion. CH_4 readily reacted with most of the ions in the trap to produce a multitude of mass peaks, greatly complicating the analysis.

Normally N_2 would not be a good choice, due to the fact that N_2H^+ has the same mass as the formyl isomers at $m/z = 29$, but we may instead introduce $^{15}\text{N}_2$ to produce a new peak at $m/z = 31$.

We do not expect and do not see any reaction between the initially loaded ions of Be^+ and C^+ . But according to section 8.1, we should still have a separation of the isomers, thus:



Considering reactions 8.7 and 8.6, if we let $\text{X} = \text{CO}$, we find that both reactions can only yield HCO^+ , allowing us to deterministically produce one of the isomers:



To verify reaction 8.13, trapped Be^+ and C^+ ions are exposed to the water from the CBGB at a density of $4.3 \times 10^6 \text{ cm}^{-3}$ while simultaneously flooded with $\approx 3 \times 10^7 \text{ cm}^{-3}$ of CO from the leak valve connected to the differential pumping region such that $k_{8.13} \gg k_{8.1, 8.2}$.

After 10 s, the gate valve between the differential pumping and experimental ion chamber regions is manually closed, after which, 10^9 cm^{-3} of $^{15}\text{N}_2$ is introduced for 10 s. A TOF trace for this procedure is shown in figure 8.1.

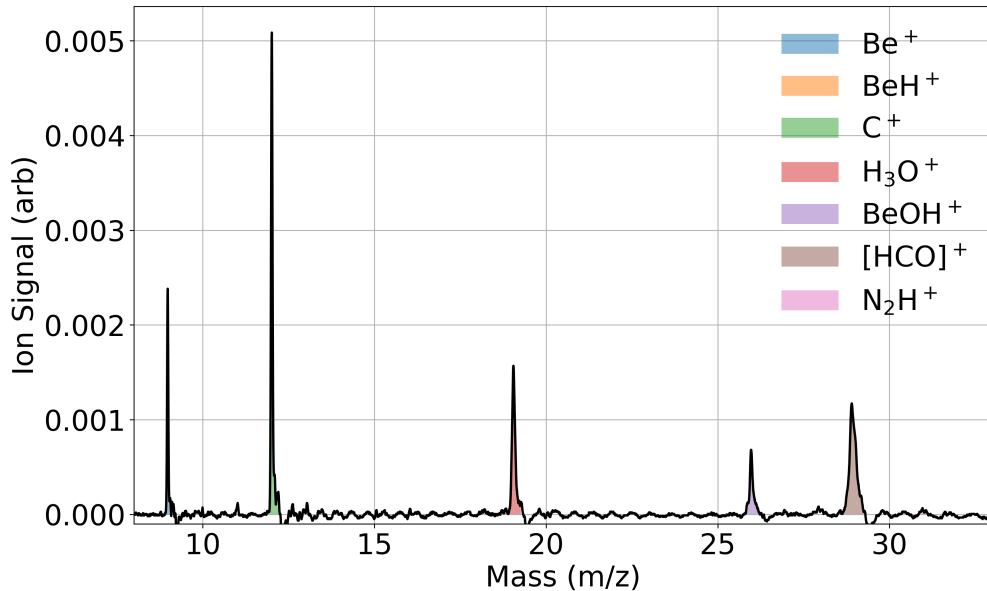


Figure 8.1: TOF trace of reaction products of Be^+ and C^+ after exposure to both water from the CBGB beam, and CO (10 s) before titration with $^{15}\text{N}_2$ (10 s). There is a distinct lack of N_2H^+ , indicating full conversion of $\text{HOC}^+ \longrightarrow \text{HCO}^+$.

Integrated N_2H^+ signal was found to be below the threshold for null signal demonstrating both points that reaction 8.13 proceeds as expected, as well as experimental verification that reaction 8.11 does not occur. Extending this process, we consider the possibility that reactions 8.3 and 8.4 are different by again exposing C^+ to H_2O from the beam to produce $[\text{HCO}]^+$, eliminating the HOC^+ with CO, and finally exposing the everything to H_2O again.

verify
rate
con-
stants

Missing
figure

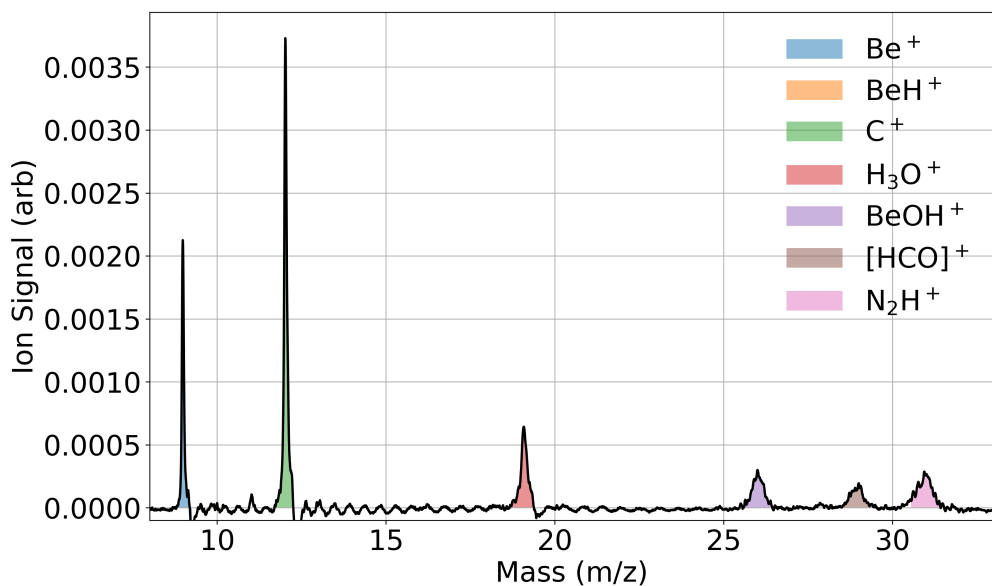
blah

Figure 8.2: text

8.2.1 Branching Ratio Determination

At room temperatures, the branching ratio has been found to be approximately 84:16 ($\text{COH}^+:\text{HCO}^+$)^[14], but unexplored at lower regimes.

To determine the branching ratio, Be^+ and C^+ in the trap are exposed to the CBGB for 10 s, after which, the gate valve connecting the differential pumping region and ion trap chamber is closed. $^{15}\text{N}_2$ is then introduced via leak valve to react with the HOC^+ . Only runs taken at delay times of 10 s were taken, as we only concern ourselves with a ratio of signals.



Repeating this process over various densities of $^{15}\text{N}_2$ allows us to determine the isomer branching ratio. We expect the ratio of N_2H^+ and $[\text{HCO}]^+$ to follow the form:

$$\eta(t) = C(1 - e^{-k_{8.6}\rho t}) \quad (8.14)$$

Where we define $\eta(t) \equiv \frac{^{15}\text{N}_2\text{H}^+(t)}{^{15}\text{N}_2\text{H}^+(t) + [\text{HCO}]^+(t)}$. A fit performed on the data over various densities yields a rate constant of $k_{8.6} = ((6.2 \pm 1.0) \times 10^{-10}) \text{ cm}^3/\text{s}$, and a final branching ratio of $\text{HOC}^+ : \text{HCO}^+ = 0.58 \pm 0.02$.

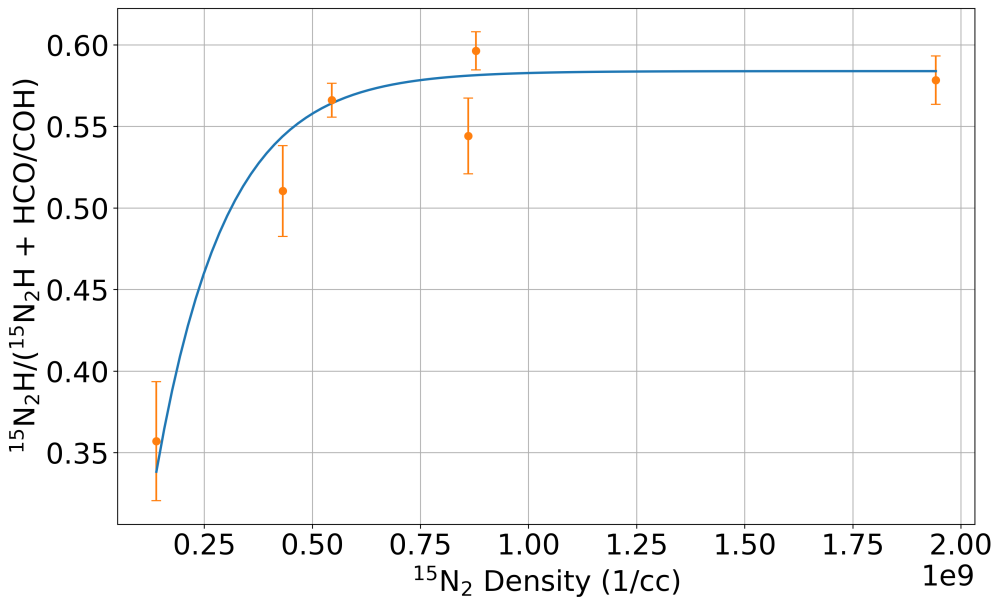


Figure 8.3: $^{15}\text{N}_2$ introduced into the ion chamber after trapped Be^+ and C^+ are exposed to water from the CBGB for set times.

With this fit, we may consider putting bounds on the rate of isomerization by comparing the theoretical rate constant for reaction 8.6 with the fitted value. If reaction 8.7 plays a role, it will proportionally affect the total rate constant. We find the Langevin rate for $\text{HOC}^+ + ^{15}\text{N}_2$ to be $k_L = 8.0 \times 10^{-10} \text{ cm}^3/\text{s}$

To estimate a limit on the isomerization, we consider the above reaction eqs. (8.7) and (8.6), where $\text{X} = ^{15}\text{N}_2$ in the context that we can only determine the abundance of $[\text{HCO}]^+$ and $^{15}\text{N}_2\text{H}^+$. As a function of pressure, we cannot see reaction 8.7, but if it does

contribute, we should see a discrepancy in the total rate constant, which we estimate to be Langevin: $k_L = 8.0 \times 10^{-10}$. This gives us a possible isomerization rate of 22%, which then yield a branching ratio of 70:30

CHAPTER 9

Conclusion and Future Outlook

The experiment has broken new ground in ion-molecule reactions at various reaction temperatures, but there is still much left unexplored. The recent inclusion of two Lioptec dye lasers will allow for more stuff and stuff.

Also stereodynamics with molecules or just atoms

We have only been exciting the Be^+ into the ${}^2\text{P}_{3/2}$ state because it is easier than the ${}^2\text{P}_{1/2}$ manifold, but that would allow us to possibly see fine structure dependent rates and dynamics.

APPENDIX A

Chemical Rate Equations

Rate equations used in the shared fitting programs.

A.1 $\text{Be}^+ + \text{H}_2\text{O} + \text{H}_2$

Differential forms for background reactions:

$$\dot{\text{Be}}(t) = (-k_1\rho_1 + k_2\rho_2)\text{Be}(t) \quad (\text{A.1})$$

$$\dot{\text{BeH}}(t) = k_1\rho_1\text{Be}(t) - k_3\rho_2\text{BeH}(t) \quad (\text{A.2})$$

$$\dot{\text{BeOH}}(t) = k_2\rho_2\text{Be}(t) + k_3\rho_3\text{BeH}(t) \quad (\text{A.3})$$

Where ρ_1 is the density of H_2 and ρ_2 is the density of H_2O . The solutions are as follows:

$$\text{Be}(t) = \text{Be}_0 e^{t(-(k_1\rho_1 + k_2\rho_2))} \quad (\text{A.4})$$

$$\text{BeH}(t) = \frac{1}{\rho_2(k_3 - k_2) - k_1\rho_1} \left[e^{-k_3\rho_2 t} (\text{Be}_0 k_1\rho_1 (e^{-(k_1\rho_1 + k_2\rho_2 - k_3\rho_2)t} - 1) \right. \quad (\text{A.5})$$

$$\left. - \text{BeH}_0 (k_1\rho_1 + \rho_2(k_2 - k_3))) \right] \quad (\text{A.6})$$

$$\text{BeOH}(t) = \frac{e^{-k_3\rho_2 t}}{\rho_2(k_3 - k_2) - k_1\rho_1} \left[\text{Be}_0 (k_1\rho_1 - (k_1\rho_1 + k_2\rho_2 - k_3\rho_2)) e^{k_3\rho_2 t} \right. \quad (\text{A.7})$$

$$\left. + \rho_2(k_2 - k_3) e^{-(k_1\rho_1 + \rho_2(k_2 - k_3))t} \right] \quad (\text{A.8})$$

$$+ ((\text{BeH}_0 + \text{BeOH}_0) e^{k_3\rho_2 t} - \text{BeH}_0) (\rho_2(k_3 - k_2) - k_1\rho_1) \quad (\text{A.9})$$

A.2 Be⁺ + H₂O/HOD/D₂O

Differential forms for:

$$\dot{\text{Be}}(t) = -(k_1\rho_1 + k_2\rho_2 + k_3\rho_3)\text{Be}(t) \quad (\text{A.10})$$

$$\dot{\text{BeOH}}(t) = (k_1\rho_1 + (1 - \eta)k_2\rho_2)\text{Be}(t) \quad (\text{A.11})$$

$$\dot{\text{BeOD}}(t) = (k_3\rho_3 + \eta k_2\rho_2)\text{Be}(t) \quad (\text{A.12})$$

Where ρ_1 is the density of H₂O, ρ_2 is the density of HOD, and ρ_3 is the density of D₂O.

The solutions are as follows:

$$\text{Be}(t) = \text{Be}_0 e^{-(k_1\rho_1 + k_2\rho_2 + k_3\rho_3)t} \quad (\text{A.13})$$

$$\begin{aligned} \text{BeOD}(t) = & \frac{1}{k_1\rho_1 + k_2\rho_2 + k_3\rho_3} [\text{Be}_0(\eta k_2\rho_2 + k_3\rho_3)(1 - e^{-(k_1\rho_1 + k_2\rho_2 + k_3\rho_3)t}) \\ & + \text{BeOD}_0(k_1\rho_1 + k_2\rho_2 + k_3\rho_3)] \end{aligned} \quad (\text{A.14})$$

$$\begin{aligned} \text{BeOH}(t) = & \frac{1}{k_1\rho_1 + k_2\rho_2 + k_3\rho_3} [\text{Be}_0(k_1\rho_1 - (\eta - 1)k_2\rho_2)(1 - e^{-(k_1\rho_1 + k_2\rho_2 + k_3\rho_3)t}) \\ & + \text{BeOH}_0(k_1\rho_1 + k_2\rho_2 + k_3\rho_3)] \end{aligned} \quad (\text{A.16})$$

$$+ \text{BeOH}_0(k_1\rho_1 + k_2\rho_2 + k_3\rho_3)] \quad (\text{A.17})$$

A.3 C⁺ + H₂O

Differential forms for 8.1, 8.2, and 8.5.

$$\dot{\text{C}}(t) = -k_1\rho\text{C}(t) \quad (\text{A.18})$$

$$[\dot{\text{HCO}}](t) = \rho(k_1\text{C}(t) + k_2[\text{HCO}](t)) \quad (\text{A.19})$$

$$\dot{\text{H}_3\text{O}}(t) = k_2\rho[\text{HCO}](t) \quad (\text{A.20})$$

Where ρ is the density of H₂O. The solutions are as follows:

$$C(t) = C_0 e^{-k_1 \rho t} \quad (\text{A.21})$$

$$[\text{HCO}](t) = \frac{e^{-(k_1+k_2)\rho t}}{k_1 - k_2} (e^{k_1 \rho t} ((C_0 + [\text{HCO}]_0)k_1 - [\text{HCO}]_0 k_2) - C_0 e^{-(k_1+k_2)\rho t}) \quad (\text{A.22})$$

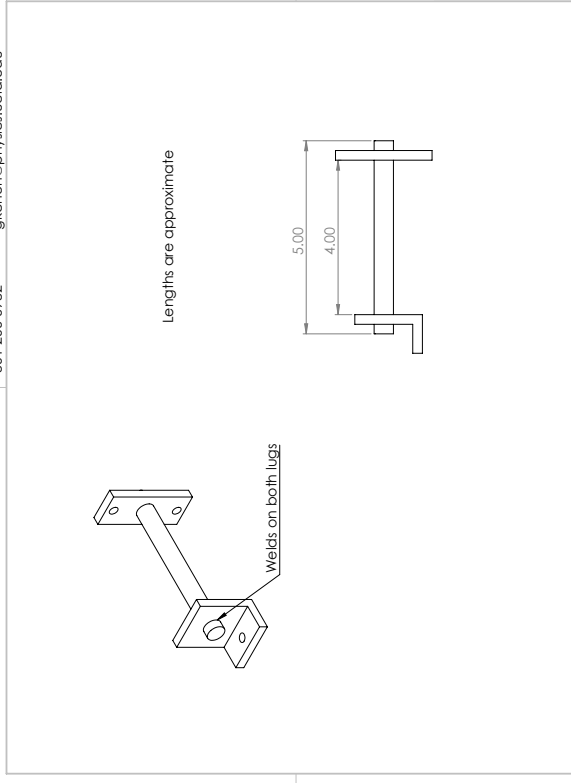
$$\text{H}_3\text{O}(t) = \text{H}_3\text{O}_0 + [\text{HCO}]_0(1 - e^{-k_2 \rho t}) + \frac{C_0 (k_1 (1 - e^{-k_2 \rho t}) + k_2 (e^{-k_1 \rho t} - 1))}{k_1 - k_2} \quad (\text{A.23})$$

APPENDIX B

CBGB Drawings

4K_thermal_link

Campbell Lab Attn: Gary Chen
301-206-6782



Tolerance: $X_{XXX} = +/-0.05$
 $X_{XXX} = +/-0.005$

Material: Cu 10100
Quantity: 2

REFERENCES

- [1] N. G. Adams and D. Smith. The selected ion flow tube (SIFT); A technique for studying ion-neutral reactions. *International Journal of Mass Spectrometry and Ion Physics*, 21(3-4):349–359, 1976.
- [2] Marcelino Agúndez and Valentine Wakelam. Chemistry of Dark Clouds: Databases, Networks, and Models. *Chemical Reviews*, 113(12):8710–8737, 2013.
- [3] PB Armentrout. Reactions and Thermochemistry of Small Transition Metal Cluster Ions. *Annual Review of Physical Chemistry*, 52(1):423–461, 2002.
- [4] J J Bollinger, J S Wells, D J Wineland, and Wayne M Itano. Hyperfine structure of the $2p^2P_{1/2}$ state in ${}^9\text{Be}^+$. *Physical Review A*, 31(4):2711–2714, 1985.
- [5] Michael J. Bronikowski, William R. Simpson, Bertrand Girard, and Richard N. Zare. Bond-specific chemistry: OD:OH product ratios for the reactions H+HOD(100) and H+HOD(001). *Journal of Chemical Physics*, 95(11):8647–8648, 1991.
- [6] Eduardo Carrascosa, Jennifer Meyer, and Roland Wester. Imaging the dynamics of ion-molecule reactions. *Chemical Society Reviews*, 46(24):7498–7516, 2017.
- [7] Kuang Chen, Scott T. Sullivan, and Eric R. Hudson. Neutral gas sympathetic cooling of an ion in a Paul trap. *Physical Review Letters*, 112(14):1–5, 2014.
- [8] Kuang Chen, Scott T. Sullivan, Wade G. Rellergert, and Eric R. Hudson. Measurement of the coulomb logarithm in a radio-frequency Paul trap. *Physical Review Letters*, 110(17):1–5, 2013.
- [9] D. C Clary. Fast Chemical Reactions: Theory Challenges Experiment. *Annual Review of Physical Chemistry*, 41(1):61–90, 1990.
- [10] F. Fleming Crim. Bond-selected chemistry: Vibrational state control of photodissociation and bimolecular reaction. *Journal of Physical Chemistry*, 100(31):12725–12734, 1996.
- [11] N. F. Dalleska, Kevin C. Crellin, and P. B. Armentrout. Reactions of alkaline earth ions with hydrogen, deuterium, and hydrogen deuteride. *The Journal of Physical Chemistry*, 97(13):3123–3128, 2005.
- [12] C. E. Dateo and D. C. Clary. Rate constant calculations on the $\text{C}^+ + \text{HCl}$ reaction. *The Journal of Chemical Physics*, 1989.
- [13] Colin G. Freeman, John S. Knight, Jonathan G. Love, and Murray J. McEwan. The reactivity of HOC^+ and the proton affinity of CO at O. *International Journal of Mass Spectrometry and Ion Processes*, 80(C):255–271, 1987.

- [14] Colin G. Freeman and Murray J. McEwan. A selected-ion flow tube study of the $\text{C}^+ + \text{H}_2\text{O}$ reaction. *International Journal of Mass Spectrometry and Ion Processes*, 75(1):127–131, 1987.
- [15] Bina Fu and Dong H. Zhang. A full-dimensional quantum dynamics study of the mode specificity in the $\text{H} + \text{HOD}$ abstraction reaction. *Journal of Chemical Physics*, 142(6), 2015.
- [16] George Gioumousis and D. P. Stevenson. Reactions of gaseous molecule ions with gaseous molecules. V. theory. *The Journal of Chemical Physics*, 29(2):294–299, 1958.
- [17] Anders K. Hansen, Magnus A. Sørensen, Peter F. Staanum, and Michael Drewsen. Single-ion recycling reactions. *Angewandte Chemie - International Edition*, 51(32):7960–7962, 2012.
- [18] William L. Hase, Jochen Mikosch, Roland Wester, Jiaxu Zhang, Rico Otto, and Jing Xie. Identification of Atomic-Level Mechanisms for Gas-Phase $\text{X}^- + \text{CH}_3 \text{Y S}_N\text{2}$ Reactions by Combined Experiments and Simulations. *Accounts of Chemical Research*, 47(10):2960–2969, 2014.
- [19] J L Highberger, C Savage, J H Bieging, and L M Ziurys. HEAVY-METAL CHEMISTRY IN PROTO-PLANETARY NEBULAE: DETECTION OF MgNC, NaCN, AND AlF TOWARD CRL 2688. *the Astrophysical Journal*, 562:790–798, 2001.
- [20] Eric R. Hudson. Sympathetic cooling of molecular ions with ultracold atoms. *EPJ Techniques and Instrumentation*, 3(1):8, 2016.
- [21] W. T. Huntress and R. F. Pinizzotto. Product distributions and rate constants for ion-molecule reactions in water, hydrogen sulfide, ammonia, and methane. *The Journal of Chemical Physics*, 59(9):4742–4756, 2004.
- [22] Nicholas R Hutzler, Hsin-I Lu, and John M Doyle. The buffer gas beam: an intense, cold, and slow source for atoms and molecules. *Chemical reviews*, 112(9):4803–27, sep 2012.
- [23] NR Nicholas R Hutzler, MF Maxwell F Parsons, Yulia V Gurevich, Paul W Hess, Elizabeth Petrik, Ben Spaun, Amar C Vutha, David Demille, Gerald Gabrielse, and John M Doyle. A cryogenic beam of refractory, chemically reactive molecules with expansion cooling. . . . *Chemistry Chemical . . .*, 13(42):1–16, 2011.
- [24] Vladimir A Krasnopolsky. Chemical composition of Titan’s atmosphere and ionosphere: Observations and the photochemical model. *Icarus*, 236:83–91, 2014.
- [25] D. J. Larson, J. C. Bergquist, J. J. Bollinger, Wayne M. Itano, and D. J. Wineland. Sympathetic cooling of trapped ions: A laser-cooled two-species nonneutral ion plasma. *Physical Review Letters*, 57(1):70–73, 1986.

- [26] Adan Li, Jianzheng Song, Yang Sun, and Tifeng Jiao. The application of resonance-enhanced multiphoton ionization technique in gas chromatography mass spectrometry. *Journal of Spectroscopy*, 2014, 2014.
- [27] Jun Li, Bin Jiang, and Hua Guo. Spin-orbit corrected full-dimensional potential energy surfaces for the two lowest-lying electronic states of FH_2O and dynamics for the $\text{F} + \text{H}_2\text{O} \rightarrow \text{HF} + \text{OH}$ reaction. *Journal of Chemical Physics*, 138(7), 2013.
- [28] Jun Li, Bin Jiang, Hongwei Song, Jianyi Ma, Bin Zhao, Richard Dawes, and Hua Guo. From ab initio potential energy surfaces to state-resolved reactivities: $\text{X} + \text{H}_2\text{O} \leftrightarrow \text{HX} + \text{OH}$ [$\text{X} = \text{F}, \text{Cl}$, and $\text{O}({}^3\text{P})$] reactions. *Journal of Physical Chemistry A*, 119(20):4667–4687, 2015.
- [29] U. Lourderaj, M. Weidemuller, W. L. Hase, J. Mikosch, R. Otto, R. Wester, C. Eichhorn, J. X. Zhang, and S. Trippel. Imaging Nucleophilic Substitution Dynamics. *Science*, 319(5860):183–186, 2008.
- [30] Ricardo B. Metz, John D. Thoemke, Joann M. Pfeiffer, and F. Fleming Crim. Selectively breaking either bond in the bimolecular reaction of HOD with hydrogen atoms. *Journal of Chemical Physics*, 99(3):1744–1751, 1993.
- [31] Edvardas Narevicius, Adam Libson, Christian G. Parthey, Isaac Chavez, Julia Narevicius, Uzi Even, and Mark G. Raizen. Stopping supersonic oxygen with a series of pulsed electromagnetic coils: A molecular coilgun. *Physical Review A - Atomic, Molecular, and Optical Physics*, 77(5):1–4, 2008.
- [32] M. Oppenheimer and A. Dalgarno. The Fractional Ionization in Dense Interstellar Clouds. *The Astrophysical Journal*, 192(12):29, 2002.
- [33] Hans Pauly. *Atom, Molecule, and Cluster Beams I: Basic Theory, Production and Detection of Thermal Energy Beams*, volume 28. Springer, 2000.
- [34] Prateek Puri, Michael Mills, Christian Schneider, Ionel Simbotin, John A. Montgomery, Robin Côté, Arthur G. Suits, and Eric R. Hudson. Synthesis of mixed hypermetallic oxide BaOCa^+ from laser-cooled reagents in an atom-ion hybrid trap. *Science*, 357(6358):1370–1375, 2017.
- [35] Amelia W. Ray, Jianyi Ma, Rico Otto, Jun Li, Hua Guo, and Robert E. Continetti. Effects of vibrational excitation on the $\text{F} + \text{H}_2\text{O} \rightarrow \text{HF} + \text{OH}$ reaction: Dissociative photodetachment of overtone-excited $[\text{F}-\text{H}-\text{OH}]^-$. *Chemical Science*, 8(11):7821–7833, 2017.
- [36] B. Roth, P. Blythe, H. Wenz, H. Daerr, and S. Schiller. Ion-neutral chemical reactions between ultracold localized ions and neutral molecules with single-particle resolution. *Physical Review A - Atomic, Molecular, and Optical Physics*, 73(4):1–9, 2006.

- [37] Christian Schneider, Steven J. Schowalter, Kuang Chen, Scott T. Sullivan, and Eric R. Hudson. Laser-Cooling-Assisted Mass Spectrometry. *Physical Review Applied*, 2(3):1–7, 2014.
- [38] Steven J. Schowalter, Kuang Chen, Wade G. Rellergert, Scott T. Sullivan, and Eric R. Hudson. An integrated ion trap and time-of-flight mass spectrometer for chemical and photo- reaction dynamics studies. *Review of Scientific Instruments*, 83(4), 2012.
- [39] Steven J. Schowalter, Alexander J. Dunning, Kuang Chen, Prateek Puri, Christian Schneider, and Eric R. Hudson. Blue-sky bifurcation of ion energies and the limits of neutral-gas sympathetic cooling of trapped ions. *Nature Communications*, 7:1–8, 2016.
- [40] Ian R Sims. Gas-Phase Reactions and Energy Transfer at Very Low Temperatures. *Annual Review of Physical Chemistry*, 46(1):109–137, 2002.
- [41] Amitabha Sinha, Mark C. Hsiao, and F. Fleming Crim. Bond-selected bimolecular chemistry: $\text{H} + \text{HOD}(4\nu_{OH}) \rightarrow \text{OD} + \text{H}_2$. *The Journal of Chemical Physics*, 92(10):6333–6335, 1990.
- [42] Dimitris Skouteris, David E. Manolopoulos, Wensheng Bian, Hans Joachim Werner, Lih Huey Lai, and Kopin Liu. Van der Waals interactions in the Cl + HD reaction. *Science*, 286(5445):1713–1716, 1999.
- [43] I. W M Smith and Bertrand R. Rowe. Reaction kinetics at very low temperatures: Laboratory studies and interstellar chemistry. *Accounts of Chemical Research*, 33(5):261–268, 2000.
- [44] Theodore P. Snow and Veronica M. Bierbaum. Ion Chemistry in the Interstellar Medium. *Annual Review of Analytical Chemistry*, 1(1):229–259, 2008.
- [45] Hongwei Song and Hua Guo. Vibrational and Rotational Mode Specificity in the Cl + H₂O → HCl + OH Reaction: A Quantum Dynamical Study. *Journal of Physical Chemistry A*, 119(24):6188–6194, 2015.
- [46] Hongwei Song, Soo Ying Lee, Yunpeng Lu, and Hua Guo. Full-Dimensional Quantum Dynamical Studies of the Cl + HOD → HCl/DCl + OD/OH Reaction: Bond Selectivity and Isotopic Branching Ratio. *Journal of Physical Chemistry A*, 119(50):12224–12230, 2015.
- [47] Timothy Su and Michael T. Bowers. Ion-polar molecule collisions: the effect of ion size on ion-polar molecule rate constants; the parameterization of the average-dipole-orientation theory. *International Journal of Mass Spectrometry and Ion Physics*, 12(4):347–356, 1973.
- [48] Timothy Su and Michael T. Bowers. Theory of ion-polar molecule collisions. Comparison with experimental charge transfer reactions of rare gas ions to geometric isomers of difluorobenzene and dichloroethylene. *The Journal of Chemical Physics*, 58(7):3027–3037, 1973.

- [49] Timothy Su and Michael T. Bowers. Ion-polar molecular collisions: the average quadrupole orientation theory. *International Journal of Mass Spectrometry and Ion Physics*, 17(3):309–319, 1975.
- [50] Michał Tomza, Krzysztof Jachymski, Rene Gerritsma, Antonio Negretti, Tommaso Calarco, Zbigniew Idziaszek, and Paul S. Julienne. Cold hybrid ion-atom systems. pages 1–61, 2017.
- [51] J. Troe. Statistical adiabatic channel model of ion-neutral dipole capture rate constants. *Chemical Physics Letters*, 122(5):425–430, 1985.
- [52] Ewine F. van Dishoeck, Eric Herbst, and David A. Neufeld. Interstellar Water Chemistry: From Laboratory to Observations. *Chemical Reviews*, 113(12):9043–9085, 2013.
- [53] Stefan Willitsch. Coulomb-crystallised molecular ions in traps: Methods, applications, prospects. *International Reviews in Physical Chemistry*, 31(2):175–199, 2012.
- [54] D. J. Wineland and Wayne M. Itano. Laser cooling of atoms. *Physical Review A*, 20(4):1521–1540, 1979.
- [55] Paul Wolfgang. Electromagnetic Traps For charged And Neutral Particles, 1990.
- [56] Chunlei Xiao, Xin Xu, Shu Liu, Tao Wang, Wenrui Dong, Tiangang Yang, Zhigang Sun, Dongxu Dai, Xin Xu, Dong H Zhang, and Xueming Yang. Experimental and theoretical differential cross sections for a four-atom reaction: $\text{HD} + \text{OH} \rightarrow \text{H}_2\text{O} + \text{D}$. *Science*, 333(6041):440–442, 2011.
- [57] Richard N. Zare. Laser Control of Chemical Reactions. *Science*, 279(5358):1875–1879, 1998.
- [58] Dong H Zhang and John C Light. Full-dimensional quantum study. 93(5):691–697, 1997.
- [59] Dongdong Zhang and Stefan Willitsch. Cold ion chemistry. 2017.
- [60] Rui Zheng, Yongfa Zhu, and Hongwei Song. Mode specific dynamics in bond selective reaction $\text{O}'(^3\text{P}) + \text{HOD} \rightarrow \text{O}'\text{H} + \text{OD}/\text{O}'\text{D} + \text{OH}$. *Journal of Chemical Physics*, 149(5), 2018.